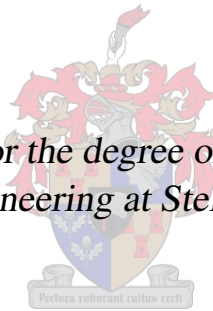


Formulation of a weakly compressible two-fluid
flow solver and the development of a compressive
surface capturing scheme using the volume-of-fluid
approach

by

Johan Adam Heyns

*Dissertation approved for the degree of Doctor of Philosophy in
the Faculty of Engineering at Stellenbosch University*



Supervisors:

Prof T.M. Harms Prof A.G. Malan
University of Stellenbosch University of Cape Town

December 2012

Declaration

By submitting this dissertation electronically, I declare that the entirety of the work contained therein is my own, original work, that I am the sole author thereof (save to the extent explicitly otherwise stated), that reproduction and publication thereof by Stellenbosch University will not infringe any third party rights and that I have not previously in its entirety or in part submitted it for obtaining any qualification.

Signature:

J.A. Heyns

Date:

Copyright © 2012 Stellenbosch University
All rights reserved.

Abstract

Formulation of a weakly compressible two-fluid flow solver and the development of a compressive surface capturing scheme using the volume-of-fluid approach

J.A. Heyns

Dissertation: PhD (Mech Eng)

December 2012

This study presents the development and extension of free-surface modelling techniques for the purpose of modelling two-fluid systems accurately and efficiently. The volume-of-fluid (VOF) method is extended in two ways: Firstly, it is extended to account for variations in the gas density through a weakly compressible formulation. Secondly, a compressive free-surface interface capturing formulation that preserves the integrity of the interface shape is detailed. These formulations were implemented and evaluated using the *Elemental* software.

Under certain flow conditions liquid-gas systems may be subjected to large variations in pressure, making it necessary to account for changes in gas density. Modelling this effectively has received relatively little attention in the context of free-surface modelling and remains a challenge to date. To account for the variations in gas density a weakly compressible free-surface modelling formulation is developed for low Mach number flows. The latter is formally substantiated via a non-dimensional analysis. It is proposed that the new formulation advances on existing free-surface modelling formulations by effecting an accurate representation of the dominant physics in an efficient and effective manner.

The proposed weakly compressible formulation is discretised using a vertex-centred edge-base finite volume approach, which provides a computationally efficient method of data structuring and memory usage. Furthermore, this implementation is applicable to unstructured spatial discretisation and parallel computing. In this light, the discretisation is formulated to ensure a stable, oscillatory free solution. Furthermore, the governing equations are solved in a fully coupled manner using a combination of dual time-stepping and a Generalised Minimum Residual solver with Lower-Upper Symmetric Gauss-Seidel preconditioning, ensuring a fast and efficient solution.

ABSTRACT

The newly developed VOF interface capturing formulation is proposed to advance on the accuracy and efficiency with which the evolution of the free-surface interface is modelled. This is achieved through a novel combination of a blended higher-resolution scheme, used to interpolate the volume fraction face value, and the addition of an artificial compressive term to the VOF equation. Furthermore, the computational efficiency of the higher-resolution scheme is improved through the reformulation of the normalised variable approach and the implementation of a new higher-resolution blending function.

For the purpose of evaluating the newly developed methods, several test cases are considered. It is demonstrated that the new surface capturing formulation offers a significant improvement over existing schemes, particularly at large CFL numbers. It is shown that the proposed method achieves a sharper, better defined interface for a wide range of flow conditions. With the validation of the weakly compressible formulation, it is found that the numerical results correlate well with analytical solutions. Furthermore, the importance of accounting for gas compressibility is demonstrated via an application study. The weakly compressible formulation is also found to result in negligible additional computational cost while resulting in improved convergence rates.

Uittreksel

Formulering van 'n swak samedrukbare twee-vloeistof berekeningsmodel sowel as die ontwikkeling van 'n numeriese skema vir die hoë-resolusie modellering van 'n vloeistof-oppervlak deur gebruik te maak van die volume-van-vloeistof benadering

J.A. Heyns

Proefskrif: PhD (Meg Ing)

Desember 2012

Hierdie studie behels die ontwikkeling van numeriese tegnieke met die doel om twee-vloeistof vloeï akkuraat en numeries effektief te modelleer. Die volume-van-vloeistof metode word op twee maniere uitgebrei: Eerstens word variasie van die gasdigtheid in ag geneem deur gebruik te maak van 'n swak samedrukbare model. Tweedens saam is 'n hoë-resolusie metode geformuleer vir die voorstelling van die vloeistof-oppervlak. Hierdie uitbreidings is met die behulp van die *Elemental* programmatuur geïmplementeer en met behulp van die programmatuur geëvalueer.

Onder sekere toestande ervaar vloeistof-gas mengsels groot veranderinge in druk. Dit vereis dat die variasie in gasdigtheid in berekening gebring moet word. Die modellering hiervan het egter tot dusver relatief min aandag ontvang. Om hierdie rede word 'n swak samedrukbare model vir lae Mach-getalle voorgestel om die variasie in gasdigtheid in te reken. Die formulering volg uit 'n nie-dimensionele analise. Daar word geargumenteer dat die nuwe formulering die fisika meer akkuraat verteenwoordig.

'n Gesentraliseerde hoekpunt, rant gebaseerde eindige volume metode word gevolg om die differensiaalvergelykings numeries te diskretiseer. Dit bied 'n doeltreffende manier vir datastrukturering en geheuebenutting. Hierdie benadering is verder geskik vir toepassing op ongestruktureerde roosters en parallelverwerking. Die diskretisering is geformuleer om 'n stabiele oplossing sonder numeriese ossillasies te verseker. Die vloeivergelykings word op 'n gekoppelde wyse opgelos deur gebruik te maak van 'n kombinasie van 'n pseudo tyd-stap metode en 'n Veralgemene Minimum Residu berekeningsmetode met Onder-Bo Simmetriese Gauss-Seidel voorafbewerking.

UITTREKSEL

Die nuut ontwikkelde skema vir die modellering van die vloeistof-oppervlak is veronderstel om 'n meer akkurate voorstelling te bied en meer doeltreffend te wees vir numeriese berekeninge. Dit word bereik deur die nuwe kombinasie van 'n hoë-resolusie skema, wat gebruik word om die volumefraksie te interpoleer, met die samevoeging van 'n kunsmatige term in die volume-van-vloeistof vergelyking om die resolusie te verfyn. Verder is die doeltreffendheid van die skema verbeter deur die genormaliseerde veranderlikes benadering te herformuleer en deur die ontwikkeling van 'n nuwe hoë-resolusie vermengingsfunksie.

Verskeie toetsgevalle is uitgevoer met die doel om die nuwe modelle te evalueer. Daar word aangetoon dat die nuwe skema vir die modellering van die vloeistof-oppervlak 'n meetbare verbetering bied, veral by hoër Courant-Friedrichs-Lewy getalle. Die nuwe formulering bied dus hoër akkuraatheid vir 'n wye verskeidenheid van toestande. Vir die swak samedrukbare formulering is daar 'n goeie korrelasie tussen die numeriese resultate en die analitiese oplossing. In 'n toegepassingsgeval word die noodsaaklikheid om die samedrukbaarheid van die gas in ag te neem gedemonstreer. Die addisionele berekening-kostes van die nuwe formulering is weglaatbaar en in sommige gevalle verhoog die tempo waarteen die oplossing konvergeer.

Acknowledgements

I would like to express my deepest gratitude to my supervisors, Prof. A.G. Malan and Prof T.M. Harms, for the guidance and support they provided throughout the course of this work. I would in particular like to thank Prof A.G. Malan for his valuable advise and contributions as well as for the use of his research code Elemental.

I would further like to express my gratitude to the CSIR who made this work possible through their financial support.

Many thanks to my colleges at the Advance Computational Methods research group for their interest and the insightful discussions. Special acknowledgement is given to Oliver Oxtoby for his support and advise in this work.

Finally, I would like to take the opportunity to thank my family for their support and interest in my work. To my wife, Anri, thank you very much for your endless support and encouragement.

Contents

Declaration	i
Abstract	ii
Uittreksel	iv
Acknowledgements	vi
Contents	vii
List of Figures	ix
List of Tables	xi
Nomenclature	xii
1 Introduction	1
1.1 Multi-phase flow	1
1.2 Modelling of multi-fluid flow	2
1.3 Numerical modelling	2
1.4 Objectives and research contributions	3
1.5 Overview	4
2 Weakly compressible formulation	6
2.1 Compressible multi-phase flow	6
2.2 Mathematical derivation	7
2.3 Closer	10
3 Numerical solver	12
3.1 Spatial discretisation	12
3.2 Split solver with artificial compressibility	15
3.3 Iterative implicit solver	17
3.4 Treatment of spatial discontinuities	21
3.5 Closer	23

CONTENTS

4	Free-surface interface capturing formulation	24
4.1	Overview of existing methods	24
4.2	Volume-of-fluid approach	26
4.3	Surface capturing formulation	28
4.4	Closer	35
5	Evaluation of the surface capturing formulation	36
5.1	Computational efficiency	36
5.2	Comparative analysis	36
5.3	Closer	47
6	Validation of the weakly compressible formulation	48
6.1	Forced compression and expansion of the gas	48
6.2	Gravity driven flow	50
6.3	Growth of a rising bubble	52
6.4	Horizontal shaker	53
6.5	Sloshing analysis of a partially filled tank	56
6.6	Closer	59
7	Conclusions and future work	60
A	Temporal discretisation	63
A.1	Explicit temporal discretisation	63
A.2	Implicit temporal discretisation	65
A.3	Large systems of equations	66
B	Spatial interpolation of the discretised advective face flux	69
B.1	Linear interpolation schemes	70
B.2	Non-linear interpolation schemes	72
B.3	Extension to unstructured meshes	77
C	Surface tension	79
D	Validation of the weakly compressible liquid-gas flow solver	82
	References	85

List of Figures

3.1	Construction of the median-dual-mesh on unstructured grids	13
3.2	Piece-wise linear interpolation of the pressure and step-wise interpolation of the density	22
4.1	Schematic representation of the normalised variable nomenclature on unstructured meshes	28
4.2	Bounded regions on the normalised variable diagram for explicit and implicit flow calculations	30
4.3	Comparison of the different weighting functions	33
5.1	CPU time for one-dimensional advection of a step function using CICSAM and HiRAC	37
5.2	Schematic representation of the advected square and round droplet . . .	38
5.3	Error plots of the advected square and round droplet	39
5.4	Contour plots of the convected square droplet, $c_f = 0.6$	39
5.5	Contour plots of the convected round droplet, $c_f = 0.6$	40
5.6	Schematic representation of the rotating key and the 70×70 structured mesh used for the analysis	40
5.7	Comparative error plot for the rotating key	41
5.8	Contour plots of the rotating key, $c_f = 0.6$	41
5.9	Schematic representation of the droplet in shear flow and the unstructured mesh used for the analysis	42
5.10	Comparative error plot for the droplet in shear flow	42
5.11	Contour plots of the droplet in shear flow just before the flow field is reversed, $c_f = 0.5$	43
5.12	Contour plots of the droplet in shear flow after initial shape is recovered, $c_f = 0.5$	43
5.13	Schematic representation of the falling droplet and the unstructured mesh used for the analysis	44
5.14	Diffusive error as a function of time for the falling droplet	44
5.15	Snapshots of the falling droplet	45
5.16	Contour plots, $\alpha = 0.5$, of the slotted sphere before and after translation and rotation	46

LIST OF FIGURES

6.1	Schematic of the quasi one-dimensional tube	49
6.2	Numerical results for the quasi one-dimensional tube	49
6.3	Schematic representation of gas bubble subjected to sinusoidal compression and expansion	50
6.4	Average pressure in the gas bubble during compression and expansion	51
6.5	Schematic of two columns of water at different fill levels and the unstructured 4000 node mesh	51
6.6	Average pressures in the gas pockets	52
6.7	Schematic representation of the rising gas bubble	53
6.8	Linear growth of the rising bubble	54
6.9	Schematic representation of the liquid subjected lateral excitation	54
6.10	Left sidewall pressure for the liquid subjected to sinusoidal excitation	55
6.11	Left sidewall pressure for the liquid subjected to a step function excitation	56
6.12	Partially filled tank with baffle configuration	57
6.13	Difference in average pressure measured on the left and right sidewall	57
6.14	Difference in average pressure measured the left and right side of the baffle	58
6.15	Contour plots ($\alpha = 0.1$, $\alpha = 0.5$ and $\alpha = 0.9$) for the weakly compressible formulation during the time frames of maximum impact pressure	58
B.1	Schematic representation of node points and edge faces on a one-dimensional grid	70
B.2	Schematic representation of a one-dimensional grid for the donor-acceptor formulation	73
B.3	Boundedness of the normalised variable to ensure monotonicity	73
B.4	Normalised variable diagram with the implicit convection boundedness criteria and various higher order schemes	74
B.5	One-dimensional stencil showing the left and right states of face, f	75
B.6	Admissible region for TVD second order schemes	77
B.7	Unstructured mesh	78
C.1	Static two-dimensional drop subjected to surface tension	81
D.1	Partially filled tank with baffle subjected to lateral excitation	82
D.2	Numerical and experimental predicted relative pressures	83
D.3	Numerical and experimental predicted absolute pressures	83

List of Tables

5.1	Material properties of the falling droplet	44
6.1	Material properties of the liquid and gas	48
6.2	Comparison of solver times	52

Nomenclature

\mathbf{A}_f	Outward pointing area vector (m^2)
\mathbf{A}	Temporal coefficient vector
\mathcal{A}	Surface (m^2)
\mathcal{A}_ξ	Surface bounding control volume ξ (m^2)
a_{ij}, b_i	Runge-Kutta coefficients
\mathbf{C}	Internal edge coefficient (m^2); or Flux Jacobian matrix
c	Acoustic velocity (m/s); or constant
c_α	Artificial compressive coefficient
c_f	Courant number
$c_{\tau conv}$	Convective pseudo acoustic velocity (m/s)
$c_{\tau diff}$	Diffusive pseudo acoustic velocity (m/s)
\mathbf{d}	Edge vector (m)
E_{comp}	Free-surface interface comparative error
E_{diff}	Free-surface interface diffusive error
E_{rms}	Root mean square error
\mathbf{F}	Inviscid flux matrix
\mathbf{G}	Viscous flux matrix
g	Gravitational acceleration (m/s^2)
h	Height (m)
k	Diffusive coefficient
k_γ	Weighting function coefficient

LIST OF TABLES

L	Edge length (m)
M	Mach number
\mathbf{n}	Unit normal vector (m)
N	Number of cells
N_{ba}	Matrix bandwidth
N_{eq}	Number of equations
p	Pressure (N/m ²)
R	Radius (m)
Res	Residual
\mathbf{r}	Right-hand side vector
r	Normalised variable gradient
\mathbf{S}	Source vector
S	Source term; or Strouhal number
s	Number of Runge-Kutta stages
\mathbf{t}	Edge vector (m)
t	Time (s)
u	Cell-averaged velocity (m/s)
u_c	Artificial compressive velocity (m/s)
u_i	Velocity component in cartesian coordinate direction i (m/s)
\mathbf{v}	Krylov space vectors
\mathcal{V}	Volume (m ³)
\mathcal{V}'_{ξ}	Discrete control volume associated with node ξ (m ³)
\mathbf{W}	Primitive variable vector
x_i	Cartesian spatial coordinate component i (m)
Greek symbols	
α	Volume fraction; or indicator function

LIST OF TABLES

β_f	Higher-resolution weighting function
$\Delta\chi$	Length scale (m)
Δ	Difference operator
δ_{ij}	Kronecker delta, $\delta = 1$ if $i = j$ and $\delta = 0$ if $i \neq j$
γ	Weighting factor for higher-resolution blending function
κ	Free-surface interface curvature; or higher order interpolation coefficient
λ	Eigenvalue
μ	Dynamic viscosity (kg/ms)
ϕ	Arbitrary scalar value
ψ	Slope limiter
ρ	Density (kg/m ³)
σ	Surface tension (N/m)
σ_{vN}	Von Neumann number, related to scaling of diffusive information propagation speed
Υ	Edge

Subscripts

A	Acceptor cell
analt	Analytical
avg	Average
D	Donor cell
η, ξ	Cell vertex
exp	Experimental
f	Edge face
g	Gas
HC	Hyper-C
i, j, k	Cartesian coordinates; or indicial notation

LIST OF TABLES

<i>l</i>	Liquid
max	Maximum
norm	Normal
num	Numerical
<i>o</i>	Reference value; or initial value
τ	Pseudo
tang	Tangential
<i>U</i>	Upwind cell
<i>UQ</i>	Ultimate-Quickest

Superscripts

θ	Time step ratio
<i>L</i>	Left
<i>n</i>	Time step
<i>R</i>	Right
*	Non-dimensional; smoothed; or intermediate value
~	Normalised values

Abbreviations

AC	Artificial compressibility
CBC	Convection boundedness criteria
CBS	Characteristic based split
CD	Central differencing
CFD	Computational fluid dynamics
CFL	Courant-Friedrichs-Lewy number
CG	Conjugate gradient
CICSAM	Compressive interface capturing scheme for arbitrary meshes
CSF	Continuum surface force

LIST OF TABLES

FSM	Free-surface modelling
GMRES	Generalised minimum residual
HiRAC	Higher-resolution artificial compressive scheme
LU-SGS	Lower-upper symmetric Gauss-Seidel
NV	Normalised variable
PP	Projected pressure
QUICK	Quadratic upstream interpolation for convective kinematics
RHS	Right-hand side
SOU	Second order upwinding
TVD	Total variation diminishing
VOF	Volume-of-fluid

Chapter 1

Introduction

Various forms of immiscible liquid-gas flow are encountered in industry and nature. Therefore, with the aim of developing of more efficient processes and optimised designs, various models attempt to accurately describe the free liquid surface and subsequently predict the dynamic characteristics of multi-fluid flow. To advance on existing methods and describe more complex flow phenomena with greater efficiency and accuracy these models are continuously extended and improved.

1.1 Multi-phase flow

Examples of industries that may benefit from accurate modelling of multi-fluid flow are numerous. Maritime and naval engineering require the prediction of wave impact loads on fixed and floating structures. Whereas, with the transportation of liquids it is necessary to accurately describe two-fluid flow as it greatly influences sloshing induced impact pressures measured on tank walls. For example, in commercial aircraft fuel can constitute approximately 50 % of take off weight and may be subjected to highly dynamic loading conditions. Due to potentially large sloshing induced loads, stringent restrictions are placed on tank fill levels of liquefied natural gas (LNG) carriers. Further examples of multi-fluid flow in industry include casting, aeration processes as well as condensation of refrigerants in coolers.

Most examples given here consider immiscible flow of a low density gas and a high density liquid under various flow regimes. The flow regimes range from segregated flow, through transitional or mixed flow up to dispersed flow or violent sloshing. This study focuses on modelling immiscible liquid-gas flow under a wide range of conditions and consider the extension of existing modelling techniques to improve on the solution accuracy and efficiency.

CHAPTER 1. INTRODUCTION

1.2 Modelling of multi-fluid flow

Due to the complex nature of multi-fluid liquid-gas flow, an analytical approach is typically not viable and traditionally most studies were limited to experimental analyses or simplified models. For example, in sloshing analyses simplified or lower order models are used to approximate the magnitude and frequency of impact loads on tank sidewalls. Although these low-fidelity models are computationally efficient, they are normally limited to a very narrow range of flow conditions and geometrical configurations. It is found that these models can often not provide an accurate representation of multi-fluid flow in and around intricate geometries.

Several researchers have furthermore argued that there are limitations to the experimental analysis of multi-fluid flow. Scardovelli and Zaleski (1999) argued that multi-fluid flow phenomena often occur on scales of time and space that are difficult to visualise experimentally and Godderidge *et al.* (2009b) noted that correct scaling of experimental models may be challenging. For experimental sloshing analyses the Froude scaling law is normally used. Lee *et al.* (2007) argued that with the Froude Law it is impossible to match all the relevant non-dimensional terms such as the viscosity, density ratio as well as the gas pressure and compressibility.

Difficulties associated with extrapolating scaled experimental results are discussed by Delorme *et al.* (2005). They noted that real tanks have a lower structural stiffness than smaller scaled experimental models and are, therefore, subjected to larger deformations. This may result in the effective pressure loads on the structure being lower than the experimentally predicted values. Uncertainties in the accuracy of experimental analyses result in the use of excessively large safety factors, subsequently leading to inefficient designs.

In recent years computational fluid dynamics (CFD) has developed to a point where it can provide a cost effective alternative for analysing two-fluid flow. Compared with simplified models and experimental analyses, CFD may provide a more practical approach to model a wide range of flow conditions. Numerical modelling or simulation is also more versatile; various geometrical configurations under a number of input conditions can be evaluated and compared, without the costly construction of new test models or the modification of existing setups.

1.3 Numerical modelling

With numerical two-fluid flow modelling or free-surface modelling (FSM), as it is commonly referred to, the flow is typically described using two sets of governing equations. It is, however, found that differences in the respective fluid properties results in discontinuities in the partial differential equations, introducing non-linearity into the coupled system of equations. This may result in the solution being ill-posed and increases the complexity of solving it numerically. If standard linear interpolation methods are used, the discontinuity in the partial differential equations may lead to spurious oscillations in the solution and render it unstable. Due to these

CHAPTER 1. INTRODUCTION

complexities, various aspects of FSM are continuously reviewed with the aim of improving on solution accuracy and efficiency.

An area within FSM that has been the subject of much interest is the modelling of the free-surface interface evolution. As it is required that an ever-increasing range of flow conditions be modelled, the accurate representation of the free-surface interface evolution becomes fundamental to the prediction of the flow dynamics. Various approaches have been proposed in literature (Terashima and Tryggvason, 2010; Chen *et al.*, 2009; Darwish and Moukalled, 2006; De Sousa *et al.*, 2004), however for this work the conservative volume-of-fluid (VOF) approach of Hirt and Nichols (1981) is followed.

The VOF method is preferred as it is computationally efficient; capable of modelling complex flow phenomena such as separation and merging of the interface; and ensures strict conservation of mass (Ubbink and Issa, 1999). With the VOF method the fluids are modelled by means of an advective volume fraction equation, where the respective fluids are represented by a volume fraction. As the interface is represented by partially filled cells, it is found that the VOF method is subject to numerical smearing of the interface.

To date, most free-surface flow solvers assume incompressible flow and neglect changes in density due to variations in pressure. Although this is a reasonable assumption for many flow regimes, in liquid-gas systems entrapped gas pockets and bubbles may be subjected to notable fluctuations in pressure. These changes are caused by large variations in the static pressure of the high density liquid when subjected to sizeable accelerations.

In these cases, it is suggested that the compressibility of the gas cannot be neglected as it may influence the predicted pressures. For example, experiments conducted by Faltinsen *et al.* (2005), Lugni *et al.* (2006), as well as Bullock *et al.* (2007) showed that the compressibility of air has a significant effect on the impact pressures measured on the tank walls during sloshing. They noted that the presence of the compressible air reduces the peak pressure levels, but increases the duration of the impact.

1.4 Objectives and research contributions

In light of the above, the current work aims to advance on existing volume-of-fluid FSM methods in two respects. First, to account for variations in gas density, a weakly compressible flow solver is developed that allows for computationally efficient analyses. Thereafter, a new compressive surface capturing scheme is developed to effect greater accuracy in the representation of the free-surface interface evolution. The new weakly compressible formulation and the compressive surface capturing scheme are implemented and evaluated using the *Elemental* software (Malan *et al.*, 2002a,b).

CHAPTER 1. INTRODUCTION

Weakly compressible two-fluid flow

As noted previously, under certain conditions it becomes necessary to account for variation in gas density. If a liquid-gas system under low Mach number flow conditions is considered, a non-dimensional analysis shows that the liquid may be treated as incompressible and the gas modelled using a weakly compressible approximation. As the variation in material properties introduces discontinuities over the free surface interface, the governing equations are discretised in a manner that ensures a stable, oscillatory free solution.

For the implementation of the weakly compressible formulation a vertex-centred edge-based finite volume approach (Zhao and Zhang, 2000) is followed. This approach is applicable to three-dimensional, unstructured meshes and the edge-based matrix-free approach furthermore allows for easy extension to parallel computing. The equations of motion are solved in a fully coupled manner using a split solver with artificial compressibility (Chorin, 1967). To achieve the coupling, the volume-of-fluid and momentum equations are discretised in time using a dual time-stepping approach, while to improve the rate of convergence a Generalised Minimum Residual (GMRES) solver with Lower-Upper Symmetric Gauss-Seidel (LU-SGS) preconditioning (Luo *et al.*, 1998) is used for the projected pressure equation. This allows for the efficient simulation of industrial sized problems that need to be analysed over an extended period of time.

Free-surface interface capturing formulation

Furthermore, a new Higher-Resolution Artificial Compressive (HiRAC) surface capturing formulation is developed. The new formulation uses a novel method of combining a higher-resolution scheme (Ubbink and Issa, 1999), used to interpolate the volume fraction face value, and the addition of an artificial compressive term to the VOF equation (Jasak and Weller, 1995). The combination of these methods ensures that the integrity of the free-surface interface is preserved while reducing the numerical smearing of the interface. The volume fraction equation, which is used to describe the free-surface interface evolution, is solved in a fully coupled manner and is discretised in a manner which ensures a bounded solution. Furthermore, the higher-resolution scheme is reformulated for improved computational efficiency.

1.5 Overview

The derivation of the weakly compressible formulation is presented in Chapter 2, where after the discretisation of the partial differential equations are discussed in Chapter 3. The development of the new Higher-Resolution Artificial Compressive (HiRAC) surface capturing formulation is considered in Chapter 4. In Chapter 5, the new surface capturing formulation is evaluated, where several benchmark test cases are considered to assess the improvement in accuracy. Thereafter, in Chapter 6,

CHAPTER 1. INTRODUCTION

the weakly compressible flow solver is validated against known analytical solutions and through application focused test cases the effect of the gas compressibility is investigated.

Chapter 2

Weakly compressible formulation

To date, most free-surface models treated both fluids as incompressible (e.g Liu and Lin, 2009; Waławczyk and Koronowicz, 2006; Löhner *et al.*, 2006; Ubbink and Issa, 1999) and assume the densities remain constant. This stems from the assumption that for low Mach number flows density is invariant with respect to pressure. In the majority of cases where relatively moderate flow conditions are considered this assumption holds true. However, with high density ratio liquid-gas systems subjected to appreciable accelerations it is found that entrapped gas pockets may be subjected to notable fluctuations in pressure.

2.1 Compressible multi-phase flow

It is suggested that under certain conditions it is necessary to account for compressibility to ensure an accurate representation of the flow dynamics. This is substantiated by experiments conducted by Faltinsen *et al.* (2005), Lugni *et al.* (2006) as well as Bullock *et al.* (2007) that suggested the compressibility of air has a measurable effect on the impact pressures measured on the tank walls during sloshing. They note that presence of the compressible air reduces the peak pressure levels, but increases the duration of the impact.

It is reasoned that entrapped air pockets or bubbles have a cushioning effect on the impact of breaking waves. In an experimental study, Abrahamsen and Faltinsen (2009) report of oscillatory behaviour in pressure measurements as entrapped pockets of air compress and expand. They noted that the pressure oscillation seems to decay in a manner similar to a dampened mass-spring system. Similar high frequency pressure oscillations were observed by Chen *et al.* (2009) when they considered compression and expansion of air during wave impact.

In light of this, it is evident that under certain conditions it is necessary to take into account the compressibility. Various authors (Liou *et al.*, 2007; Murrone and Guillard, 2005; Romenski and Toro, 2004) have presented high fidelity compressible multi-fluid models. These typically employ the seven equation Baer-Nunziato type model, where the flow is described by two continuity equations, two momen-

CHAPTER 2. WEAKLY COMPRESSIBLE FORMULATION

tum equations, two energy equations and a topological or interface equation. Some of these have been simplified to five equation models, which is said to be computationally more efficient.

With liquid-gas systems the material properties may vary by up to three orders of magnitude, introducing large discontinuities over the free-surface interface and result in such a system being numerically ill-posed. Furthermore, for low Mach number flows, the time scales permitted for long wavelength acoustic wave propagation is not aligned with the physical time scales typically of interest. Using these high fidelity approaches to model low Mach number high density ratio two fluid systems for an extended period of time is, therefore, deemed computationally overly expensive.

Song and Yuan (1988) presented a weakly compressible formulation for low Mach number single phase flow. By means of a non-dimensional analysis the governing equations were reconstructed and only the dominant terms were retained, allowing for a computationally efficient formulation. Chang *et al.* (2008) subsequently applied this approach to an averaged two-fluid flow model and used a single compressibility parameter to describe the fluids. The compressibility parameter is, however, a function of the square of the acoustic velocity, which for liquid-gas systems may differ by an order of magnitude. In passing it is noted that Bhajantri *et al.* (2007) and Song and Zhou (1999) have presented a weakly compressible formulation for free-surface flows; their formulations, however, only account for the liquid and neglect the description of the low density gas.

This work endeavours to extend on the above-mentioned work and, to this end, the following section presents a novel weakly compressible VOF formulation for immiscible high density ratio two-fluid flow under low Mach number conditions. This formulation solves the equations of motion describing both fluids while allowing for large differences in material properties of the fluids. For this purpose, the governing equation set is formulated to accurately account for the compressible properties of the gas phase, while ensuring the solution remains free from significant non-physical oscillations. In addition, it is solved in a manner which allows for efficient numerical simulation.

2.2 Mathematical derivation

If an Eulerian volume-of-fluid approach is followed, a control volume partially filled with liquid and gas can be considered. The volume fraction occupied by the liquid and the gas are respectively denoted α_l and α_g . Following this the governing equations for two-fluid flow can be derived from first principles.

For this work a homogeneous flow model is employed, which assumes a cell-averaged velocity and pressure, so that in a given cell $u_l = u_g = u$ and $p_l = p_g = p$ hold. Dias *et al.* (2010) explain that an averaged velocity can be assumed if the time scales on which the turbulent drag forces tend to equalise the velocity are smaller than the time scales on which the flow is averaged. It is furthermore suggested by

CHAPTER 2. WEAKLY COMPRESSIBLE FORMULATION

Godderidge *et al.* (2009a) that the homogeneous model provides better underlying numerical stability compared to the more complex models.

Considering the low Mach number application of this work, a weakly compressible formulation which assumes barotropic compression and expansion of the fluids is employed. Based on these assumptions, the continuity and momentum equations of respectively the liquid and gas simplify to read

$$\frac{\partial(\alpha_l \rho_l)}{\partial t} + \frac{\partial(\alpha_l \rho_l u_j)}{\partial x_j} = 0 \quad (2.1)$$

$$\frac{\partial(\alpha_l \rho_l u_i)}{\partial t} + \frac{\partial(\alpha_l \rho_l u_i u_j)}{\partial x_j} + \alpha_l \frac{\partial p}{\partial x_i} = \alpha_l S_{li} \quad (2.2)$$

$$\frac{\partial(\alpha_g \rho_g)}{\partial t} + \frac{\partial(\alpha_g \rho_g u_j)}{\partial x_j} = 0 \quad (2.3)$$

$$\frac{\partial(\alpha_g \rho_g u_i)}{\partial t} + \frac{\partial(\alpha_g \rho_g u_i u_j)}{\partial x_j} + \alpha_g \frac{\partial p}{\partial x_i} = \alpha_g S_{gi} \quad (2.4)$$

where the compatibility relation for the volume fractions holds, $\alpha_l + \alpha_g = 1$, and the liquid and gas volume fractions can, therefore, be expressed as $\alpha_l = \alpha$ and $\alpha_g = (1 - \alpha)$. The source terms, S_l and S_g , contain the hydro-static pressure terms as well as the viscous terms. If Newtonian flow is assumed, the following holds

$$S_{li} = \rho_l g_i + \frac{\partial}{\partial x_j} \left(\mu_l \frac{\partial u_i}{\partial x_j} \right) \quad (2.5)$$

$$S_{gi} = \rho_g g_i + \frac{\partial}{\partial x_j} \left(\mu_g \frac{\partial u_i}{\partial x_j} \right) \quad (2.6)$$

An averaged momentum equation for homogenous two-fluid flow is found by adding Eq. (2.2) and Eq. (2.4)

$$\frac{\partial(\rho u_i)}{\partial t} + \frac{\partial(\rho u_i u_j)}{\partial x_j} + \frac{\partial p}{\partial x_i} = S_i \quad (2.7)$$

where the mixture density and dynamic viscosity, expressed in terms of the volume fractions, are (Lafaurie *et al.*, 1994; Ubbink and Issa, 1999)

$$\rho = \alpha \rho_l + (1 - \alpha) \rho_g$$

$$\mu = \alpha \mu_l + (1 - \alpha) \mu_g$$

From the isentropic relation for the speed of sound, $c_l^2 = \partial p / \partial \rho_l$, (White, 2006) and by employing the product rule the liquid continuity equation (2.1) can be expanded and written as

$$\frac{\alpha}{c_l^2} \frac{\partial p}{\partial t} + \frac{\alpha u_j}{c_l^2} \frac{\partial p}{\partial x_j} + \rho_l \left(\frac{\partial \alpha}{\partial t} + \frac{\partial \alpha u_j}{\partial x_j} \right) = 0 \quad (2.8)$$

CHAPTER 2. WEAKLY COMPRESSIBLE FORMULATION

To evaluate the order of each term's contribution, Eq. (2.8) is cast into a non-dimensional form. The reference values used for pressure, $\rho_o u_o^2$, density, ρ_o , velocity, u_o , time, t_o , and length, l_o yield the non-dimensional form

$$\alpha S M_l^2 \frac{\partial p^*}{\partial t^*} + \alpha M_l^2 \left(u^* \frac{\partial p^*}{\partial x^*} \right) + \rho_l^* \left(S \frac{\partial \alpha}{\partial t^*} + \frac{\partial \alpha u_j^*}{\partial x_j^*} \right) = 0 \quad (2.9)$$

where * denotes non-dimensional quantities, $M_l = u_o/c_l$ is the liquid Mach number and $S = l_o/u_o t_o$ is the Strouhal number.

For low Mach number liquid-gas systems it is noted that the square of liquid Mach number, M_l , would be of order 10^{-7} . If the reference density, ρ_o , is taken to be of the same order as the gas density, the term ρ_l^* would be of order 10^3 . It is, therefore, acceptable to neglect the first two terms of Eq. (2.8) and as the liquid density will always be non-zero the following holds

$$\frac{\partial \alpha}{\partial t} + \frac{\partial(\alpha u_j)}{\partial x_j} = 0 \quad (2.10)$$

which is similar to the VOF equation for incompressible FSM.

Next, the product rule is applied to the gas continuity equation (2.3) and by rearranging the terms it yields

$$(1 - \alpha) \frac{\partial \rho_g}{\partial t} + (1 - \alpha) u_j \frac{\partial \rho_g}{\partial x_j} + \rho_g \frac{\partial u_j}{\partial x_j} - \rho_g \left(\frac{\partial \alpha}{\partial t} + \frac{\partial(\alpha u_j)}{\partial x_j} \right) = 0 \quad (2.11)$$

where the last term in brackets is the volume fraction equation (2.10) and equal to zero.

As pointed out previously, Song and Yuan (1988) presented a weakly compressible formulation for single phase flow with low Mach numbers. They showed via a non-dimensional analysis that the spatial derivative of pressure in the expanded continuity equation is negligibly small. A similar approach can be followed for two-fluid flow, where the gas continuity equation is cast into a non-dimensional form and the contribution of the respective terms evaluated. From the isentropic relation for the speed of sound, $c_g^2 = \partial p / \partial \rho_g$, it follows

$$(1 - \alpha) \frac{\partial p}{\partial t} + (1 - \alpha) u_j \frac{\partial p}{\partial x_j} + \rho_g c_g^2 \frac{\partial u_j}{\partial x_j} = 0 \quad (2.12)$$

with the non-dimensional version reading

$$(1 - \alpha) S M_g^2 \frac{\partial p^*}{\partial t^*} + (1 - \alpha) M_g^2 u_j^* \frac{\partial p^*}{\partial x_j^*} + \rho_g^* \frac{\partial u_j^*}{\partial x_j^*} = 0 \quad (2.13)$$

where $M_g = u_o/c_g$ is the gas Mach number and the square of M_g is of the order 10^{-6} . As previously noted, the reference density is of the same order as the gas

CHAPTER 2. WEAKLY COMPRESSIBLE FORMULATION

density and ρ_g^* is therefore of order unity. When considering low Mach number liquid-gas systems, the order of the terms would suggest that contribution of the spatial derivative of pressure can be neglected. When modelling the high frequency pressure oscillations during the compression and expansion of entrapped gas pockets, relatively small time scales are required. If, however, larger length scales are considered, the effect the temporal term cannot be neglected due to the increased contribution of the Strouhal number. From the non-dimensional analysis the gas continuity equation for weakly compressible flow thus simplifies to

$$\frac{(1 - \alpha) \partial \rho_g}{\rho_g \partial t} = - \frac{\partial u_j}{\partial x_j} \quad (2.14)$$

which also holds for the incompressible liquid phase as it then reads $\partial u_i / \partial x_i = 0$.

For the weakly compressible formulation the compression and expansion of the gas can be approximated by a linear form of the ideal gas law

$$\rho_g - \rho_{g0} = \frac{1}{c_g^2} (p - p_0) \quad (2.15)$$

where ρ_{g0} and p_0 is the initial gas density and pressure.

From the non-dimensional analysis, it is implied that the gradient in the gas density is negligibly. To ensure consistency in the momentum equation it is required that the hydro-static source term in the gas phase be neglected. This is, however, acceptable as the hydro-static pressure is a function of the density, which for the gas is three orders of magnitude smaller than the hydro-static pressure of the liquid.

2.3 Closer

To conclude, a new weakly compressible VOF formulation is presented. The VOF equation, the gas continuity equation and the averaged momentum equation describing low Mach number immiscible liquid-gas flow read

$$\frac{\partial \alpha}{\partial t} + \frac{\partial(\alpha u_j)}{\partial x_j} = 0 \quad (2.16)$$

$$\frac{(1 - \alpha) \partial \rho_g}{\rho_g \partial t} = - \frac{\partial u_j}{\partial x_j} \quad (2.17)$$

$$\frac{\partial(\rho u_i)}{\partial t} + \frac{\partial(\rho u_i u_j)}{\partial x_j} + \frac{\partial p}{\partial x_i} = \frac{\partial}{\partial x_j} \left(\mu \frac{\partial u_i}{\partial x_j} \right) + \alpha \rho_l g_i \quad (2.18)$$

where ρ and μ are the mixture density and viscosity.

The formulation takes into consideration changes in gas density due to variations in pressure; it describes both fluids and accounts for differences in the liquid-gas material properties. Apart from neglecting the gas hydro-static pressure in the momentum equation, only the continuity equation differs from the incompressible

CHAPTER 2. WEAKLY COMPRESSIBLE FORMULATION

formulation as it now contains a conditional temporal term. As the conditional temporal term is only activated in the gas phase, it results in a discontinuity in the velocity gradient. In Chapter 3 the underlying numerical solver deployed is described as well as the interpolation of the discontinuous pressure and velocity terms. The numerical approximation of the VOF equation is considered in Chapter 4.

Chapter 3

Numerical solver

In the previous chapter a new weakly compressible VOF formulation for liquid-gas systems was derived. As noted in the introduction, these equations are discretised using an unstructured vertex-centred edge-based finite volume approach. This approach is preferred as the edge-based data structure is computationally more efficient than element-based approaches (Luo *et al.*, 1994) and the vertex-centred variant of finite volume scheme is more efficient in terms of memory usage compared to cell-centred (De Foy and Dawes, 2000; Zhao and Zhang, 2000). Furthermore, the edge-based matrix-free implementation ensures an efficient extension to parallel computing.

3.1 Spatial discretisation

The weakly compressible FSM formulation can be described through a single unified governing equation

$$\mathbf{A} \frac{\partial \mathbf{W}}{\partial t} + \frac{\partial \mathbf{F}^j}{\partial x_j} - \frac{\partial \mathbf{G}^j}{\partial x_j} = \mathbf{S} \quad (3.1)$$

where

$$\mathbf{W} = \begin{pmatrix} \alpha \\ \rho_g \\ \rho u_i \end{pmatrix}, \quad \mathbf{F}^j = \begin{pmatrix} \alpha u_j \\ u_j \\ \rho u_i u_j + \delta_{ij} p \end{pmatrix}, \quad \mathbf{G}^j = \begin{pmatrix} 0 \\ 0 \\ \mu \frac{\partial u_i}{\partial x_j} \end{pmatrix},$$

$$\mathbf{A} = \begin{pmatrix} 0 \\ \frac{1-\alpha}{\rho_g} \\ 0 \end{pmatrix}, \quad \mathbf{S} = \begin{pmatrix} 0 \\ 0 \\ \alpha \rho_l g_i + \mu \frac{\partial}{\partial x_j} \left(\frac{\partial u_i}{\partial x_j} \right) \end{pmatrix}$$

With the said finite volume approach, the spatial domain, \mathcal{V} , is subdivided into a finite number of non-overlapping volumes, $\mathcal{V}_\xi \in \mathcal{V}$. The dual-mesh construction for the vertex-centred approach as proposed by Vahdati *et al.* (1989) is illustrated in

CHAPTER 3. NUMERICAL SOLVER

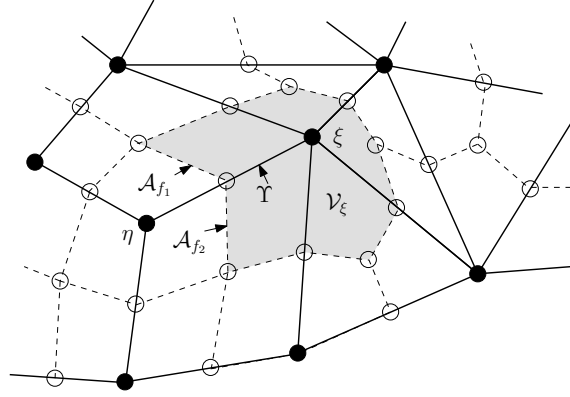


Figure 3.1: Construction of the median-dual-mesh on unstructured grids

Figure 3.1. By integrating over the finite volume, \mathcal{V}_ξ , the general governing equation can be cast into weak form and from the divergence theorem can subsequently be written in terms of surface integrals

$$\int_{\mathcal{V}_\xi} \mathbf{A} \frac{\partial \mathbf{W}}{\partial t} d\mathcal{V} + \int_{\mathcal{A}_\xi} (\mathbf{F}^j - \mathbf{G}^j) n_j d\mathcal{A} = \int_{\mathcal{V}_\xi} \mathbf{S} d\mathcal{V} \quad (3.2)$$

where \mathcal{A}_ξ is the surface bounding \mathcal{V}_ξ and \mathbf{n} is the unit vector normal to the boundary segment \mathcal{A} pointing outward.

To exploit the computational advantages of an edge-based assembly, bounding surface information is stored in an edge-wise manner, as edge-coefficients. Edge-coefficients are defined as

$$\mathbf{C}_f = \mathbf{n}_{f_1} \mathcal{A}_{f_1} + \mathbf{n}_{f_2} \mathcal{A}_{f_2} \quad (3.3)$$

where f denotes the face value.

The hyperbolic or convective terms, which are composed of the product of primitive variables, are approximated numerically as

$$\int_{\mathcal{A}_\xi} \mathbf{F}^j n_j d\mathcal{A} \approx \sum_{\Upsilon \cap \mathcal{V}_\xi} \bar{F}_f^j \mathbf{C}_f^j \quad (3.4)$$

where \bar{F}_f^j is the interpolated face flux along the edge Υ .

If face flux is interpolated using linear second order central differencing, it is found to introduce spurious oscillations in the locality of sharp gradients. To stabilise the solution the face flux can be interpolated using non-linear higher order interpolation schemes (see Appendix B). These schemes are monotonic and prevent the creation of new local extrema, consequently, keeping the solution from diverging. In support of an oscillatory free solution, non-linear higher order schemes provide an automated solution without the adjustment of various empirical coefficients.

CHAPTER 3. NUMERICAL SOLVER

With the edge-based finite volume approach the elliptic or diffusive terms are typically computed with two loops over the edges. Using the divergence theorem, the first derivative is approximated in the first loop

$$\mu \frac{\partial u_i}{\partial x_j} \Big|_{\xi} \approx \mu_{\xi} \overline{\frac{\partial u_i}{\partial x_j}} \Big|_{\xi} = \frac{\mu_{\xi}}{\mathcal{V}_{\xi}} \int_{A_{\xi}} u_i n_j d\mathcal{A} = \frac{\mu_{\xi}}{\mathcal{V}_{\xi}} \sum_{\Upsilon \cap \mathcal{V}_{\xi}} u_f^i C_f^j \quad (3.5)$$

where u_f^i is the velocity face value, which is interpolated using central differencing. Thereafter, setting $G^{ij} = \mu \frac{\partial u_i}{\partial x_j}$, the viscous term is discretised as

$$\int_{A_{\xi}} \mu \frac{\partial u_i}{\partial x_j} n_k d\mathcal{A} \approx \sum_{\Upsilon \cap \mathcal{V}_{\xi}} \overline{G^{ij}}_f C_f^k \quad (3.6)$$

If $\overline{G^{ij}}_f$ is approximated as described above the contribution of the direct neighbouring nodes are nullified, which may lead to odd-even decoupling of the solution. To rectify this, Crumpton *et al.* (1997) proposed the use of a compact stencil strategy which involves splitting $\overline{G^{ij}}_f$ into components tangential and normal to the edge

$$\overline{G^{ij}}_f = (\overline{G^{ij}}_f|_{\text{tang}} + \overline{G^{ij}}_f|_{\text{norm}}) \quad (3.7)$$

In a similar fashion as presented in Malan *et al.* (2007), the tangential component or directional derivative along the edge is calculated as

$$\overline{G^{ij}}_f|_{\text{tang}} = \mu_f \frac{u_{\eta} - u_{\xi}}{|\mathbf{x}_{\eta} - \mathbf{x}_{\xi}|} t_j \quad (3.8)$$

with \mathbf{t} designating the unit vector tangential to the edge, Υ . From vector algebra, the normal component is calculated using the average flux $\overline{G^{ij}}_f$, initially computed in Eq. (3.5)

$$\overline{G^{ij}}_f|_{\text{norm}} = \overline{G^{ij}}_f - (\overline{G^{ik}}_f t_k) t_j \quad (3.9)$$

so that Eq. (3.6) becomes

$$\int_{A_{\xi}} \mu \frac{\partial u_i}{\partial x_j} n_k d\mathcal{A} \approx \sum_{\Upsilon \cap \mathcal{V}_{\xi}} (\overline{G^j}_f|_{\text{tang}} + \overline{G^j}_f|_{\text{norm}}) C_f^k \quad (3.10)$$

For typical isotropic meshes with reasonable alignment of the edge-coefficient and the associated edge, the contribution of the five stencil normal component is limited and the greatest contribution from the tangential component is based on a three node stencil. This technique is computationally only marginally more expensive and provides an elegant method of improving the accuracy while still conserving the edge-based approach.

3.2 Split solver with artificial compressibility

To solve the coupled Navier-Stokes equations, Zienkiewicz and Taylor (2000) presented a characteristic based split (CBS) method which follows a similar process to the split method of Chorin (1968). Zienkiewicz and Taylor (2000) state that the CBS method provides a unified approach to solve both compressible and incompressible flow and is applicable to explicit and semi-implicit temporal discretisation. They further note that with compressible flow the explicit formulation of the scheme compares computationally well with existing schemes and the additional cost associated with splitting the operator is insignificant.

Pressure split with upwind-biased stabilisation

To solve the incompressible Navier-Stokes equations, Nithiarasu (2003) introduced artificial compressibility (AC) in an explicit form to the CBS method. In essence, this approach combines the pressure projection (PP) method and the artificial compressibility method in a manner that retains the preferred features of each. With the AC method the large compressible wave speed, c , that causes the numerical stiffness of the system and imposes a severe time step restriction on the solution is replaced with an appropriate artificial parameter, c_τ . This parameter is computed locally to account for different flow regimes, convection and diffusion dominated. Nithiarasu (2003) noted that by combining the two methods, the stability and robustness of the PP method is retained with the added computational efficiency of the AC approach. The split solver with AC was extended for application to edge-based finite volume by Malan and Lewis (2011).

Following a similar procedure, Malan and Oxtoby (2010) and Oxtoby and Malan (2011) combined an upwind-stabilised pressure-projection split with artificial compressibility. They found that by employing the pressure-projection split with higher-order upwinding of the face fluxes sufficient numerical diffusion is introduced to ensure a stable solution. The pressure-projection split solver consist of three steps, first an intermediate momentum equation, from which the pressure gradients are removed, is solved explicitly *viz.*

$$\frac{\Delta \rho u_i^*}{\Delta t} = - \left. \frac{\partial(\rho u_i u_j)}{\partial x_j} \right|^n + \mu \frac{\partial}{\partial x_j} \left(\frac{\partial u_i}{\partial x_j} \right)^n \quad (3.11)$$

where $\Delta \rho u_i^* = \rho u_i^* - \rho u_i|^n$ and $\Delta t = t^{n+1} - t^n$.

The continuity equation is expanded as follows, including additional second order elliptic terms

$$\begin{aligned} \frac{(1-\alpha)}{\rho_g} \frac{1}{c_g^2} \frac{p^{n+1} - p^n}{\Delta t} &= - \left. \frac{\partial u_j}{\partial x_j} \right|^{n+1} = - \left. \frac{\partial u_j}{\partial x_j} \right|^n - \frac{\partial \Delta u_j}{\partial x_j} \\ &= - \frac{\partial}{\partial x_j} \left[u_j^n + \Delta u_j^* + \frac{\Delta t}{\rho} \left(- \frac{\partial p^{n+1}}{\partial x_j} + \alpha \rho_l g \right) \right] \end{aligned} \quad (3.12)$$

CHAPTER 3. NUMERICAL SOLVER

for which the temporal term is only activated in the gas phase. The said artificial compressibility is applied to the weakly compressible continuity equation. As the introduction of AC destroys the temporal accuracy, a dual-time-stepping formulation is employed where the pressure is solved iteratively in pseudo-time for every real time step

$$\left[\frac{\alpha}{c_{\tau l}^2} + \frac{(1-\alpha)}{c_{\tau g}^2} \right] \frac{p^{\tau+1} - p^{\tau}}{\Delta t_{\tau}} + \frac{(1-\alpha)}{\rho_g} \frac{1}{c_g^2} \frac{p^{\tau} - p^n}{\Delta t} = - \frac{\partial}{\partial x_j} \left[u_j^n + \Delta u_j^* + \frac{\Delta t}{\rho} \left(- \frac{\partial p^{\tau}}{\partial x_j} + \alpha \rho_l g \right) \right] \quad (3.13)$$

where Δt_{τ} is the pseudo time step and c_{τ} is the pseudo-acoustic velocity or artificial compressibility parameter.

As described later on, the artificial compressibility is a function of the convective and diffusive velocities. Therefore, as an averaged velocity is assumed with the homogeneous two-fluid model it is possible to use a single pseudo-acoustic velocity, c_{τ} . Furthermore, the temporal derivative that accounts for changes in gas density can be treated explicitly as a source term on the right-hand side. Taking this into consideration the projected pressure equation using artificial compressibility with dual time-stepping reads

$$\frac{1}{c_{\tau}^2} \frac{p^{\tau+1} - p^{\tau}}{\Delta t_{\tau}} = - \frac{\partial}{\partial x_j} \left[u_j^{\tau} + \Delta u_j^* + \frac{\Delta t}{\rho} \left(- \frac{\partial p^{\tau}}{\partial x_j} + \alpha \rho_l g \right) \right] - \frac{(1-\alpha)}{\rho_g} \frac{1}{c_g^2} \frac{p^{\tau} - p^n}{\Delta t} \quad (3.14)$$

Finally, in the third step the velocities are calculated from the corrected momentum equation which contains the updated values

$$\frac{\Delta \rho u_i^{n+1}}{\Delta t} = \frac{\Delta \rho u_i^{*\tau}}{\Delta t} - \frac{\partial p^{n+1}}{\partial x_i} + \alpha \rho_l g \quad (3.15)$$

By employing a dual time-stepping approach velocity, pressure and volume fraction can be solved in a fully coupled manner. The dual time-stepping form of the momentum equation reads

$$\frac{\rho u_i^{\tau+1} - \rho u_i^{\tau}}{\Delta t_{\tau}} = \frac{\Delta \rho u_i^{*\tau}}{\Delta t} - \frac{\partial p^{\tau+1}}{\partial x_i} + \alpha \rho_l g - \frac{\rho u_i^{\tau} - \rho u_i^n}{\Delta t} \quad (3.16)$$

where Δt_{τ} is the pseudo time step.

Artificial compressibility parameter

To avoid numerical experimentation and ensure general applicability, Malan *et al.* (2002a) suggested an automated procedure for calculating the artificial compressibility parameter (pseudo-acoustic velocity) and the associated pseudo-time step

CHAPTER 3. NUMERICAL SOLVER

size. As noted previously, the artificial compressibility parameter is computed to hold for both convection and diffusion dominated flows as considered respectively by Turkel (1987) and Choi and Merkle (1993)

$$c_\tau = \max(0.3 u_{max}, c_{\tau conv}, c_{\tau diff}) \quad (3.17)$$

where u_{max} is the maximum velocity magnitude in the domain. This prevents the artificial compressibility parameter of becoming zero at stagnation points.

Turkel (1987) suggested that in the inviscid limit the artificial parameter should be kept as close as possible to the local convective velocity for best convergence rates. To compute the convective pseudo-acoustic velocity the following relation is used

$$c_{\tau conv} = 1.1 \sqrt{u_i u_i} \quad (3.18)$$

The diffusive pseudo-acoustic velocity is determined by a relation that takes into account the viscous diffusion velocity

$$c_{\tau diff} = \frac{\mu}{\rho \Delta \chi \sigma_{vN}} + |u| \quad (3.19)$$

where σ_{vN} is the von Neumann number and in general is taken as 0.5 (Zienkiewicz and Taylor, 2000). The length scale is given by

$$\Delta \chi = \sqrt{\Delta x_i \Delta x_i} \quad (3.20)$$

When calculating the local value for c_τ , the restriction on the pseudo time step size should be taken into consideration to ensure the local stability criteria are met. The largest allowable pseudo time step for the dual volume, \mathcal{V}_ξ is calculated as

$$\Delta t_{\tau \xi} = \frac{CFL \Delta \chi_\xi}{\lambda_\xi} \quad (3.21)$$

where according to Malan *et al.* (2002a) the maximum eigenvalue, λ , is

$$\lambda = \frac{1}{2} \left(|u| + \sqrt{|u| |u| + 4c_\tau^2} \right) \quad (3.22)$$

This procedure automates the calculation of the artificial compressibility parameter at each computational cell for a wide range of flow conditions and only requires the adjustment of the global Courant-Friedrichs-Lewy (CFL) number.

3.3 Iterative implicit solver

For industrially applicable problems the system of unknowns tend to become extremely large as a significant number of discrete volumes are needed for an accurate approximation. Furthermore, with the weakly compressible formulation, the

CHAPTER 3. NUMERICAL SOLVER

projected pressure equation is subjected to relatively slow rates of convergence, resulting in lengthy computational times. As a sparse non-symmetric system of equations is recovered from the finite volume discretisation of the flow equations, an iterative implicit solver is employed to solve the pressure equation and improve the rates of convergence.

Generalised Minimum Residual solver

Luo *et al.* (1998) developed a matrix-free implicit method for unstructured meshes. This method consisted of solving a system of approximated linear equations through the use of a Generalised Minimum Residual (GMRES) method with Lower-Upper Symmetric Gauss-Seidel (LU-SGS) preconditioning. It is suggested that this approach provides significant improvements in performance over existing iterative implicit solvers, while its memory requirements are similar to that of explicit schemes. The authors have furthermore implemented and demonstrated the applicability of the scheme to parallel computing (Luo *et al.*, 2003).

Malan *et al.* (2007) used GMRES with LU-SGS preconditioning to solve a non-linear diffusion equation. In calculating the flux Jacobian, they employed a semi-analytical approximation instead of the backward difference approximation or incremental flux vector normally used. The semi-analytical approach avoids step-size sensitivities associated with the previous methods and furthermore the flux Jacobians are only computed once per GMRES iteration, reducing the computational overhead.

The aim of this work is to extend the existing GMRES solver with LU-SGS preconditioning as presented in Malan *et al.* (2007) to the weakly compressible FSM formulation. The focus of this study, therefore, falls on determining the semi-analytical approximation of the Jacobian matrix. The reader is referred to Appendix A for a discussion on the GMRES solver with LU-SGS preconditioning.

Semi-analytical approximation of the flux Jacobians

The semi-discrete pressure projection equation (3.14) employing a Jacobian-type dual time-stepping formulation reads

$$\frac{1}{c_\tau^2} \frac{p^{\tau+1} - p^\tau}{\Delta t_\tau} = -\frac{\partial}{\partial x_j} \left[u_j^\tau + \Delta u_j^* + \frac{\Delta t}{\rho} \left(-\frac{\partial p^\tau}{\partial x_j} + \alpha \rho_l g \right) \right] - \frac{(1-\alpha)}{\rho_g} \frac{1}{c_g^2} \frac{p^\tau - p^n}{\Delta t}$$

where the discrete form, which is found using the edge-based dual-volume finite volume approach described in Section 3.1, can be grouped into pressure dependent

CHAPTER 3. NUMERICAL SOLVER

and non-dependent terms

$$\begin{aligned}
 \frac{1}{c_\tau^2} \frac{p_\xi^{\tau+1} - p_\xi^\tau}{\Delta t_\tau} &= -\frac{1}{\mathcal{V}_\xi} \left[-\sum_{\Upsilon \cap \mathcal{V}_\xi} \frac{\Delta t}{\rho} \frac{\partial p^\tau}{\partial x_j} \Big|_f \cdot C_f + \frac{(1-\alpha)}{\rho_g} \frac{1}{c_g^2} \frac{p_\xi^\tau - p_\xi^n}{\Delta t} \mathcal{V}_\xi \right. \\
 &\quad \left. + \sum_{\Upsilon \cap \mathcal{V}_\xi} \left\{ u_f^j + \Delta u_j^*|_f + \frac{\Delta t}{\rho} (\alpha \rho_l g)|_f \right\}^\tau \cdot C_f \right] \\
 &= -\frac{1}{\mathcal{V}_\xi} \left[A_\xi(p^\tau) + B_\xi \right] \\
 &= \text{Res}_\xi^\tau
 \end{aligned} \tag{3.23}$$

where Res_ξ^τ denotes the residual at node ξ and tends to zero as the solution converges in pseudo-time.

By using Newton and linearising Eq. (3.23) in time the following approximation is found

$$\frac{1}{c_\tau^2} \frac{\Delta \mathbf{p}^\tau}{\Delta t_\tau} = \mathbf{Res}^\tau + \frac{\partial \mathbf{Res}^\tau}{\partial \mathbf{p}} \cdot \Delta \mathbf{p}^\tau \tag{3.24}$$

which can be rewritten as

$$C \cdot \Delta \mathbf{p}^\tau = \mathbf{Res}^\tau \tag{3.25}$$

where C contains the Jacobian matrix, $\partial \mathbf{Res}^\tau / \partial \mathbf{p}$, and reads

$$C = \frac{1}{c_\tau^2} \frac{I}{\Delta t_\tau} - \frac{\partial \mathbf{Res}^\tau}{\partial \mathbf{p}} \tag{3.26}$$

and I is the identity matrix.

To solve this system and find the increment in pressure, Δp , GMRES with LU-SGS preconditioner is employed. When computing the Jacobian Matrix, C , the term $\partial \mathbf{Res}^\tau / \partial p$ needs to be approximated. As suggested by Malan *et al.* (2007) the residual gradient used in the linearised form of equation (3.24) is calculated using a semi-analytical approximation

$$\begin{aligned}
 \frac{\partial \text{Res}_\xi^\tau}{\partial p} &\approx \frac{\partial}{\partial p} \left[-\frac{1}{\mathcal{V}_\xi} \left(A(p^\tau) + B \right) \right] \\
 &= -\frac{1}{\mathcal{V}_\xi} \frac{\partial}{\partial p} \left(A(p^\tau) \right)
 \end{aligned} \tag{3.27}$$

In Section 3.1 it is shown that the discretised elliptic term can be approximated using the compact stencil formulation. For meshes where the edge-coefficient aligns well with the associated edge, it is found that the contribution of the normal component is small in comparison to the tangential term. Taking this into consideration

CHAPTER 3. NUMERICAL SOLVER

and neglecting the normal component, the Jacobian can be approximated as follows

$$\begin{aligned} \frac{\partial \text{Res}_\xi^\tau}{\partial p} \approx & -\frac{1}{\mathcal{V}_\xi} \frac{\partial}{\partial p} \left[- \sum_{\Gamma \cap \mathcal{V}_\xi} \frac{2\Delta t}{(\rho_\xi + \rho_\eta)} \frac{p_\eta^\tau - p_\xi^\tau}{|\mathbf{x}_\eta - \mathbf{x}_\xi|} t_j C_f^j \right. \\ & \left. + \frac{(1-\alpha)}{\rho_g} \frac{1}{c_g^2} \frac{p_\xi^\tau - p_\xi^n}{\Delta t} \mathcal{V}_\xi \right] \end{aligned} \quad (3.28)$$

where $\rho_g = \rho_g(p^\tau)$.

Start by considering the first term in the square brackets. By evaluating the derivative for the internal node ξ the semi-analytical expressions for the diagonal terms of the Jacobian matrix are found

$$\begin{aligned} \frac{\partial}{\partial p_\xi} \left[\sum_{\Gamma \cap \mathcal{V}_\xi} \frac{2\Delta t}{(\rho_\xi + \rho_\eta)} \frac{p_\eta^\tau - p_\xi^\tau}{|\mathbf{x}_\eta - \mathbf{x}_\xi|} t_j C_f^j \right] \\ = 2\Delta t \sum_{\Gamma \cap \mathcal{V}_\xi} \left[\frac{1}{(\rho_\xi + \rho_\eta)} \frac{-1}{|\mathbf{x}_\eta - \mathbf{x}_\xi|} + \frac{p_\eta^\tau - p_\xi^\tau}{|\mathbf{x}_\eta - \mathbf{x}_\xi|} \frac{\partial}{\partial p_\xi} \left(\frac{1}{\rho_\xi + \rho_\eta} \right) \right] t_j C_f^j \end{aligned} \quad (3.29)$$

where

$$\frac{\partial}{\partial p_\xi} \left(\frac{1}{\rho_\xi + \rho_\eta} \right) = \frac{-(1-\alpha)}{c_g^2 (\rho_\xi + \rho_\eta)^2} \quad (3.30)$$

In a similar fashion the semi-analytical expression for the off-diagonal terms are found by considering the partial derivative for the neighbouring node η

$$\begin{aligned} \frac{\partial}{\partial p_\eta} \left[\sum_{\Gamma \cap \mathcal{V}_\xi} \frac{2\Delta t}{(\rho_\xi + \rho_\eta)} \frac{p_\eta^\tau - p_\xi^\tau}{|\mathbf{x}_\eta - \mathbf{x}_\xi|} t_j C_f^j \right] \\ = 2\Delta t \sum_{\Gamma \cap \mathcal{V}_\xi} \left[\frac{1}{(\rho_\xi + \rho_\eta)} \frac{1}{|\mathbf{x}_\eta - \mathbf{x}_\xi|} + \frac{p_\eta^\tau - p_\xi^\tau}{|\mathbf{x}_\eta - \mathbf{x}_\xi|} \frac{-(1-\alpha)}{c_g^2 (\rho_\xi + \rho_\eta)^2} \right] t_j C_f^j \end{aligned} \quad (3.31)$$

Malan *et al.* (2007) note that a Gauss-Seidel type loop over the mesh is required to calculate these Jacobian terms. The loop iterates over the nodes and at each node over all the edges. They note that the computational effort is comparable to a single residual calculation and is therefore at least an order of magnitude less costly than the backward difference approach.

Now, consider the derivative of the second term in the square brackets of equation 3.28. By means of the quotient rule this term simplifies as follows

$$\frac{\partial}{\partial p_\xi} \left[\frac{(1-\alpha)}{\rho_g} \frac{1}{c_g^2} \frac{p_\xi^\tau - p_\xi^n}{\Delta t} \mathcal{V}_\xi \right] = \frac{(1-\alpha)}{c_g^2} \frac{\mathcal{V}_\xi}{\Delta t} \left[\frac{1}{\rho_g} - \frac{(p_\xi^\tau - p_\xi^n)}{\rho_g^2} \frac{\partial \rho_g}{\partial p_\xi} \right] \quad (3.32)$$

CHAPTER 3. NUMERICAL SOLVER

From the isentropic relation for the speed of sound it follows $\partial p / \partial \rho_g = c_g^2$. As the last term contains the coefficient $1/c_g^4$, which is negligible for the large acoustic velocities, the approximation of Equation (3.32) reads

$$\frac{\partial}{\partial p_\xi} \left[\frac{(1-\alpha)}{\rho_g} \frac{1}{c_g^2} \frac{p_\xi^{\bar{\tau}} - p_\xi^{\bar{n}}}{\Delta t} \mathcal{V}_\xi \right] \approx \frac{(1-\alpha)}{\rho_g} \frac{1}{c_g^2} \frac{\mathcal{V}_\xi}{\Delta t} \quad (3.33)$$

3.4 Treatment of spatial discontinuities

As described earlier, the intermediate momentum equation (3.11), projected pressure equation (3.14) and corrected momentum equation (3.16) are discretised using an edge-based finite volume approach. It is, however, found that standard linear interpolation of the discretised equations' face fluxes causes spurious oscillations in the solution. This results from the large difference in material properties of the liquid and gas as well as the introduction of a conditional temporal term in the continuity equation.

Pressure interpolation

Löhner *et al.* (2006) noted that if the density of the liquid and gas varies significantly, small changes in the pressure gradient over the interface will induce inaccurate acceleration of the gas. This consequently results in the formation of spurious oscillations in the velocity field over the interface. To overcome this, Panahi *et al.* (2006) discretised the spatial pressure derivative in a piece-wise linear manner. They noted that for incompressible free-surface flow the velocity field is continuous throughout the domain, so that for a given edge, Υ ,

$$\frac{1}{\rho} \frac{\partial p}{\partial x} \Big|_{\Upsilon} \approx c \quad (3.34)$$

where c is a constant.

In Eq. (3.34) the edge face value of the pressure is calculated using a piece-wise linear approximation, while the density is treated as a nodal value which is interpolated in a stepwise manner (see Figure 3.2). For the weakly compressible formulation the contribution of the hydro-static pressure in the gas phase is neglected, resulting in a discontinuous source term. The piece-wise linear interpolation of Panahi *et al.* (2006) is extended to include the discontinuous source term

$$\left[\frac{1}{\rho} \frac{\partial p}{\partial x} - \frac{S_g}{\rho} \right]_{\Upsilon} = c \quad (3.35)$$

Similar to the interpolation presented by Panahi *et al.* (2006), the pressure is treated as piece-wise linear and the density as piece-wise constant. Similar to the

CHAPTER 3. NUMERICAL SOLVER

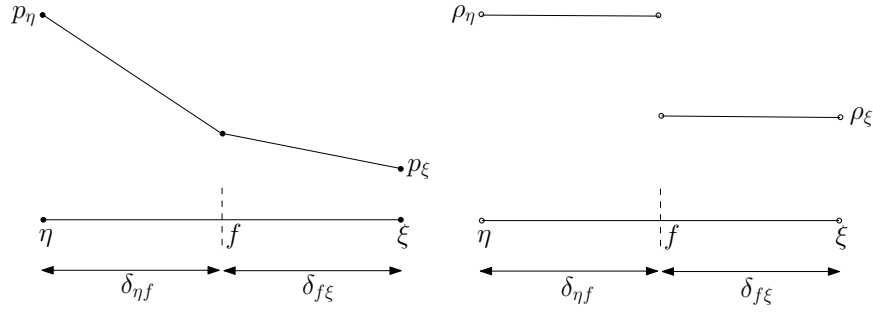


Figure 3.2: Piece-wise linear interpolation of the pressure and step-wise interpolation of the density

density, the newly introduced discontinuous source term is computed using a piece-wise constant approximation. Eq. (3.35) is integrated from node, η , to the edge face, f , to find an expression for p_f in terms of the pressure at node η

$$\int_{\eta}^f \frac{1}{\rho} \frac{\partial p}{\partial x} - \frac{S_g}{\rho} dx = \int_{\eta}^f c dx \quad (3.36)$$

which yields

$$p_f - p_{\eta} = \frac{\rho_{\eta} L}{2} \left(\frac{S_{\eta}}{\rho_{\eta}} + c \right) \quad (3.37)$$

where L is the edge length.

In a similar fashion, by integrating from the edge face, f , to node ξ a face pressure in terms of the pressure and source term at node ξ is obtained

$$p_{\xi} - p_f = \frac{\rho_{\xi} L}{2} \left(\frac{S_{\xi}}{\rho_{\xi}} + c \right) \quad (3.38)$$

The face pressure in terms of the pressures and source terms at node η and ξ is found by subtracting Eq. (3.37) from Eq. (3.38)

$$p_f = \frac{\rho_{\eta} p_{\xi} + \rho_{\xi} p_{\eta}}{\rho_{\eta} + \rho_{\xi}} + \frac{\rho_{\eta} \rho_{\xi} L}{2(\rho_{\eta} + \rho_{\xi})} \left(\frac{S_{\eta}}{\rho_{\eta}} - \frac{S_{\xi}}{\rho_{\xi}} \right) \quad (3.39)$$

To find an expression for the constant, c , in terms of the known variables Eq. (3.37) and Eq. (3.38) is added. Through some manipulation the following expression for c is found

$$c = \frac{p_{\xi} - p_{\eta}}{\frac{L}{2}(\rho_{\eta} + \rho_{\xi})} - \frac{S_{\eta} + S_{\xi}}{\rho_{\eta} + \rho_{\xi}} \quad (3.40)$$

where the previous two expressions are substituted into the projected pressure equation (3.14) and corrected momentum equations (3.16).

CHAPTER 3. NUMERICAL SOLVER

Velocity interpolation

The extension of the incompressible FSM formulation to account for changes in the density involves the addition of a temporal term to the gas phase. It is found that this may result in a sharp change in the velocity gradient over the free-surface interface (as demonstrated in Chapter 6). To ensure an oscillatory free and stable solution, the discretised advective face flux is interpolated using a non-linear higher order slope limiting scheme (Appendix B.2).

At sharp discontinuities, the gradient slope is limited to prevent the creation of new extrema; this is done by recovering a first order scheme in the immediate vicinity of high gradients. To limit the amount of numerical dissipation, the limiter recovers the original higher order discretisation in the smooth regions. It is found that good results are obtained by employing the MUSCL scheme of van Leer as quoted by Waterson and Deconinck (2007) and Blazek (2001). The extension for unstructured meshes presented by Zhao *et al.* (2002) is used in this study (Appendix B.3).

3.5 Closer

In this chapter the discretisation of the weakly compressible formulation using a vertex-centred finite volume approach was discussed along with the implementation of a projected-pressure split solver with artificial compressibility. To improve convergence rates the projected pressure equation is solved using an advanced GMRES solver with LU-SGS preconditioner, for which the semi-analytical flux Jacobians for the weakly compressible formulation are derived. Furthermore, to ensure an oscillatory free solution, procedures for the interpolation of the pressure and velocity face values were reviewed.

Chapter 4

Free-surface interface capturing formulation

In Chapter 2 the governing equations for a weakly compressible liquid-gas flow were derived using the volume-of-fluid approach, where the free-surface interface evolution is described using the VOF equation (2.10). It is found that the VOF equation remains unchanged from the incompressible formulation and similar methods can be implemented.

4.1 Overview of existing methods

One of the approaches used when modelling the evolution of the free-surface is Lagrangian surface fitting methods (De Sousa *et al.*, 2004; Ferziger and Perić, 1999; Clarke and Issa, 1997), where the interface is fitted to the mesh. These methods are, however, limited in the flow phenomena that they can model, as large interface deformations lead to a highly distorted mesh that requires continuous re-meshing. Furthermore, complex procedures are required to model the merging and break-up of the interface. With Eulerian approaches the fluids can either be modelled by means of so-called volume tracking methods or by means of interface or front tracking techniques. Here, the propagation of respectively the volume or the interface is computed based on the local velocity.

Interface tracking methods include massless particles on the interface (Terashima and Tryggvason, 2010; Popinet and Zaleski, 1999; Unverdi and Tryggvason, 1992), height functions (López and Hernández, 2010; Farmer *et al.*, 1994) and level set methods (Chen *et al.*, 2009; Sethian, 2003; Sussman *et al.*, 1999). Interface or front tracking methods are, however, non-conservative (Cassidy *et al.*, 2009; Tsui *et al.*, 2009; Bonometti and Magnaudet, 2007) and are limited in their application to complex flow phenomena such as separation and merging of fluids. Extensions to overcome these limitations tend to increase the complexity of these methods as well as the computational overhead.

With volume tracking methods the fluids are either represented with massless

CHAPTER 4. FREE-SURFACE INTERFACE CAPTURING FORMULATION

particles or with a volume fraction indicator function, where the latter is commonly referred to as the volume-of-fluid (VOF) approach. With these methods the exact position of the interface is unknown and special algorithms are required to describe a well defined interface. With the Marker-and-Cell (MAC) and smooth particle hydrodynamics (SPH) approaches, the fluid of interest is represented by mass-less particles that are spread over the volume occupied by that fluid (Reddy and Radosavljevic, 2006; Armenio and Rocca, 1996; Hwang and Stoehr, 1988). Babaei *et al.* (2006) note that these methods are computationally expensive and are not well posed in the description of boundary conditions.

In contrast, VOF volume tracking methods use a volume fraction advection equation to describe the evolution of the fluid volume. These methods are capable of conserving mass (Raessi *et al.*, 2010; Gopala and van Wachem, 2008; Cummins *et al.*, 2005) and have been shown to be effective in modelling separation and merging of fluids. To maintain a sharp interface and ensure the volume fraction remains bounded, two approaches have been proposed *viz.* discretising the advective term using non-linear higher-resolution schemes or adding an artificial compressive term to the VOF equation.

With non-linear higher-resolution schemes the volume fraction face value, α_f , can be interpolated using either the normalised variable (NV) approach of Leonard (1991) with convective boundedness criteria (CBC), or a flux-limiting method employing a total variation diminishing (TVD) condition. The NV approach with CBC is preferred as the availability criteria can easily be evaluated (Ubbink, 1997). It is, however, noted that flux-limiting schemes with TVD are employed by Tsui *et al.* (2009) and Cassidy *et al.* (2009). Further advantages of the NV approach is discussed in depth by inter alia Waclawczyk and Koronowicz (2008), Ubbink and Issa (1999) and Leonard (1991).

Though NV higher-resolution schemes are highly compressive and capable of maintaining a sharp interface, they are inclined to distort or wrinkle the interface when the free surface is not aligned with the edge face. As a result Lafaurie *et al.* (1994) developed a scheme that switches between compressive downwinding and diffusive upwinding to maintain the integrity of free-surface interface shape while preventing artificial smearing of the interface. Based on this concept various authors developed schemes that blend compressive and more diffusive schemes, where they are blended based on the alignment of the free-surface interface and the control volume or edge face. These are commonly referred to as blended high-resolution surface capturing schemes and examples of them include STACS of Darwish and Moukalled (2006), CICSAM of Ubbink and Issa (1999), HRIC of Muzafferija *et al.* (1998) and SURFER of Lafaurie *et al.* (1994).

Blended higher-resolution schemes tend to be computationally efficient; are easily implemented on unstructured three-dimensional meshes; and can be applied in modelling complex flow phenomena such as separation and merging of the interface. However, the degree of numerical smearing is directly proportional to the time step size and furthermore the interface sharpness cannot be recovered once

CHAPTER 4. FREE-SURFACE INTERFACE CAPTURING FORMULATION

smearing has occurred.

As an alternative to the blended higher-resolution schemes, Rusche (2002) and Jasak and Weller (1995) introduced an artificial compressive term into the VOF equation to achieve the necessary compression of the interface. Gopala and van Wachem (2008) showed that the Inter-Gamma scheme of Jasak and Weller (1995), with the artificial compressive term, is capable of maintaining a sharp interface, but tends to wrinkle the shape of the free-surface interface. Takatani (2007) introduced an additional anti-diffusion step to sharpen the interface, where the anti-diffusion coefficient is only activated in the interface and is scaled according to the Courant number.

With the aim of accurately modelling free-surface flow, this work builds on existing VOF free-surface interface capturing methods and presents the development of a new Higher-Resolution Artificial Compressive (HiRAC) formulation. Through a novel combination of a higher-resolution scheme and the addition of an artificial compressive term, the new formulation provides improved accuracy when modelling the interface evolution. Building on the strengths of these methods, HiRAC reduces the numerical diffusivity while it preserves the integrity of the interface shape. Furthermore, to improve the computational efficiency the normalised variable approach used in the development of the higher-resolution scheme is reformulated and a new blending function for the higher-resolution scheme is proposed.

4.2 Volume-of-fluid approach

Volume fraction

To describe the evolution of the free-surface interface, an advective volume fraction equation is employed. This equation, which is commonly referred to as the VOF equation, holds for both incompressible flow as well as the newly derived weakly compressible formulation (see equation 2.10). The VOF equation reads

$$\frac{\partial \alpha}{\partial t} + \frac{\partial}{\partial x_i} (\alpha u_i) = 0$$

where the volume fraction is defined as

$$\alpha(x_i, t) = \begin{cases} 1 & \text{for the point } (x_i, t) \text{ inside the liquid} \\ 0 & \text{for the point } (x_i, t) \text{ inside the gas} \end{cases} \quad (4.1)$$

The VOF equation is discretised using an edge-based vertex-centred finite volume method described in Chapter 3. To this effect the VOF equation is spatially discretised at a node ξ as

$$\frac{\partial \alpha}{\partial t} \int_{\mathcal{V}_\xi} d\mathcal{V}_\xi + \sum_{\Gamma_\xi \cap \mathcal{V}_\xi} \alpha_f u_f^j C_f^j = 0 \quad (4.2)$$

CHAPTER 4. FREE-SURFACE INTERFACE CAPTURING FORMULATION

where f denotes values at the face of the control volume, \mathcal{V}_ξ^f . The edge coefficient is defined as

$$\mathbf{C}_f = \mathbf{n}_{f1} \mathcal{A}_{f1} + \mathbf{n}_{f2} \mathcal{A}_{f2} \quad (4.3)$$

where \mathbf{n} is the outward pointing unit vector normal to the control volume bounding surface, \mathcal{A}_ξ .

Normalised variable approach

To ensure an accurate solution when modelling free-surface flow, a sharp interface between the fluids needs to be maintained while the volume fraction is kept within its physical bounds of zero and one. To achieve this the volume fraction face flux, α_f , is interpolated using a blended higher-resolution scheme.

As noted above, the NV approach with CBC is preferred for the formulation of the blended higher-resolution scheme. In this section a general introduction to the NV approach is presented, however, for a more in-depth discussion the reader is referred to Appendix B. Start by considering the expression for the normalised variable

$$\tilde{\alpha} = \frac{\alpha - \alpha_U}{\alpha_A - \alpha_U} \quad (4.4)$$

where the upwind, donor and acceptor cells are, respectively, denoted U , D and A .

To ensure a bounded solution when the NV approach is used to compute the normalised face value, $\tilde{\alpha}_f$, the convective boundedness criteria are typically employed. Leonard (1991) adjusted the implicit CBC of Gaskell *et al.* (1988) for explicit discretisation by introducing a linear weighting based on the cell Courant number, c_f . The explicit formulation of CBC reads

$$\begin{aligned} \tilde{\alpha}_D \leq \tilde{\alpha}_f \leq \min\left\{1, \frac{\tilde{\alpha}_D}{c_f}\right\} & \quad \text{for } 0 \leq \tilde{\alpha}_D \leq 1 \\ \tilde{\alpha}_f = \tilde{\alpha}_D & \quad \text{for } \tilde{\alpha}_D < 0 \text{ or } \tilde{\alpha}_D > 1 \end{aligned} \quad (4.5)$$

For an unstructured formulation of the NV approach, the expression for the projected upwind value (Figure 4.1) as presented by Ubbink and Issa (1999) is used

$$\alpha_U^* = \alpha_A - 2(\nabla\alpha)_D \cdot \mathbf{d} \quad (4.6)$$

where the edge vector is defined as $\mathbf{d} = \mathbf{x}_A - \mathbf{x}_D$.

Artificial compressive term

To achieve a sharp free-surface interface Jasak and Weller (1995) presented an alternative approach to discretising the volume fraction face flux, α_f , using a blended higher-resolution scheme. They introduced an artificial compressive term into the

CHAPTER 4. FREE-SURFACE INTERFACE CAPTURING FORMULATION

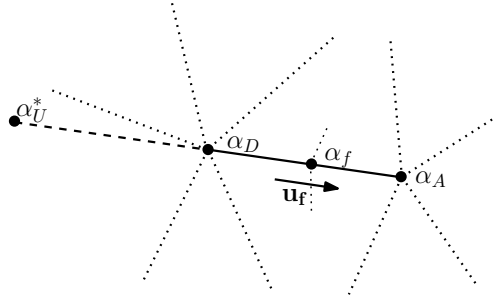


Figure 4.1: Schematic representation of the normalised variable nomenclature on unstructured meshes

VOF equation to reduce the numerical smearing of the interface. If the said artificial compressive term is added to the VOF equation (2.10) the following equation is obtained

$$\frac{\partial \alpha}{\partial t} + \nabla \cdot (u_i \alpha) + \nabla \cdot (u_c | \alpha (1 - \alpha)) = 0 \quad (4.7)$$

where the term $\alpha(1 - \alpha)$ ensures that the artificial compressive term is only activated in the interface region and does not affect the rest of the domain. The compressive velocity, u_c , is proportional to the unit vector normal to the interface, \mathbf{n}_α , ensuring optimal compression of the interface

$$\mathbf{u}_c = c_\alpha |u_f| \mathbf{n}_\alpha \quad (4.8)$$

where

$$\mathbf{n}_\alpha = \frac{\nabla \alpha}{|\nabla \alpha|} \quad (4.9)$$

and c_α is a compressive coefficient and $|u_f|$ is the magnitude of the face velocity.

4.3 Surface capturing formulation

In Section 4.1, it was argued that each of the VOF approaches presented above has its own strengths and weaknesses. Blended higher-resolution methods are capable of maintaining the integrity of the interface shape, but tend to become diffusive at higher Courant numbers. On the other hand, with the approach of adding an artificial compressive term it is possible to ensure a sharp free-surface interface at high Courant numbers, but it tends to result in the wrinkling of the interface shape. From the mathematical formulation it is apparent that these approaches can easily be combined.

CHAPTER 4. FREE-SURFACE INTERFACE CAPTURING FORMULATION

Higher resolution artificial compressive formulation

As part of this work a new blended Higher-Resolution Artificial Compressive (HiRAC) formulation is proposed. This formulation aims to reduce the Courant number related numerical smearing while maintaining a well defined free-surface interface shape. The method involves discretising the volume fraction face flux using a blended higher-resolution scheme, but in addition introduces an artificial compressive term to the VOF equation. As the face flux is discretised using a compressive higher-resolution scheme, the degree of additional compression needed from the artificial term is limited, preventing it from distorting the shape of the free-surface interface.

The formulation of the new HiRAC method is divided into three parts: Firstly, the appropriate temporal discretisation of the VOF equation is considered, based on the availability criteria restrictions; secondly, a computationally efficient blended higher-resolution approach for discretising the face flux is presented; and finally, the implementation of the artificial compressive term is considered.

Temporal discretisation

In Figure 4.2 the regions for which the convection boundedness criteria ensure a bounded solution are shown. The dark grey area represents the bounded region for an explicit solution and the lighter grey area represents the extended region for an implicit solution. It is suggested that the upper bound of CBC provides the most compressive solution with the sharpest interface and therefore as the Courant number increases the explicit solution tends towards the more diffusive upwind differencing.

Due to the explicit schemes' dependence on the c_f number, Hoekstra *et al.* (2007), Hogg *et al.* (2006) and Darwish and Moukalled (2006) employ implicit formulations to achieve more compressive solutions at larger time steps. Considering the non-linear higher-resolution discretisation schemes, it is noted that they are a function of both the flow direction as well as the local shape or gradient of the volume fraction. As the gradient is unknown at the latest time step, an approximation needs to be made for the implicit formulation. Using Crank-Nicolson for the temporal discretisation, Ubbink and Issa (1999) noted that if small time steps are taken a weighting factor, β_f , can be approximated using the value at the previous time step. The weighting factor which is a function of the local shape and orientation of the volume fraction and is defined as

$$\beta_f = \frac{\tilde{\alpha}_f - \tilde{\alpha}_D}{1 - \tilde{\alpha}_D} \quad (4.10)$$

and is used to calculate the actual volume fraction face value

$$\alpha_f = (1 - \beta_f)\alpha_D + \beta_f\alpha_A \quad (4.11)$$

If larger time steps are taken the approximation of β_f would be inaccurate and the solution may become unbounded, as the amount of fluid projected into or out of

CHAPTER 4. FREE-SURFACE INTERFACE CAPTURING FORMULATION

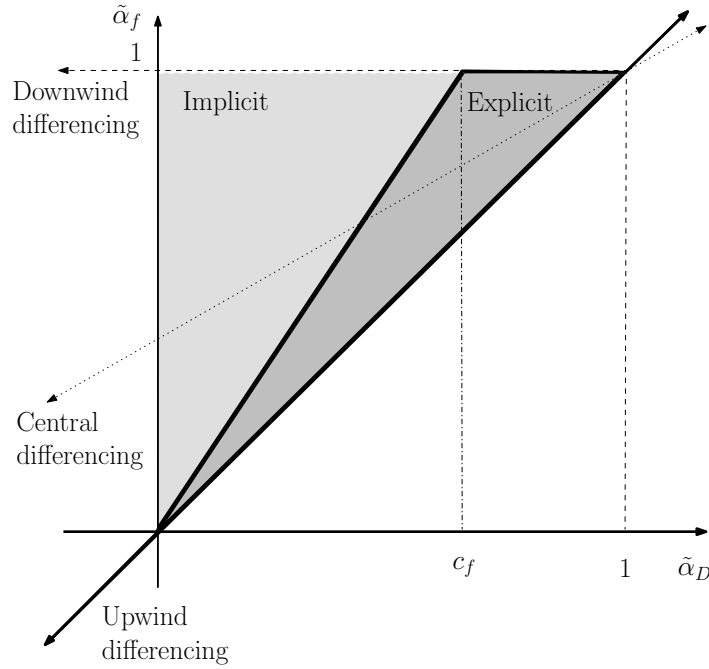


Figure 4.2: Bounded regions on the normalised variable diagram for explicit and implicit flow calculations

the cell may exceed the available amount. Therefore, although the implicit schemes are not dependant on the c_f number and tend to be more compressive for larger time steps, it is suggested that for larger time steps the degree to which the solution will be unbounded will also increase. Furthermore, it is noted that the interface is localised to relatively small regions of the domain and it would most likely be computationally inefficient to use costly implicit solvers.

It is found that explicit schemes tend to become diffusive for larger time steps and the approximated implicit schemes result in a costly, unbounded solution. For the purpose of this work, it is proposed that a Jacobi-type solver with dual time-stepping be employed, where the volume fraction equation is solved in pseudo-time, t_τ . This approach results in the advection of the volume fraction being broken up into pseudo sub-steps, providing an efficient way of implementing the sub-stepping philosophy suggested by Gopala and van Wachem (2008).

As proposed by Ubbink (1997), HiRAC employs a second order Crank-Nicholson formulation, but introduces a Jacobi-type dual time-stepping approach. The semi-discrete VOF equation with the addition of an artificial compressive term reads

$$\frac{\alpha^{\tau+1} - \alpha^\tau}{\Delta t_\tau} + \frac{\alpha^\tau - \alpha^n}{\Delta t} = -\frac{1}{2} \left[\left| \frac{\partial(u_i \alpha)}{\partial x_i} \right|^\tau + \frac{\partial(u_i \alpha)}{\partial x_i} \right]^n - \frac{\partial}{\partial x_i} [u_c |i \alpha (1 - \alpha)|]^\tau \quad (4.12)$$

where the implicit solution is approached as it converges in pseudo-time. As the

CHAPTER 4. FREE-SURFACE INTERFACE CAPTURING FORMULATION

volume fraction is evaluated at every pseudo time step and the availability criteria satisfied, no approximation of a weighting factor needs to be made. The dual time-stepping formulation is therefore better enabled to provide a bounded and compressive solution at higher c_f numbers.

Higher-resolution formulation

As mentioned above, the volume fraction face value is interpolated using the NV approach with CBC to ensure a monotonic solution. Whereas, for the interpolation of the velocity face value in the advective term, it is found that by employing a linear third-order upwinding scheme acceptable results are obtained. This section therefore focuses on the formulation of a suitable interpolation scheme for the volume fraction face value.

Numerous studies have compared different blended higher-resolution schemes, where CICSAM and HRIC are most commonly used as references in the comparative analyses. Hoekstra *et al.* (2007) show that CICSAM performs better than HRIC, but note that both schemes are highly dependent on the Courant number, c_f , as well as grid refinement. Similar conclusions are made by Tsui *et al.* (2009), Waławczyk and Koronowicz (2008) and Gopala and van Wachem (2008). They found that CICSAM preserves the shape of the interface more accurately, maintaining a sharper interface. They note that the interface smears as the c_f number increases.

For CICSAM, Ubbink and Issa (1999) suggest the use of the compressive Hyper-C differencing scheme which follows the upper bound of the CBC and helps to maintain a sharp free-surface interface. HRIC utilises a Bounded Downwind scheme, which is similar to Hyper-C (Darwish and Moukalled, 2006). The explicit form of Hyper-C expressed in terms of the normalised variables of Eq. (4.4) is

$$\tilde{\alpha}_{f_{HC}} = \begin{cases} \min\left\{1, \frac{\tilde{\alpha}_D}{c_f}\right\} & \text{for } 0 \leq \tilde{\alpha}_D \leq 1 \\ \tilde{\alpha}_D & \text{for } \tilde{\alpha}_D < 0 \text{ or } \tilde{\alpha}_D > 1 \end{cases} \quad (4.13)$$

As the system is solved in pseudo-time, the discretised face values used in the dual time-stepping formulation at time step τ and n can be calculated directly. This makes it possible to reformulate the Hyper-C scheme for improved computational efficiency. This is achieved by expanding the normalised variables so that the discretised face value is calculated directly, reducing the number of computations. For HiRAC, Eq. (4.13) can be rewritten in terms of the actual volume fractions

$$\alpha_{f_{HC}} = \begin{cases} \min\left\{\alpha_A, \frac{\alpha_D - \alpha_U^*}{c_f} + \alpha_U^*\right\} & \text{for } r^* > 1 \text{ and } \alpha_D > \alpha_U^* \\ \max\left\{\alpha_A, \frac{\alpha_D - \alpha_U^*}{c_f} + \alpha_U^*\right\} & \text{for } r^* > 1 \text{ and } \alpha_D < \alpha_U^* \\ \alpha_D & \text{for } r^* \leq 1 \end{cases} \quad (4.14)$$

CHAPTER 4. FREE-SURFACE INTERFACE CAPTURING
FORMULATION

where the gradient, r^* is defined as

$$r^* = \frac{\alpha_A - \alpha_U^*}{\alpha_D - \alpha_U^*} \quad (4.15)$$

To preserve the shape of the free-surface interface, CICSAM blends the compressive Hyper-C scheme with the more diffusive ULTIMATE-QUICKEST scheme of Leonard (1991). HRIC and STACS, on the other hand, use respectively Upwind and STOIC (Darwish and Moukalled, 2006). Based on the findings of Tsui *et al.* (2009) and Waławczyk and Koronowicz (2006) when comparing blended higher-resolution schemes, HiRAC also employs ULTIMATE-QUICKEST which reads

$$\tilde{\alpha}_{f_{UQ}} = \begin{cases} \min \left\{ \frac{8c_f \tilde{\alpha}_D + (1-c_f)(6\tilde{\alpha}_D+3)}{8}, \tilde{\alpha}_{f_{HC}} \right\} & \text{for } 0 \leq \tilde{\alpha}_D \leq 1 \\ \tilde{\alpha}_D & \text{for } \tilde{\alpha}_D < 0 \text{ or } \tilde{\alpha}_D > 1 \end{cases} \quad (4.16)$$

In a similar manner as was done for Hyper-C, the computational efficiency of ULTIMATE-QUICKEST can be improved by expanding the normalised variables. For HiRAC Eq. (4.16) can be written in terms of the actual volume fractions

$$\tilde{\alpha}_{f_{UQ}} = \begin{cases} \min \{ k^*, \alpha_{f_{HC}} \} & \text{for } r^* > 1 \text{ and } \alpha_D > \alpha_U \\ \max \{ k^*, \alpha_{f_{HC}} \} & \text{for } r^* > 1 \text{ and } \alpha_D < \alpha_U \\ \alpha_D & \text{for } r^* \leq 1 \end{cases} \quad (4.17)$$

where r^* is the same as in Equation (4.15) and

$$k^* = \alpha_U + \left[\frac{3+c_f}{4} \right] (\alpha_D - \alpha_U) + \frac{3(1-c_f)}{8} (\alpha_A - \alpha_U) \quad (4.18)$$

For blended higher-resolution schemes a weighting factor, γ , is used to switch between the compressive and more diffusive schemes based on the alignment of the free-surface interface and edge face, yielding a blended face value

$$\tilde{\alpha} = \gamma_f \tilde{\alpha}_{f_{HC}} + (1 - \gamma_f) \tilde{\alpha}_{f_{UQ}} \quad (4.19)$$

The weighting function suggested by Ubbink and Issa (1999) to blend the compressive and diffusive schemes is

$$\gamma_f = \min \left\{ k_\gamma \frac{\cos(2\theta_f) + 1}{2}, 1 \right\} \quad (4.20)$$

where they recommend $k_\gamma = 1$ and

$$\theta_f = \arccos \left| \frac{(\nabla \alpha)_D \cdot \mathbf{d}}{|(\nabla \alpha)_D| \cdot |\mathbf{d}|} \right| \quad (4.21)$$

CHAPTER 4. FREE-SURFACE INTERFACE CAPTURING
FORMULATION

Tsui *et al.* (2009) and Darwish and Moukalled (2006) used the following switching formulation

$$\gamma_f = \cos^4(\theta_f) \quad (4.22)$$

For improved computational efficiency, it is suggested that the following formulation be used to compute the weighting factor

$$\gamma_f = \min((\eta_f)^m, 1) \quad (4.23)$$

where

$$\eta_f = \left| \frac{(\nabla\alpha)_D \cdot \mathbf{d}}{|(\nabla\alpha)_D| \cdot |\mathbf{d}|} \right| \quad (4.24)$$

In Figure 4.3 the new weighting factor is plotted as a function of η_f , alongside existing weighting factors. For $m = 2$ the new formulation reduces to the weighting function of Ubbink and Issa (1999), for $k_\gamma = 1$, and for $m = 4$ it reduces to the scheme of Tsui *et al.* (2009) and Darwish and Moukalled (2006). As m is increased the interpolation becomes more biased towards the diffusive higher-resolution scheme. For this study $m = 2$ is used as it is found that it provides a good balance between the compressive and diffusive higher-resolution schemes.

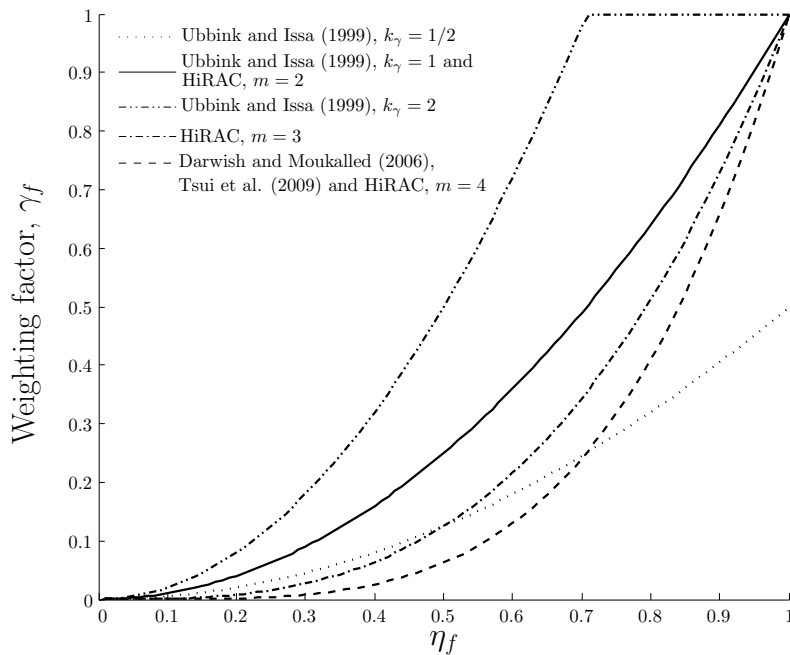


Figure 4.3: Comparison of the different weighting functions

CHAPTER 4. FREE-SURFACE INTERFACE CAPTURING
FORMULATION

Artificial compressive term

To reduce the inherent numerical diffusivity associated with the higher-resolution schemes, an additional artificial compressive term is introduced into the VOF equation. The semi-discrete VOF equation with the artificial compressive term now follows at the dual volume \mathcal{V}_ξ :

$$\frac{\partial \alpha}{\partial t} \int_{\mathcal{V}_\xi} d\mathcal{V} + \sum_{\Upsilon_\xi \cap \mathcal{V}_\xi} \alpha_f u_f^j C_f^j + \sum_{\Upsilon_\xi \cap \mathcal{V}_\xi} \alpha_f (1 - \alpha_f) u_{cf}^j C_f^j = 0 \quad (4.25)$$

Considering the discretised artificial compressive term, the interpolation of the volume fraction face value, α_f , was discussed in the previous section and the compressive velocity is computed as described in Section 4.2. The compressive coefficient, c_α , needs to be selected according to the temporal and spatial discretisation used. Rusche (2002), using the Inter-Gamma scheme of Jasak and Weller (1995), states that $c_\alpha = 1.5$ is desirable. For HiRAC with the compressive blended higher-resolution spatial interpolation and the second-order temporal discretisation, it is found that good results were obtained with a compressive coefficient value of $c_\alpha = 0.5$ (see Section 5). The required contribution from the artificial compressive term with HiRAC is therefore notably less than for the Inter-Gamma scheme.

As the volume fraction undergoes a sharp change in gradient over the free-surface interface, it is found that the vector normal to the interface is calculated inaccurately if Eq. (4.9) is discretised directly. To remedy this a smoothed volume fraction value, α^* , is used to calculate \mathbf{n}_α

$$\mathbf{n}_\alpha^* = \frac{\nabla \alpha^*}{|\nabla \alpha^*|} \quad (4.26)$$

Various methods can be used to smooth the volume fraction, where the convolution of α with a smooth integration kernel is most commonly implemented (Cummins *et al.*, 2005; Williams *et al.*, 1998; Brackbill *et al.*, 1992). Ubbink and Issa (1999) note that for an edge-based approach only the information of the two nodes connected to the edge is known and it may become costly to extend the method beyond the direct neighbouring nodes of each cell. This is particularly the case on three-dimensional unstructured meshes. Ubbink and Issa (1999) therefore employed a Laplacian filter, \mathcal{F} , recommended by Lafaurie *et al.* (1994), and adapted it for unstructured meshes

$$\mathcal{F}(\alpha) = \frac{\sum_{f=1}^n \alpha_f |\mathbf{A}_f|}{\sum_{f=1}^n |\mathbf{A}_f|} \quad (4.27)$$

where α_f is determined using central differencing and \mathbf{A}_f is the outward pointing area vector. The filter is repeated m times yielding a smooth function, where it is typical to use $m = 2$.

CHAPTER 4. FREE-SURFACE INTERFACE CAPTURING FORMULATION

Rusche (2002) on the other hand smoothed the volume fraction by means of elliptic relaxation

$$\left[\nabla \cdot \left(\left(\frac{c}{|\mathbf{d}|} \right)^2 \nabla \alpha^* \right) \right] = \alpha^* + \alpha \quad (4.28)$$

where \mathbf{d} is the edge vector and the smoothed volume fraction, α^* , is solved using a costly, implicit solver.

As part of this work a pseudo-explicit diffusive equation is employed to smooth α . With this formulation, the volume fraction is smoothed by evolving the equation in pseudo time

$$\frac{\alpha^{*\tau+1} - \alpha^{*\tau}}{\Delta\tau} + \nabla \cdot \nabla \alpha^{*\tau} = 0 \quad (4.29)$$

where typically 2 iterations are needed.

4.4 Closer

In this chapter the formulation and implementation of a new VOF surface capturing scheme was presented. The temporal and spacial discretisation of the VOF equation was considered along with the implementation of combining an artificial compressive term with a blended higher-resolution scheme. For added computational efficiency the normalised variable approach used in the development of the higher-resolution scheme was reformulated and a new higher-resolution blending function proposed.

Chapter 5

Evaluation of the surface capturing formulation

To benchmark the proposed HiRAC formulation, it is evaluated against the surface capturing schemes CICSAM (Ubbink and Issa, 1999) and Inter-Gamma (Jasak and Weller, 1995); these are chosen as HiRAC builds on them. As CICSAM is typically used in benchmarking surface capturing schemes (Tsui *et al.*, 2009; Waławczyk and Koronowicz, 2008; Gopala and van Wachem, 2008), it provides a good point of reference to assess the increase in accuracy as well as improvement in efficiency.

5.1 Computational efficiency

To evaluate the improvement in computational efficiency of the reformulated higher-resolution interpolation of the volume fraction face value presented in Section 4.3, the advection of a one-dimensional step function is considered. To measure the possible gain in CPU time the normalised gradient of Eq. (4.24) is assumed to be $\eta_f = 0.5$, so that the combined computational cost of the reformulated Hyper-C and ULTIMATE-QUICKEST schemes as well as the new weighting function could be measured. In Figure 5.1 the CPU cost as a function of mesh size is shown. It is noted that for HiRAC a computational gain of approximately 45 % may be realised when solving the VOF equation. It is found that the largest contribution follows the reformulation of the normalised variable approach and the contribution from the new weighting function is approximately 10 %.

5.2 Comparative analysis

To evaluate HiRAC a number of test cases are considered, in which various different flow phenomena with complex interface motion are simulated. The numerical results are compared quantitatively by means of error estimates as well as by visual comparison of contour plots. As part of the comparative analyses both structured

CHAPTER 5. EVALUATION OF THE SURFACE CAPTURING FORMULATION

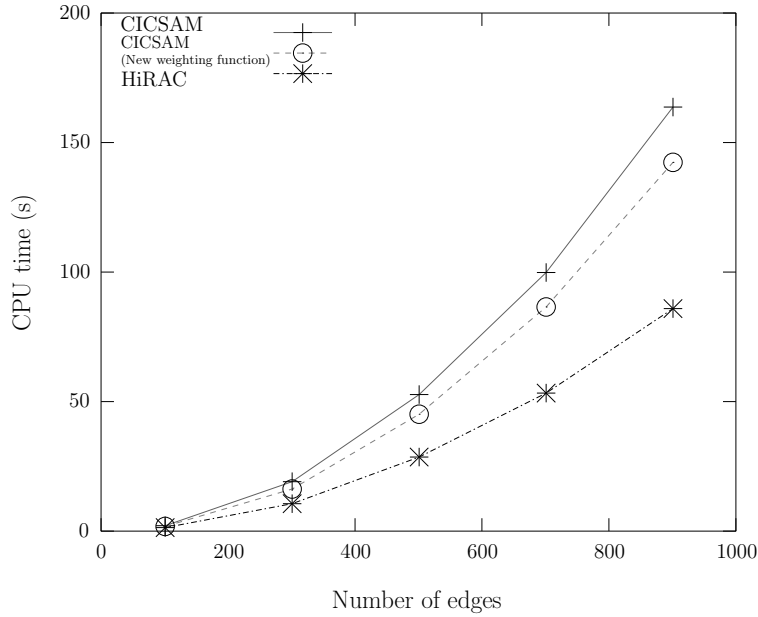


Figure 5.1: CPU time for one-dimensional advection of a step function using CICSAM and HiRAC

as well as unstructured meshes are used. For the evaluation the following test cases are considered

- Advection of a round and a square droplet;
- Rotating key;
- Droplet in shear flow;
- Falling droplet; and
- Three-dimensional sphere undergoing rotation and translation

The criterion most commonly used to evaluate surface capturing schemes is a comparative error analysis (Cassidy *et al.*, 2009; Gopala and van Wachem, 2008; Ubbink and Issa, 1999). For the comparative analysis the numerical results are compared with the expected analytical solution to determine the average error computed as

$$E_{comp} = \frac{1}{N} \sum_{i=1}^N |\alpha_{analt} - \alpha_i| \quad (5.1)$$

which provides an indication of the degree of interface deformation and smearing.

For test cases where the analytical solution is unknown, it is proposed that the following error formulation be used to evaluate the numerical smearing of the interface

$$E_{diff} = \frac{4}{N} \sum_{i=1}^N |\alpha_i| |1 - \alpha_i| \quad (5.2)$$

CHAPTER 5. EVALUATION OF THE SURFACE CAPTURING FORMULATION

where E_{diff} is equal to zero if there are no partially filled cells. As smearing of the interface causes the inaccurate distribution of partially filled cells over the computational domain, the diffusive error E_{diff} provides a way of quantifying the diffusivity of the surface capturing scheme.

Advected square and round droplet

Comparing surface capturing schemes, various authors (Gopala and van Wachem, 2008; Hoekstra *et al.*, 2007; Ubbink, 1997) considered the convection of different forms of droplets through space. In this study the advection of a 30 mm by 30 mm square droplet (Figure 5.2) and a 30 mm diameter round droplet are considered. The droplets are advected at a rate of (0.15, 0.075) mm/s, where the initial centre point is at (20, 20) mm and the final centre point is at (80, 50) mm.

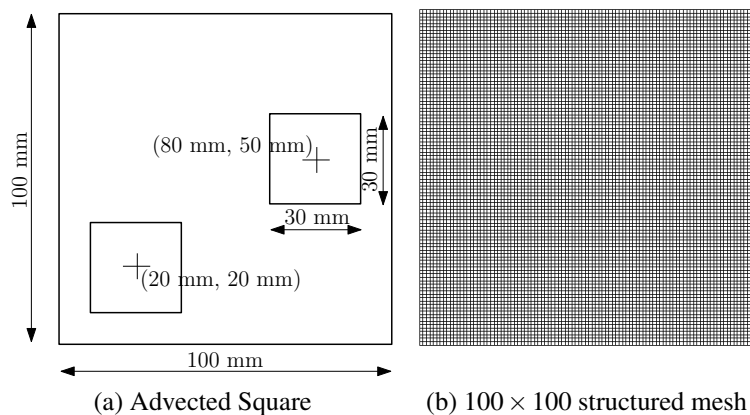
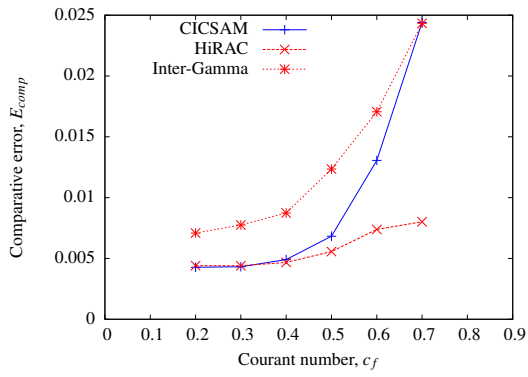


Figure 5.2: Schematic representation of the advected square and round droplet

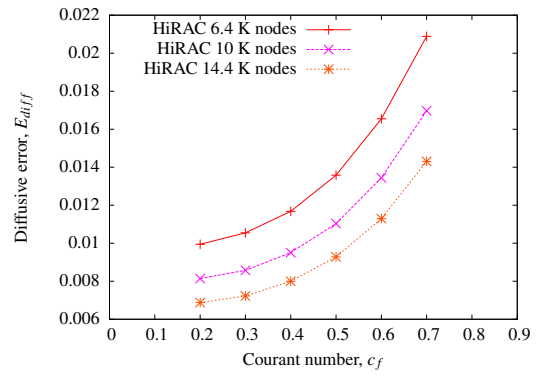
In Figure 5.3a and 5.3c the numerical results of HiRAC are compared with those of CICSAM and Inter-Gamma. For this analysis a 100×100 structured mesh is used. From the comparative error analyses, it is seen that HiRAC provides a notable improvement over the other schemes, with the exception of the results at the lowest Courant numbers which is in agreement with CICSAM. In Figure 5.3b and 5.3d the diffusive errors for the two droplets are shown and evaluated for three different structured meshes (80×80 ; 100×100 ; and 120×120). It is noted that the diffusive errors reduce as the meshes are refined, with the relative proportional gain remaining more or less the same for the different Courant numbers.

Contour plots of the square and the round droplets are respectively shown in Figure 5.4 and 5.5 for a Courant number of 0.6. The contour plots show that for CICSAM the interface is smeared, whereas with Inter-Gamma the shape of the interface is wrinkled or distorted. Building on these schemes and combining their respective qualities, HiRAC maintains a sharp interface and preserves the integrity

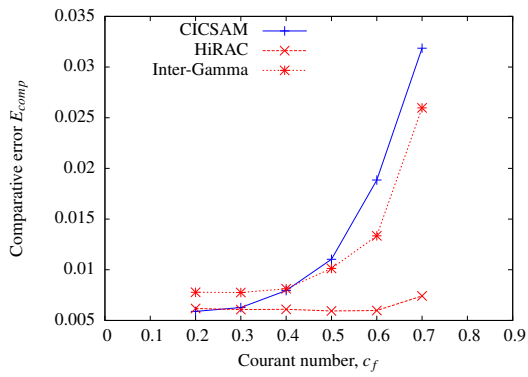
CHAPTER 5. EVALUATION OF THE SURFACE CAPTURING FORMULATION



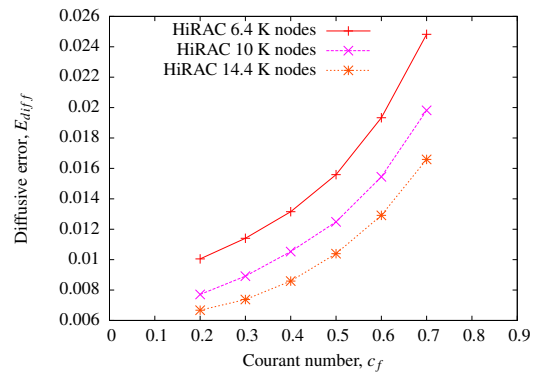
(a) Comparative error for the square droplet



(b) Diffusive error for the square droplet

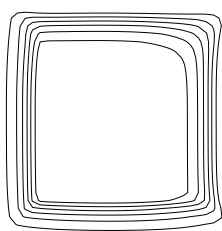


(c) Comparative error for the round droplet

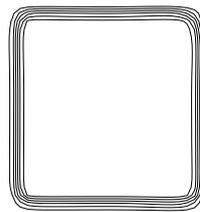


(d) Diffusive error for the round droplet

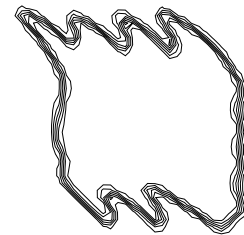
Figure 5.3: Error plots of the advected square and round droplet



(a) CICSAM



(b) HiRAC

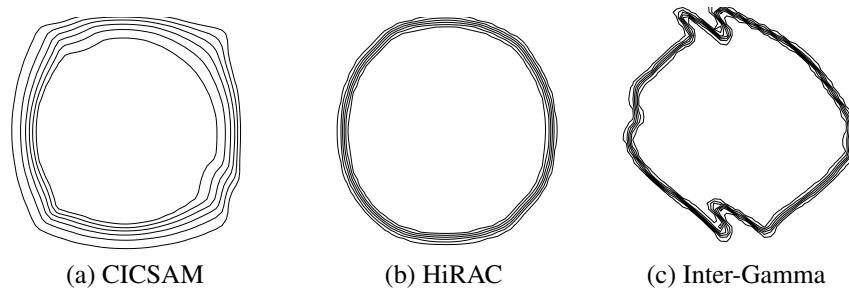


(c) Inter-Gamma

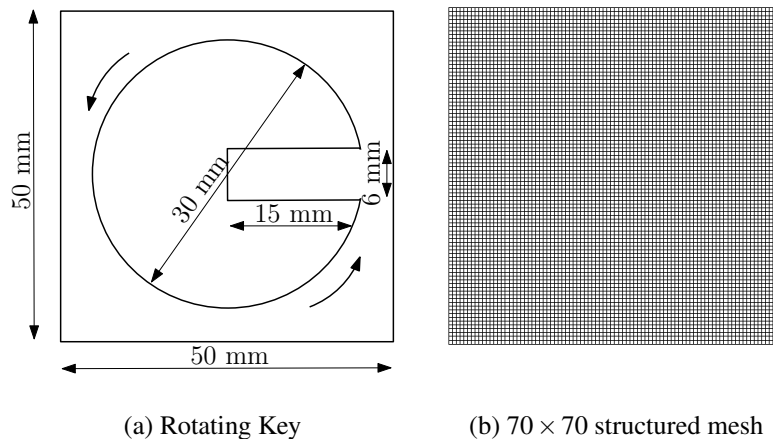
Figure 5.4: Contour plots of the convected square droplet, $c_f = 0.6$

of the interface shape. For the the rest of the analyses HiRAC will be evaluated using CICSAM as a point of reference.

CHAPTER 5. EVALUATION OF THE SURFACE CAPTURING FORMULATION

Figure 5.5: Contour plots of the convected round droplet, $c_f = 0.6$ **Rotating key**

The rotating key test case was used by various authors including Gopala and van Wachem (2008), Waławczyk and Koronowicz (2006), Darwish and Moukalled (2006), Ubbink (1997) and Zalesak (1979) to evaluate different surface capturing schemes. In Figure 5.6 dimensions of the rotating key, a slotted circle that is rotated around its centre, are shown. The diameter of the key is 30 mm and the slot in the sphere is 15 mm long and 6 mm wide. A unidirectional velocity field is applied where $u = -\pi/2(y - y_0)$ and $v = \pi/2(x - x_0)$ and the rotating key centre is $(x_0, y_0) = (25, 25)$ mm. For this analysis a structured mesh is used to represent the 50 mm by 50 mm computational domain.

Figure 5.6: Schematic representation of the rotating key and the 70×70 structured mesh used for the analysis

After one rotation the numerical results are evaluated and compared with the analytical solution. In Figure 5.7 the comparative error as a function of the Courant number is plotted for three different structured meshes (50×50 ; 70×70 ; and 90×90). As with the previous test case, it is shown that HiRAC is to a considerably

CHAPTER 5. EVALUATION OF THE SURFACE CAPTURING FORMULATION

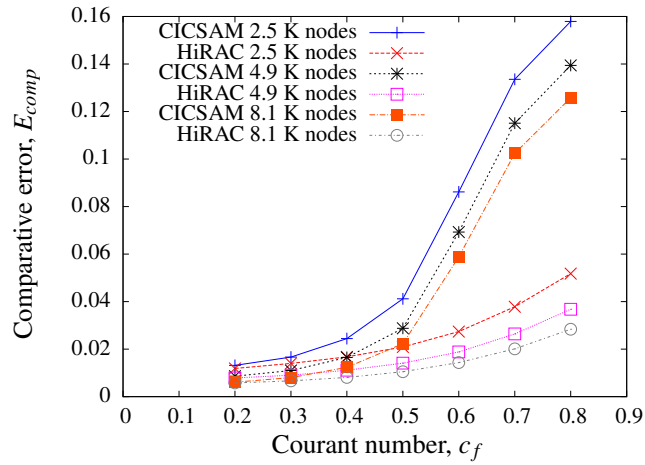
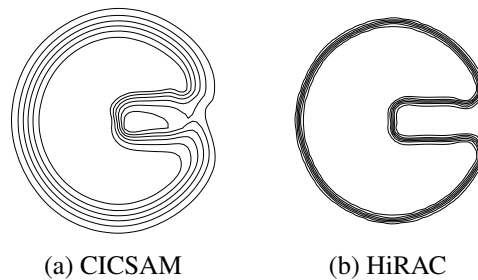


Figure 5.7: Comparative error plot for the rotating key

smaller degree dependent on the Courant number. Furthermore, as the meshes are refined the comparative error for both schemes reduces.

Contour plots of the solution after one rotation for both CICSAM and HiRAC are shown in Figure 5.8. Here again it is found that HiRAC ensures a sharper interface, while maintaining an accurate representation the interface shape.

Figure 5.8: Contour plots of the rotating key, $c_f = 0.6$

Round droplet in shear flow

Gopala and van Wachem (2008) and Hogg *et al.* (2006) evaluated the integrity of surface capturing schemes by considering a two-dimensional droplet placed in a shear flow field. With this test case the ability of the scheme to handle shearing and stretching of the interface is evaluated. A droplet is placed off centre in a rotating flow field as shown in Figure 5.9. The prescribed velocity field is $u = \sin(\pi(x - x_0)) \cos(\pi(y - y_0))$ and $v = -\cos(\pi(x - x_0)) \sin(\pi(y - y_0))$ where the domain centre is $(x_0, y_0) = (50, 50)$ mm. After one rotation the flow field is reversed with the aim

CHAPTER 5. EVALUATION OF THE SURFACE CAPTURING FORMULATION

of recovering the original round droplet. For this analysis an unstructured triangular mesh with 5000 nodes is used to represent the computational domain.

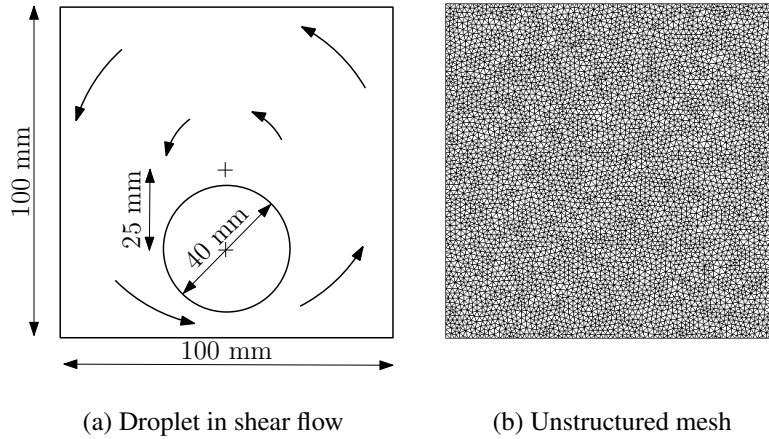


Figure 5.9: Schematic representation of the droplet in shear flow and the unstructured mesh used for the analysis

The schemes are evaluated based on their capability to reproduce the original droplet. In Figure 5.10 the comparative error is plotted as a function of the Courant number. For the droplet in shear flow on an unstructured mesh, it is also found that comparative error for HiRAC is only to a relatively small degree dependant on the Courant number.

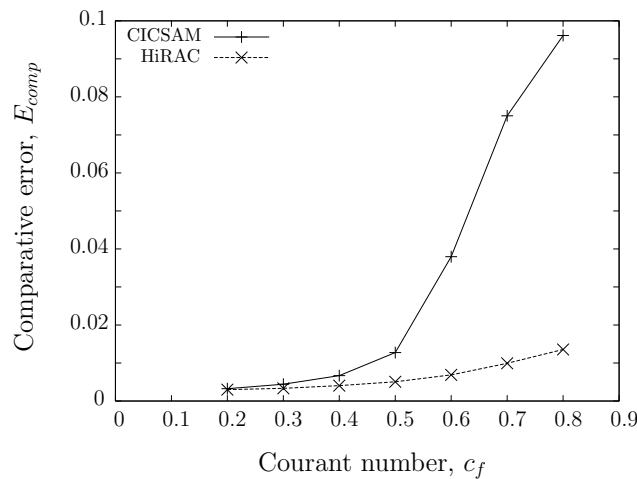


Figure 5.10: Comparative error plot for the droplet in shear flow

Contour plots of the droplet in shear flow are shown in Figure 5.11 and 5.12. In Figure 5.11 the droplet is shown after it has completed one rotation and just before

CHAPTER 5. EVALUATION OF THE SURFACE CAPTURING FORMULATION

the flow field is reversed and in Figure 5.12 the recovered droplet is shown. Both HiRAC contour plots show that a somewhat sharper interface is achieved without distorting the interface shape, reproducing the original droplet more accurately.

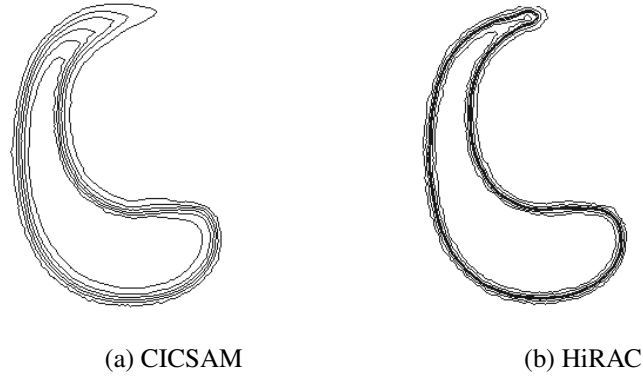


Figure 5.11: Contour plots of the droplet in shear flow just before the flow field is reversed, $c_f = 0.5$

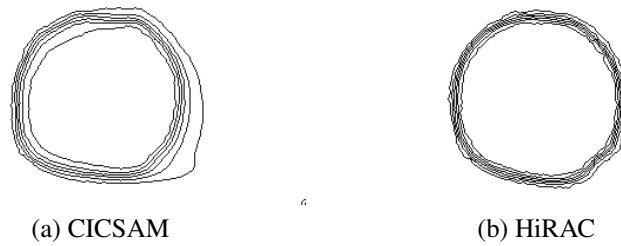


Figure 5.12: Contour plots of the droplet in shear flow after initial shape is recovered, $c_f = 0.5$

Falling droplet

To evaluate the performance characteristics of HiRAC when coupled to an incompressible fluid solver, a falling droplet is modelled. A 50 mm diameter liquid droplet is placed at the centre of a 100 mm by 100 mm computational domain (Figure 5.13) and subjected to a gravitational acceleration of 9.81m/s^2 . The droplet is left to fall and crash at the bottom of the domain, continuing the analysis up to the point where the movement in the liquid has died down sufficiently. For the purpose of this analysis surface tension is neglected, as the aim is to evaluate the numerical smearing inherent to the surface capturing schemes. For this analysis slip boundary conditions are applied and the material properties are given in Table 5.1.

CHAPTER 5. EVALUATION OF THE SURFACE CAPTURING FORMULATION

Table 5.1: Material properties of the falling droplet

	Liquid	Gas
Density (kg/m^3)	998	1.21
Viscosity (kg/ms)	1.002×10^{-3}	1.812×10^{-5}

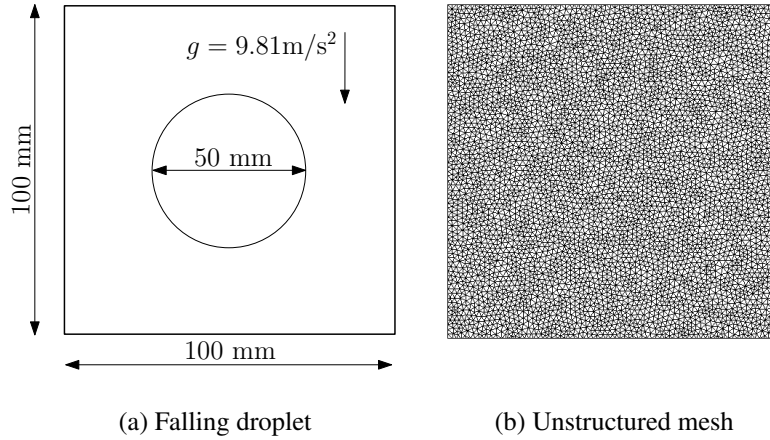


Figure 5.13: Schematic representation of the falling droplet and the unstructured mesh used for the analysis

Over time the diffusive errors for HiRAC and CICSAM are evaluated and compared. In Figure 5.14 the diffusive error for CICSAM and HiRAC are plotted over time.

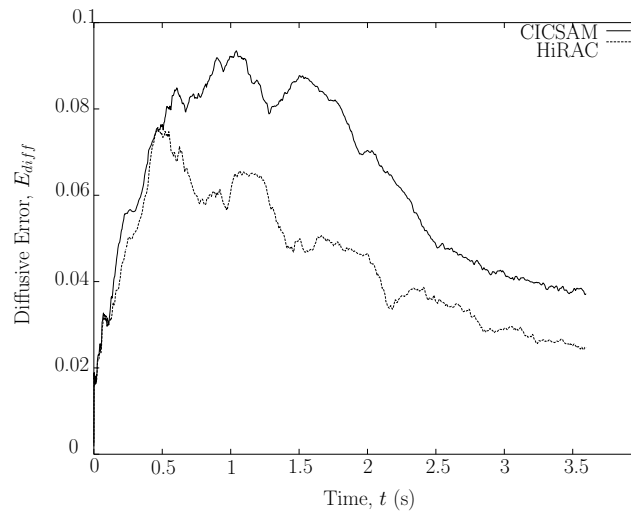


Figure 5.14: Diffusive error as a function of time for the falling droplet

CHAPTER 5. EVALUATION OF THE SURFACE CAPTURING FORMULATION

Snapshots of the falling droplet at different time steps for the two different schemes are shown in Figure 5.15. In the snapshots the high density liquid is coloured blue and the low density gas is green, partially filled cells are shades of white depending on the volume fraction of the cell. For this analysis a c_f number of 0.2 is used.

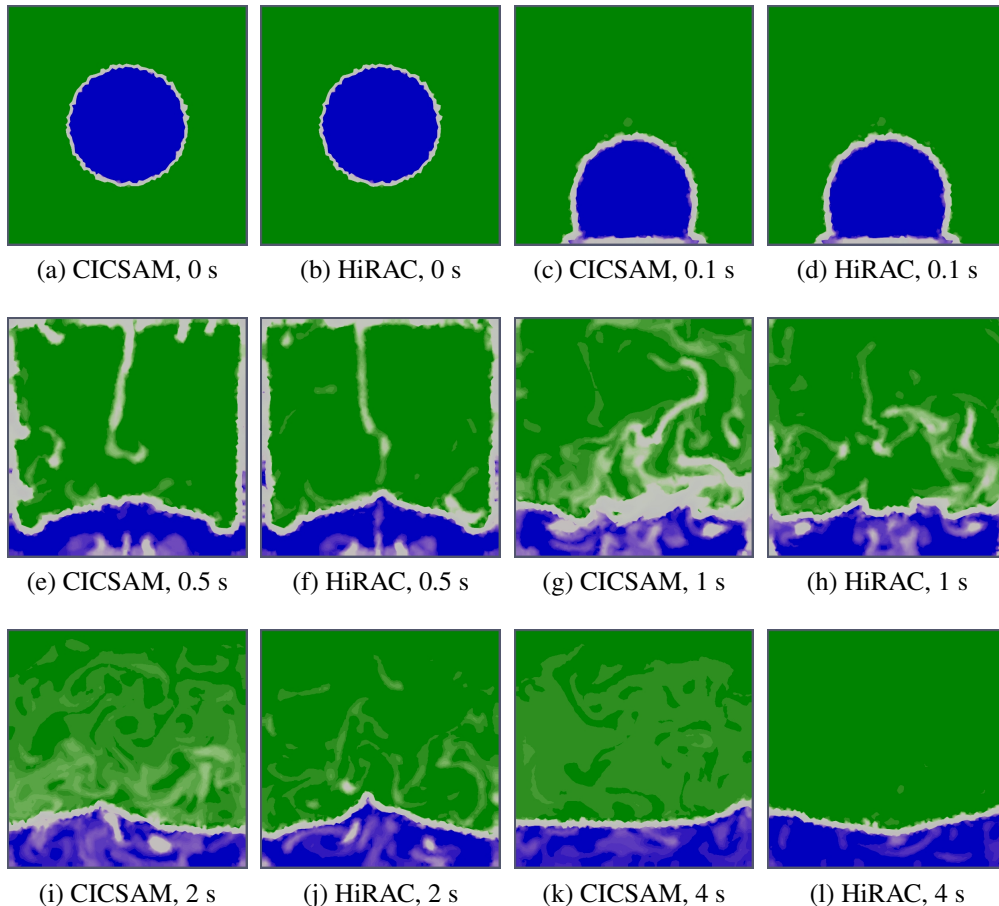


Figure 5.15: Snapshots of the falling droplet

From both the diffusive error plot as well as the snapshots it is noted that initially the numerical smearing is similar for the two schemes, but after 0.5 seconds when the flow becomes more violent it is found that for CICSAM the interface continues to smear. On the other hand with HiRAC it is noted that the amount of smearing is reduced and a much sharper interface is maintained. To the end of the analysis, as the liquid settles down at the bottom of the domain quite a large portion of liquid is still entrapped in the gas when CICSAM is used. When considering the snapshots at 2 s and 4 s it appears as if the solution becomes asymmetric when CICSAM is employed. It is suspected that this disturbance is due to the fact that the partially filled cells induce inaccurate velocity fields within the gas phase. The addition of

CHAPTER 5. EVALUATION OF THE SURFACE CAPTURING FORMULATION

the artificial compressive term helps to recover the interface. This is in contrast to existing higher-resolution interface capturing schemes that are not able to sharpen an interface after it has smeared; the compressive spacial discretisation only aims to limit numerical smearing and maintain the existing gradient.

Three-dimensional unstructured meshes

To demonstrate the extension to three-dimensional unstructured meshes, a slotted sphere that is convected and rotated in space is shown. The slotted sphere is convected in the $x - y$ plane while it is rotated around its x axis. A c_f number of 0.1 is used. In Figure 5.16 the initial contour plot ($\alpha = 0.5$) is shown on the left and the contour plot of the slotted sphere after it is convected through the domain and has done one rotation around the x axis is shown on the right. When comparing the contour plots in Figure 5.16 it is noted that the integrity of the interface shape is well preserved.

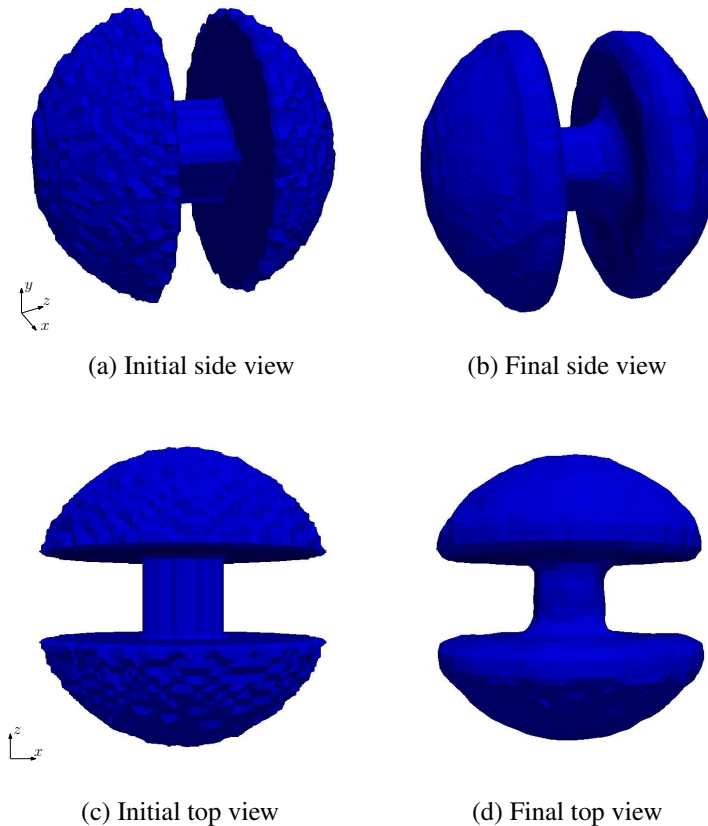


Figure 5.16: Contour plots, $\alpha = 0.5$, of the slotted sphere before and after translation and rotation

5.3 Closer

A new VOF compressive surface capturing formulation for modelling immiscible two-fluid flow was presented. HiRAC combines a computationally efficient blended high resolution scheme, which ensures the shape of the interface is preserved, with an artificial compressive term that increases the sharpness of the interface. It is shown that the new HiRAC formulation is significantly more accurate at higher Courant numbers than existing VOF schemes, being able to ensure a sharper interface. The scheme further proves to be stable and robust; is able to model complex interface phenomena; and is easily extended to three-dimensional unstructured meshes.

Chapter 6

Validation of the weakly compressible formulation

In this chapter, the implementation of the newly derived weakly compressible FSM formulation is verified by considering test cases with known analytical solutions, where after it is evaluated by means of application focused problems. These problems addresses the expansion and compression of the gas in one- and two-dimensions on both structured and unstructured meshes. In the application focused test cases the results of the weakly compressible formulation are compared with the results of an incompressible multi-fluid flow solver. The validation of the weakly compressible formulation with experimental results are presented in Appendix D. The material properties are given in Table 6.1 and a gravitational acceleration of $g = 9.81 \text{ m/s}^2$ are used.

6.1 Forced compression and expansion of the gas

To evaluate the newly proposed weakly compressible formulation, two test cases which model the forced compression and expansion of a gas pocket are presented. The first considers the linear filling of a quasi one-dimensional tube whereby a gas pocket entrapped at the end of the tube is compressed. Whereas, in the second the two-dimensional implementation of the formulation is evaluated by considering the sinusoidal compression and expansion of a gas bubble. For both cases the analytical solution can be obtained by evaluating the mass conservation and noting that liquid

Table 6.1: Material properties of the liquid and gas

	Liquid (Water)	Gas (Air)
Density (kg/m^3)	998	1.21
Viscosity (kg/ms)	1.002×10^{-3}	1.812×10^{-5}
Acoustic velc (m/s)	—	343.2

CHAPTER 6. VALIDATION OF THE WEAKLY COMPRESSIBLE FORMULATION

density remains constant as it is assumed to be incompressible.

Quasi one-dimensional tube

As mentioned, the first test case considers the linear filling of a quasi one-dimensional tube that is sealed off at the end. Liquid enters the tube at a constant velocity and compresses the entrapped gas pocket (Figure 6.1). The velocity of the liquid at the tube inlet is 0.1 m/s and the liquid-gas interface propagates from $x = 0.25$ m to $x = 0.75$ m during the 5 s of the analysis. For the purpose of assessing mesh dependence, three structured meshes are considered with 3×30 nodes, 3×50 nodes, and 3×100 nodes. Slip boundary conditions are specified on the sides of the tube and gravity is neglected.

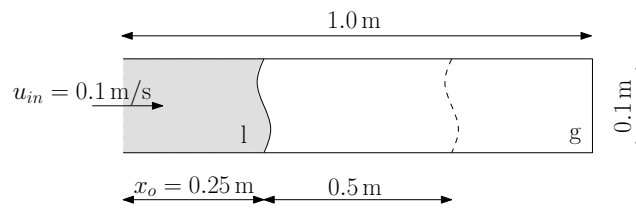
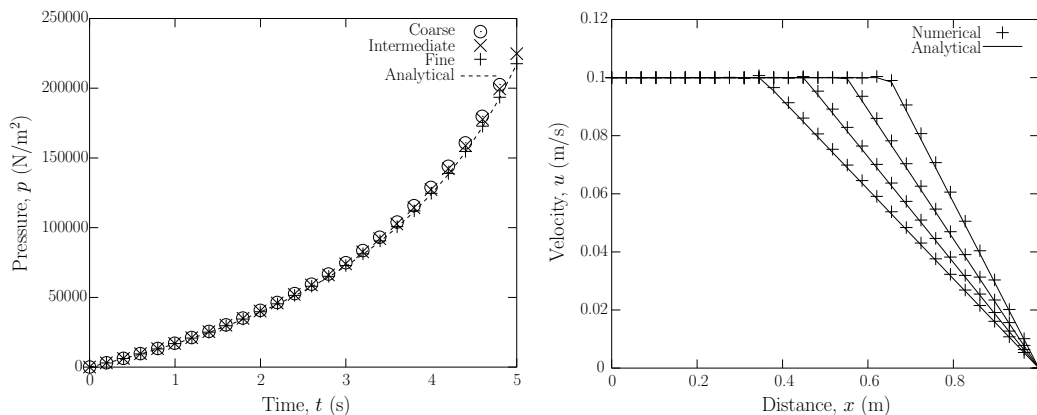


Figure 6.1: Schematic of the quasi one-dimensional tube

In Figure 6.2a the averaged pressure in the gas is shown for the three meshes. The figure shows the non-linear growth in pressure over time and that the numer-



(a) Non-linear increase in the gas pressure over time (b) Velocity profile for the coarse mesh at various time frames

Figure 6.2: Numerical results for the quasi one-dimensional tube

ical results approach the analytical solution as the mesh is refined. In Figure 6.2b the velocity profile for the coarse mesh is shown at various time frames during the

CHAPTER 6. VALIDATION OF THE WEAKLY COMPRESSIBLE FORMULATION

analysis ($t = 1$ s, $t = 2$ s, $t = 3$ s and $t = 4$ s). Even for the coarse mesh a good correlation between the numerical results and analytical solution is found. As expected, the velocity is constant in the incompressible fluid and reduces linearly in the compressible gas. Importantly, it is noted that the predicted solution is free of non-physical oscillations despite the sharp change in the velocity gradient over the free-surface interface.

Gas bubble

To evaluate the two-dimensional implementation, a 0.2 m diameter gas bubble subjected to sinusoidal compression and expansion is considered. The bottom of the domain (see Figure 6.3) is open and the prescribed liquid velocity is

$$u_i = a \sin(2\pi\theta t) \quad (6.1)$$

where the amplitude and frequency are respectively $a = 0.05$ and $\theta = 2$. As with the previous case, gravity is neglected and slip boundary conditions are specified on the sides of the tube.

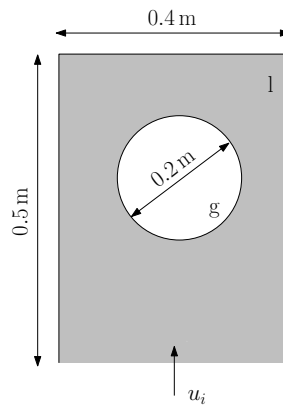


Figure 6.3: Schematic representation of gas bubble subjected to sinusoidal compression and expansion

In Figure 6.1 the average pressure in the gas bubble is shown. Three structured meshes are used with respectively 40×50 nodes, 60×75 nodes, and 80×100 nodes. It is noted that the numerical results of all three meshes very closely approximate the analytical solution, with only a 1.7 % difference at the point of highest compression ($t = 0.25$ s).

6.2 Gravity driven flow

In the next test case the two-dimensional implementation of the compression and expansion of the gas on an unstructured mesh is evaluated as well as the potential

CHAPTER 6. VALIDATION OF THE WEAKLY COMPRESSIBLE FORMULATION

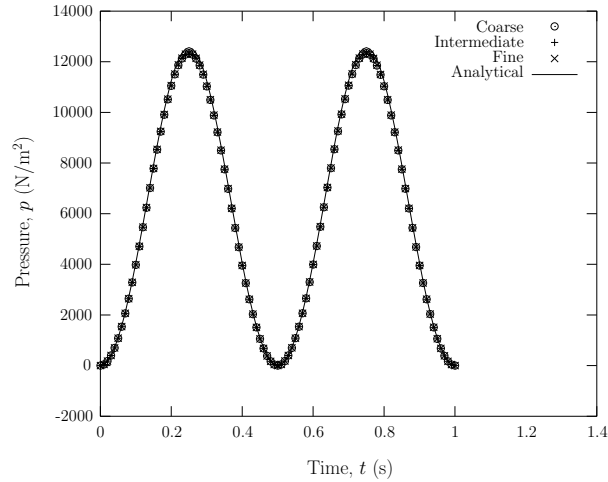


Figure 6.4: Average pressure in the gas bubble during compression and expansion

improvement in computational time if the GMRES solver is employed. Two enclosed columns of liquid, at different fill levels, are connected via a bottom channel allowing flow between them (Figure 6.5). Driven by gravity the liquid flow results

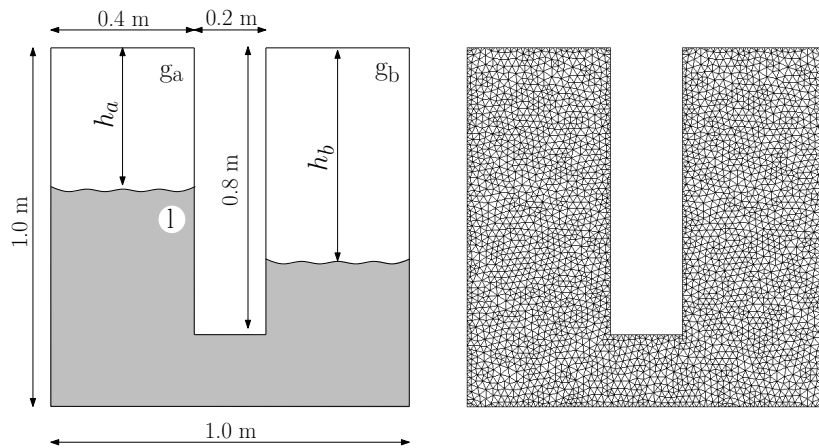


Figure 6.5: Schematic of two columns of water at different fill levels and the unstructured 4000 node mesh

in the oscillatory compression and expansion of the entrapped gas pockets. The initial fill levels are $h_a = 0.4$ and $h_b = 0.6$ and the initial gas density and pressure are respectively set to $\rho_a^0 = \rho_b^0 = 1.2 \text{ kg/s}$ and $p_a^0 = p_b^0 = 0 \text{ N/m}^2$. Viscous boundary conditions were assumed.

The average pressure in the gas pockets over the duration of the analysis is plotted in Figure 6.6. As the oscillations dampen out, due to the viscous and header losses, a steady state solution is approached and can be compared with the analytical

CHAPTER 6. VALIDATION OF THE WEAKLY COMPRESSIBLE FORMULATION

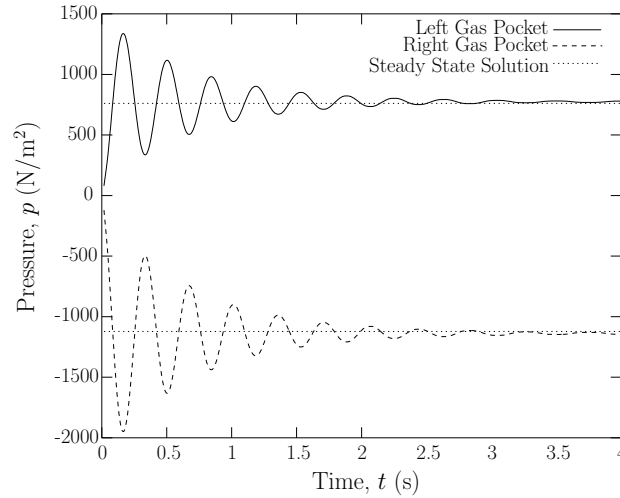


Figure 6.6: Average pressures in the gas pockets

solution. From Figure 6.6 it is noted that the pressure dampens out to within 3 % of the analytical steady state solution.

To illustrate the improvement in computational time if the projected pressure equation is solved using the GMRES solver instead of the Jacobi-type solver, the CPU times for three different unstructured meshes are compared in Table 6.2. These analyses were done using a single core of an Intel i7 2.67 GHz quad-core processor and it is found that a speed up of approximately 70 times can be achieved. For the remainder of the test cases the projected pressure equation is solved using GMRES with LU-SGS preconditioning.

Table 6.2: Comparison of solver times

	4 K	6 K	8 K
Jacobi-type solver	232 min	391 min	596 min
GMRES solver	3.5 min	5.5 min	8 min
Speed-up	66.3	71.1	74.5

6.3 Growth of a rising bubble

The next validation type problem considers the growth of a rising two-dimensional bubble (Figure 6.7) and compares the results with an analytical solution using a static pressure approximation. This approximation assumes that the internal bubble pressure equals the mean static pressure. As the compressibility of a gas bubble rising in liquid is negligible for the scales considered, non-representative material properties are used to illustrate the growth of a compressible bubble. The bubble

CHAPTER 6. VALIDATION OF THE WEAKLY COMPRESSIBLE FORMULATION

density is taken as 100 kg/m^3 , the acoustic velocity as 20 m/s and a surface tension (Appendix C) of 1 N/m is used; the remaining properties remain unchanged. Slip boundary conditions were applied.

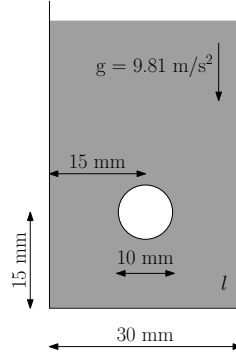


Figure 6.7: Schematic representation of the rising gas bubble

The results were evaluated by comparing the volume of the bubble at different heights, where the mean bubble height is calculated using the following relation

$$h(t) = \frac{\int_{\mathcal{V}} \alpha_g(\mathbf{x}, t) \mathbf{x} \cdot \mathbf{n}_y d\mathcal{V}}{\int_{\mathcal{V}} \alpha_g(\mathbf{x}, t) d\mathcal{V}} \quad (6.2)$$

where α_g is the gas volume fraction and \mathbf{n}_y is the unit vector in the vertical direction.

In Figure 6.8 the numerical results for three different structured meshes with 50×150 nodes, 70×210 nodes, and 90×270 nodes are shown. The numerical results for the weakly compressible formulation are compared with that of the incompressible formulation as well as the analytical solution, assuming a static pressure approximation.

As expected, the incompressible solver predicts the bubble volume remains constant, whereas the weakly compressible formulation approaches the linear analytical solution. The low amplitude oscillations stem from the imperfect initial pressure distribution due to the surface tension, leading to the subsequent compression and expansion of the bubble. From the figure it appears the results provide a reasonable approximation of the expected solution.

6.4 Horizontal shaker

The next test-case involves an application study. For this purpose liquid trapped between two gas pockets in a horizontal tube (Figure 6.9) is subjected to variable lateral excitation. The pocket is placed at the centre of the tube and is evaluated under two different horizontal accelerations. In the first analysis, a smooth sinusoidal

CHAPTER 6. VALIDATION OF THE WEAKLY COMPRESSIBLE FORMULATION

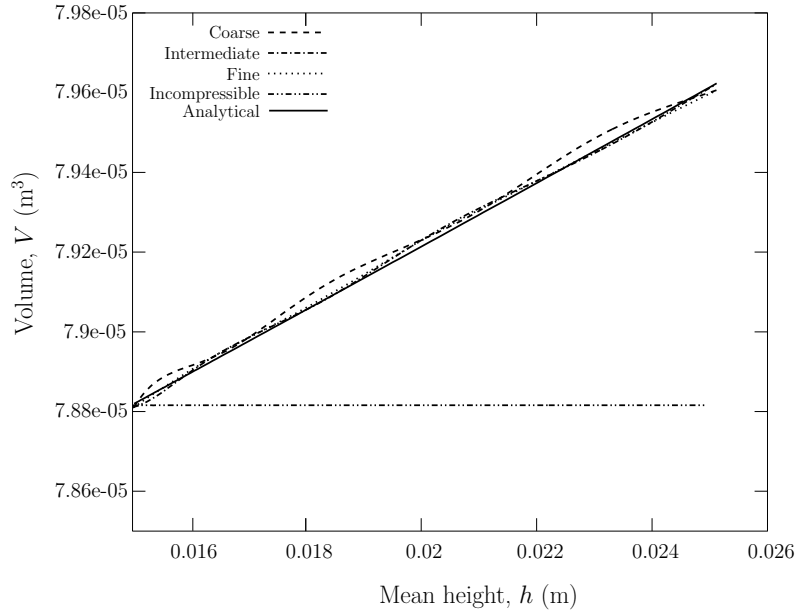


Figure 6.8: Linear growth of the rising bubble

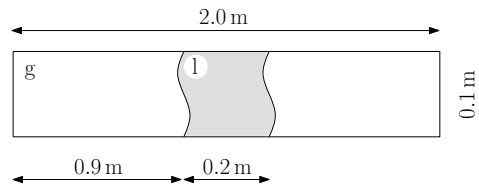


Figure 6.9: Schematic representation of the liquid subjected lateral excitation

acceleration is applied to the tube and, in the second, a step function with a sharp ramp in acceleration is applied. These are expressed as

$$a_x^{\text{sin}} = 10 \sin(2\pi t) \quad (6.3)$$

$$a_x^{\text{step}} = \begin{cases} 0 & \text{if } 0 < t < 0.1 \text{ s} \\ 10 & \text{if } t > 0.1 \text{ s} \end{cases} \quad (6.4)$$

where a_x is the lateral acceleration and t denotes time. For the purpose of this test case gravitational acceleration as well as the liquid and gas viscosity are neglected.

Sinusoidal excitation

In Figure 6.10 the left sidewall pressures are shown, where the numerical results for different acoustic velocities are compared with predicted values from an incompressible model. The incompressible model assumes an infinitely large acoustic velocity and the pressure on the sidewall is approximated as the product of mass times acceleration.

CHAPTER 6. VALIDATION OF THE WEAKLY COMPRESSIBLE FORMULATION

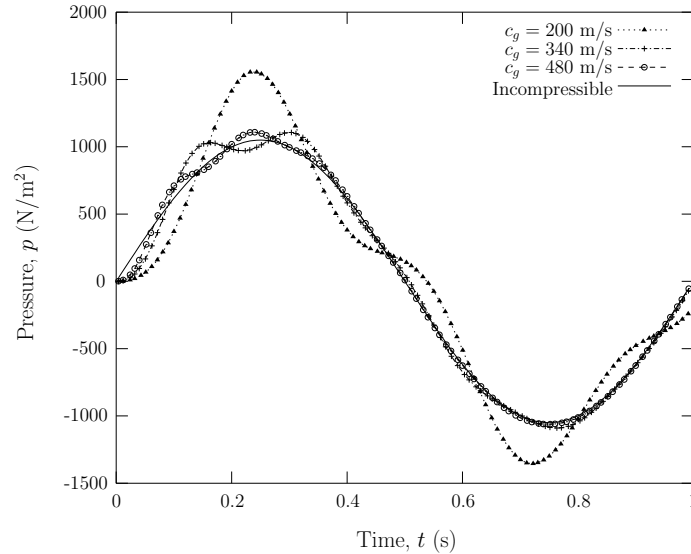


Figure 6.10: Left sidewall pressure for the liquid subjected to sinusoidal excitation

Similar to a spring-mass system, the gas initially absorbs the energy where after it is released, resulting in the oscillatory behaviour seen in the computed pressures. From Figure 6.10 it is noted that as the acoustic velocity increases the numerical results approach the incompressible limit. It is found that for the gradual sinusoidal excitation the effect of the compressibility is less pronounced and the computed maximum pressure is of the same order as the pressure predicted by the incompressible approximation. Only for the most compressible gas ($c = 200$ m/s) a notable difference is noted.

Step function excitation

In Figure 6.11 the left sidewall pressures for different meshes are compared with the analytical solution as well as the incompressible model described previously. The analytical solution is obtained by evaluating the forces acting on the liquid pocket, which includes the pressures at the liquid-gas interfaces and the acceleration of the liquid mass. For this analysis the specified acoustic velocity of 343.2 m/s is used. The mesh is refined in the surroundings of the free-surface interface, where horizontal spatial resolutions of respectively 0.01 m, 0.005 m and 0.0025 m are used.

From Figure 6.11 it is noted that with the sharp ramp in the acceleration, the compressibility of the gas greatly influences the pressure measured on the sidewall. The maximum pressure is a factor 2 larger than the pressure predicted by the incompressible model. From the figure it is further noted that as the mesh is refined the numerical results approach the analytical predicted amplitude and frequency. For the coarse mesh where the degree of interface smearing is relatively large compared to the amount of interface movement, it is found that the numerical dissipation

CHAPTER 6. VALIDATION OF THE WEAKLY COMPRESSIBLE FORMULATION

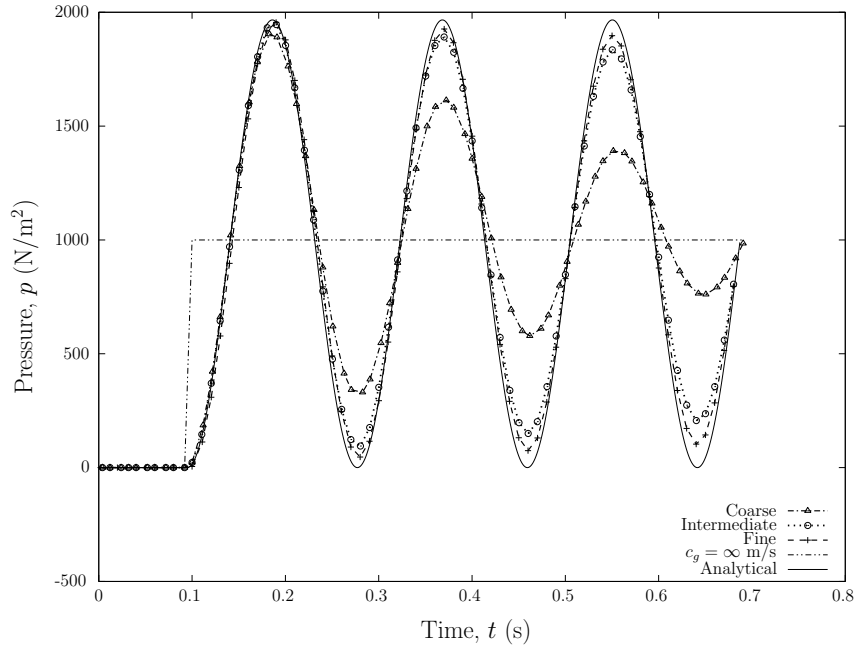


Figure 6.11: Left sidewall pressure for the liquid subjected to a step function excitation

quickly dampens out the pressure oscillations, deteriorating the solution accuracy.

For large systems it is not always practical to refine the mesh to the degree stated above, suggesting that these problems will be subjected to poor numerical accuracy. It is, however, noted that for sloshing type analyses maximum load pressures and load frequencies are typically of importance and from Figure 6.11 it is noted that even with the intermediate mesh, acceptable levels of accuracy are obtained during the first oscillation. It is, therefore, suggested that despite these restrictions the weakly compressible FSM formulation provides a measurable improvement in the pressure prediction of liquid-gas systems subjected to irregular accelerations.

6.5 Sloshing analysis of a partially filled tank

Finally, the weakly compressible formulation is evaluated by means of a comparative analysis, where a partially filled tank with a baffle configuration under lateral excitation is considered. The tank, shown in Figure 6.12a, is 70 % filled with liquid and is subjected to lateral sinusoidal excitation with an amplitude of 8 m/s^2 and a frequency of 2 Hz. For this analysis a structured mesh with 5000 nodes is used (see Figure 6.12b); the pseudo time-step is computed using a CFL number of 0.1 and for the VOF equation the real time step is restricted to a similar Courant number. No slip boundary conditions were applied to the tanks walls.

The weakly compressible and incompressible formulations are compared by evaluating the predicted average sidewall pressures, where the averaged pressures

CHAPTER 6. VALIDATION OF THE WEAKLY COMPRESSIBLE FORMULATION

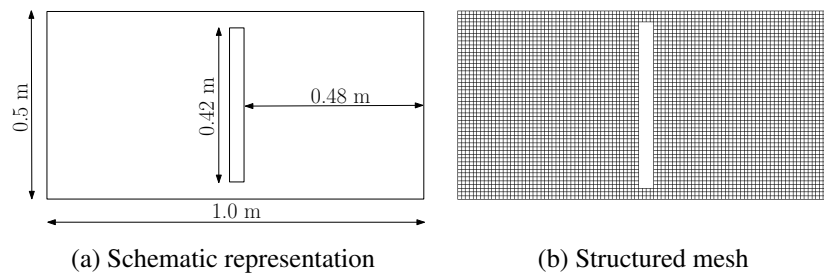


Figure 6.12: Partially filled tank with baffle configuration

are computed by integrating the pressure over the sidewall. As only the pressure gradients are computed for incompressible flow and not absolute pressures, the difference in average pressures is evaluated. In Figure 6.13 the difference in left and right sidewall average pressure is shown and in Figure 6.14 the difference in the average pressure for the left and right side of the baffle is shown.

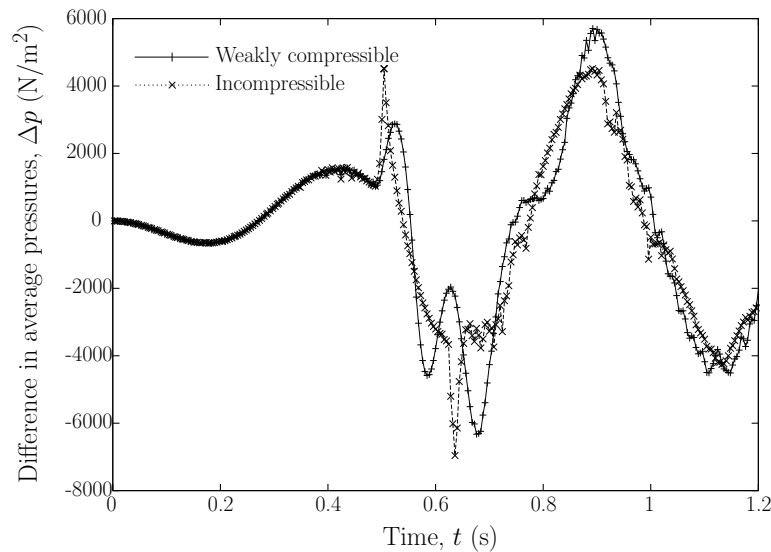


Figure 6.13: Difference in average pressure measured on the left and right sidewall

A notable difference between the weakly compressible and incompressible formulations are the sharp spikes in pressure at $t = 0.5$ s and $t = 0.62$ s, which correspond to the times that the top baffle opening is covered by liquid (see Figure 6.15). As the incompressible formulation do not account for the compressibility of the gas, it results in sharp spikes in the predicted pressures. Whereas, for the weakly compressible formulation the maximum pressure calculated at these points is slightly less, but as expected, the pressure oscillates as the gas stores and releases energy. Considering the pressures measured on the baffle, it appears the weakly compressible formulation predicts larger variations in the minimum and maximum forces

CHAPTER 6. VALIDATION OF THE WEAKLY COMPRESSIBLE FORMULATION

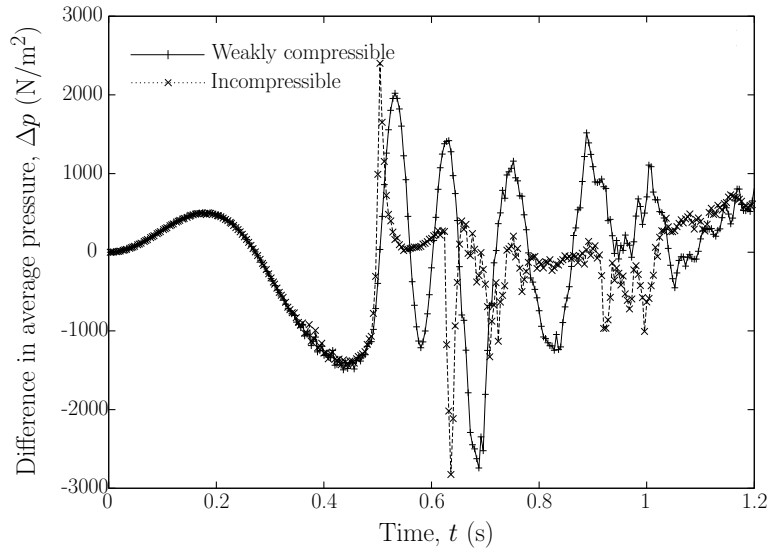


Figure 6.14: Difference in average pressure measured the left and right side of the baffle

translated to the side walls as well as an increase in the frequency of the predicted pressures.

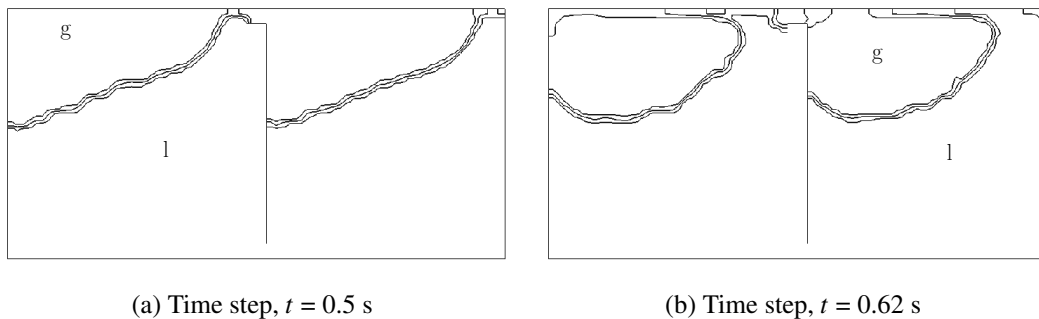


Figure 6.15: Contour plots ($\alpha = 0.1$, $\alpha = 0.5$ and $\alpha = 0.9$) for the weakly compressible formulation during the time frames of maximum impact pressure

The numerical results indicate similar trends as reported in experimental studies of Faltinsen *et al.* (2005), Lugni *et al.* (2006) and Bullock *et al.* (2007). They found that the presence of the compressible air reduces the peak pressure levels, but increases the duration of the impact. In the experimental validation of the weakly compressible solver, presented in Appendix D, it is noted that oscillatory behaviour noted in the experimental measured pressures are fairly accurately represented in the predicted numerical results. For the weakly compressible formulation it is noted that there is a slight improvement in the computational time. As the latter takes into

CHAPTER 6. VALIDATION OF THE WEAKLY COMPRESSIBLE FORMULATION

account the compressibility of the gas, it is suspected that the scheme softens the numerical system leading to a quicker convergence of the solution.

6.6 Closer

In this section the new weakly compressible formulation was validated, demonstrating its ability to accurately simulate the compression and expansion of the gas on two-dimensional structured and unstructured meshes. It was also found that through the implementation of an iterative implicit GMRES solver a CPU speed-up of approximately 70 times can be realised. The influence of the compressibility of the gas was further demonstrated in application type problems in which the computed results for the weakly compressible formulation were compared with that of an incompressible formulation. It was found that the compressible gas has a pronounced effect on pressure predictions for sharp or violent acceleration of a high density ratio two-fluid system. Furthermore, in sloshing analyses the presence of the compressible gas may reduce the peak pressure measured, but results in pressure oscillations which are translated onto the container walls, increasing the frequency of loads experienced by the structure.

Chapter 7

Conclusions and future work

Conclusions

Computational fluid dynamics has developed to a point where it can provide a cost effective alternative for analysing two-fluid flow. With the aim of improving the accuracy of free-surface modelling, this study considered the extension of the volume-of-fluid method in two ways. First, the flow solver was extended to account for changes in the gas density of liquid-gas systems by means of a novel weakly compressible two-fluid flow formulation. The second entailed the development of a new compressive surface capturing scheme that provides a more accurate representation of the free-surface interface evolution.

To improve existing incompressible FSM solvers, the weakly compressible two-fluid flow formulation accounts for the compressibility of the gas. Considering liquid-gas systems under low Mach number flow conditions, a non-dimensional analysis shows the high density liquid may be treated as incompressible and the gas represented using a weakly compressible approximation. With the weakly compressible formulation variations in gas density is modelled in a computationally efficient manner, which allows for the simulation of industrial sized problems over an extended period of time.

The new weakly compressible formulation was successfully implemented in a parallel flow solver, which uses a vertex-centred edge-based approach and allows for the application to unstructured multi-dimensional meshes. In the process of validating the new formulation it was shown that the compression and expansion of the gas can be modelled accurately. The spatial interpolation is done in a consistent manner that ensures a conservative solution free from spurious oscillations. Furthermore, the governing equations are solved in a fully coupled manner using a combination of a Jacobian-type solver with dual time-stepping and an advanced GMRES solver with LU-SGS preconditioning to allow for efficient solution convergence.

In the application of the weakly compressible formulation it was shown that the gas compressibility may influence the predicted pressure loads, especially under

CHAPTER 7. CONCLUSIONS AND FUTURE WORK

flow conditions with sharp or violent excitations. In a comparative two-dimensional sloshing analysis, it was shown that the compressible gas reduces the peak pressure levels, but increases the duration of the impact. Furthermore, the presence of the compressible gas results in pressure oscillations which are translated onto the container walls, increasing the frequency of pressure loads experienced by the structure. This appears to be in agreement with reported experimental findings and demonstrates the need to account for the compressibility of the gas in numerical sloshing analyses.

In the second part of this work a new Higher-Resolution Artificial Compressive (HiRAC) surface capturing formulation was developed. Through the novel combination of a higher-resolution scheme and the addition of an artificial compressive term a more accurate representation of the free-surface interface evolution is achieved. Furthermore, to improve the computational efficiency of the higher-resolution scheme the normalised variable approach used to interpolate the volume fraction face value was reformulated and a new higher-resolution blending function was proposed. The VOF equation is solved in a fully coupled manner using a Jacobian-type dual time-stepping approach with second order Crank-Nicolson. This allows for the availability criteria to be satisfied at every time step and as the solution converges in pseudo-time it approaches an implicit solution.

HiRAC was evaluated by comparing it to the blended higher-resolution scheme, CICSAM, and the Inter-Gamma scheme, which employs the artificial compressive term. In various comparative analyses reported in literature it was noted that CICSAM provides an accurate approximation of the free-surface interface evolution and is therefore often used as a benchmark. It was shown in the evaluation of HiRAC that the combination of the higher-resolution scheme and the addition of the artificial compressive term ensures a much sharper interface, especially for larger Courant numbers, while preserving the integrity of the interface shape. By reducing the numerical diffusivity, HiRAC provides a positive improvement in accuracy when modelling the evolution of the free-surface interface on unstructured, multi-dimensional meshes. The reformulated higher-resolution scheme and newly proposed blending function appears to provide some improvement in computational efficiency.

In conclusion this work advances on existing free-surface modelling formulations through the extension of a new weakly compressible two-fluid flow formulation and the development of a new compressive surface capturing formulation. These advances enable a more accurate numerical representation of liquid-gas flow dynamics.

Future work

Currently, the weakly compressible formulation assumes barotropic expansion of the gas where the density is only a function of pressure. A more accurate approximation would be to extend the formulation to isentropic compression and expan-

CHAPTER 7. CONCLUSIONS AND FUTURE WORK

sion of the gas. This would, however, require the inclusion of an energy equation to account for variations in temperature and subsequently in the acoustic velocity. Due to the strong interdependence of the pressure and acoustic velocity and the sharp changes in gradients over the free-surface interface, the coupling of the energy equation to the continuity and momentum equations would require special attention. It is recommended that the improvement in the fidelity of the formulation along with the possible reduction in computational efficiency be evaluated.

In the existing formulation the use of the Jacobi-type dual time-stepping approach allows for a fully coupled solution, which is expected to improve the accuracy. Even when the the projected pressure equation is solved using GMRES, it is found that for relatively large sloshing analyses the solution is slow to converge. For these analyses it seemingly becomes necessary to employ small CFL numbers to ensure the solution residuals reduce to below the required tolerance. Due to the very sharp change in gradients over the free-surface interface, it is suspected that the strong coupling of the governing equations are not ideal. With the aim of improving the computational efficiency, it is suggested that a weaker coupling of the governing equations with substepping be evaluated to see whether the required accuracy can still be achieved. Furthermore, the weakly compressible formulation is extended to three-dimensional analysis, however, due to this restriction on the CFL number large scale analyses appear not to be viable. From preliminary investigations it is found that a weakly coupled explicit split formulation provides a measurable improvement in computational efficiency.

Despite using a dual time-stepping approach which converges to an implicit solution when solving the VOF equation, it is found that the implementation of the implicit CBC formulation results in an unbounded solution. It is, therefore, still necessary to employ the more diffusive explicit form of CBC. This needs to be investigated along with the method in which the cell Courant number for CBC is calculated for multi-dimensional analyses. CBC for the normalised variable approach is derived from first principles for a one-dimensional finite difference mesh and although various approaches have been presented for the extension to multi-dimensional unstructured meshes it is believed that a more fundamental understanding is required.

Most higher-resolution schemes employ the normalised variable approach with CBC, however slope limiting functions with total variation diminishing (TVD) are successfully employed in compressible flow to describe sharp changes in gradients. It is suggested that these approaches along with their boundedness criteria should be evaluated and compared for use in higher-resolution schemes when modelling multi-fluid flow. The study should consider the applicability for implementation on multi-dimensional unstructured meshes as well as their sensitivity to the Courant number for both explicit and implicit temporal discretisation.

Appendix A

Temporal discretisation

The general form of the governing equations, written for each control volume, can be expressed as a system of coupled differential equations in time

$$\frac{\partial \mathbf{W}}{\partial t} = \mathbf{r} \quad (\text{A.1})$$

where \mathbf{r} denotes the right-hand side of the governing equations. The temporal discretisation of this system can be divided into two main classes, namely explicit and implicit schemes.

A.1 Explicit temporal discretisation

With explicit schemes the temporal derivative is approximated by a forward difference, where the right-hand side is evaluated at the current time step, n ,

$$\mathbf{W}^{n+1} - \mathbf{W}^n = \Delta t \mathbf{r}(t^n, \mathbf{W}^n) \quad (\text{A.2})$$

which is also referred to as a single-stage scheme, as the solution for \mathbf{W} is found from evaluating \mathbf{r} only once.

To extend the order of the explicit scheme's accuracy to higher than one, multistage time-stepping methods such as Runge-Kutta (RK) can be employed. Löhner (2001) gives a general formulation for RK

$$\mathbf{W}^{n+1} - \mathbf{W}^n = \Delta t b_i \mathbf{r}^i \quad (\text{A.3})$$

$$\mathbf{r}^i = \mathbf{r}(t^n + c_i \Delta t, \mathbf{W}^n + \Delta t a_{ij} \mathbf{r}^j) \quad (\text{A.4})$$

where $i = 1, s$; $j = 1, i - 1$; and s is the number of stages. The coefficients a_{ij} and b_j , used to weight the right-hand side at each stage, can be optimised for extended regions of stability or induce the preferred damping properties. For a more detailed discussion on multistage explicit time-steppings methods the reader is referred to Löhner (2001), Blazek (2001) and Wesseling (2001).

Löhner (2001) and Blazek (2001) list the following properties inherent to explicit schemes:

APPENDIX A. TEMPORAL DISCRETISATION

- Achieve arbitrary order of temporal accuracy;
- Easy to implement;
- Numerical efficiency and have a low memory usage;
- Simple to enforce boundary conditions;
- Extension for parallel computing is straight forward; however,
- The allowable time step size is restricted by the stability constraint or CFL number.

This restriction in stability may result in increased solution times in cases where the mesh is highly distorted or where the system of equations are stiff. In these cases it may be beneficial to consider alternative methods of temporal discretisation.

Stability constraint

For a stable explicit solution, the time step size is restricted by the Courant-Friedrichs-Lewy (CFL) number, which for a hyperbolic system of partial differential equations (PDEs) is given by the following relation

$$\Delta t = \frac{CFL \Delta \chi}{\lambda} \quad (\text{A.5})$$

where a stable solution is found for a CFL number of unity or smaller. Further, λ refers to the eigenvalues associated with the PDE and $\Delta \chi$ refers to the length scale (Malan, 2002)

$$\Delta \chi = \sqrt{\Delta x_i \Delta x_i} \quad (\text{A.6})$$

For coupled continuity and momentum equations the maximum eigenvalue can be calculated using the following expression (Malan, 2002):

$$\lambda = \frac{1}{2} \left(|u| + \sqrt{|u||u| + 4c^2} \right) \quad (\text{A.7})$$

where $|u|$ is the magnitude of the local velocity and c is the acoustic velocity.

Dual time-stepping

One of the methods used to accelerate convergence rates when solving steady state problems, is through local time stepping. This entails advancing the solution in each control volume with the maximum permissible time step. Shuen *et al.* (1993) extended the idea of local time-stepping to transient problems. This involves the

APPENDIX A. TEMPORAL DISCRETISATION

formulation of a Jacobian-type dual time-stepping method, which is solved iteratively in pseudo-time for every real or physical time step

$$\frac{\mathbf{W}^{\tau+1} - \mathbf{W}^{\tau}}{\Delta t_{\tau}} = \mathbf{r}(t^{\tau}, \mathbf{W}^{\tau}) - \frac{\mathbf{W}^{\tau} - \mathbf{W}^n}{\Delta t} \quad (\text{A.8})$$

where the temporal term is added as a source term on the right-hand side. As the solution converges in pseudo-time the pseudo temporal term on the left-hand side tends to zero and the system approaches an implicit solution.

Although the pseudo time step size, Δt_{τ} , is still restricted by the CFL stability criteria, it can be computed locally to enhance convergence by advancing the solution locally with the largest allowable pseudo time-step. The local time-stepping does not influence the real-time temporal accuracy and no restriction is placed on the real time step. It can, therefore, be chosen to be of the same order as the physical time scale.

A.2 Implicit temporal discretisation

If the time scales permitted by the stability criteria for explicit schemes are much smaller than the time scales governing the accuracy of the solution, it is found that the efficiency may be improved by employing a computationally more expensive temporal discretisation method that provides better stability. This can be achieved through an implicit temporal discretisation of the PDEs, where the right-hand side is evaluated at time step $n + \theta$

$$\mathbf{W}^{n+1} - \mathbf{W}^n = \Delta t \mathbf{r}(t^{n+\theta}, \mathbf{W}^{n+\theta}) \quad (\text{A.9})$$

where $0 < \theta \leq 1$. The system reduces to first order backward difference for $\theta = 1$ and to second order Crank-Nicholson for $\theta = 0.5$.

With the goal of reducing the memory usage, the right-hand side is most often linearised about the current time step (Löhner, 2001; Blazek, 2001)

$$\mathbf{r}^{n+\theta} = \mathbf{r}^n + \left. \frac{\partial \mathbf{r}}{\partial \mathbf{W}} \right|^n \cdot \theta \Delta \mathbf{W} = \mathbf{r}^n + \mathbf{C}^n \cdot \theta \Delta \mathbf{W} \quad (\text{A.10})$$

so that Equation (A.9) can be expressed in terms of a flux Jacobian \mathbf{C}^n

$$[1 - \Delta t \theta \mathbf{C}^n] \cdot \Delta \mathbf{W} = \mathbf{r}^n \quad (\text{A.11})$$

For implicit schemes Löhner (2001) and Blazek (2001) lists the following properties

- Large time steps are allowed as it is only governed by accuracy and not by stability;
- Better robustness and faster convergence rates for stiff systems;

APPENDIX A. TEMPORAL DISCRETISATION

- Time step is independent of the grid, which is beneficial for distorted meshes with highly varying control volume sizes; however,
- It is subjected to a large computational overhead per time step;
- Extension to parallel computing is more complex; and
- Maximum order of accuracy of unconditional stable linear multistep schemes is two.

Implicit schemes constitute a large system of equations that need to be evaluated at each time step. As described in the following section, these can either be solved directly or by means of iterative solvers.

A.3 Large systems of equations

As noted in the previous section, the implicit temporal discretisation of the system of equations result in a large sparse system of coupled equations that can be written as

$$\mathbf{K} \cdot \mathbf{W} = \mathbf{f} \quad (\text{A.12})$$

where this system can either be solved by directly inverting the matrix \mathbf{K} or by solving it iteratively.

Direct solvers

The inversion of the left-hand side or the implicit operator is most commonly done through Gaussian elimination or some direct sparse matrix method (Blazek, 2001). Although these methods are capable of quadratic convergence, they are normally not implemented for large systems, such as three-dimensional flow problems, as the computational cost and memory usage associated with them are exceedingly high. The computational cost is of order $N_{eq}N_{ba}^2$ and the memory storage of order $N_{eq}N_{ba}$ (Blazek, 2001), where N_{eq} is the number of equations and N_{ba} is the bandwidth of the matrix. Direct solvers do not, therefore, provide a practical method of solving large systems of equations and is not considered in this study.

Iterative solvers

Various iterative methods have been presented in literature (Wesseling, 2001; Blazek, 2001; Löhner, 2001) which aim to increase computational efficiency and reduce memory requirements. An in depth discussion of this subject is considered beyond the scope of this study. As explained in Section 3.3, the Generalised Minimum Residual (GMRES) method with Lower-Upper Symmetric Gauss-Seidel (LU-SGS) preconditioning is used and is, therefore, discussed next. For a detail discussion

APPENDIX A. TEMPORAL DISCRETISATION

on the various other iterative methods the reader is referred to the literature cited above.

With iterative solvers, the matrix \mathbf{K} of Eq. (A.12) is not directly inverted, but the original system is replaced by a sequence of solutions of the form (Löhner, 2001)

$$\tilde{\mathbf{K}} \cdot (\mathbf{W}^{n+1} - \mathbf{W}^n) = \tilde{\mathbf{K}} \cdot \Delta \mathbf{W} = \Delta t_\tau \mathbf{Res} = \Delta t_\tau (\mathbf{f} - \mathbf{K} \cdot \mathbf{W}) \quad (\text{A.13})$$

where \mathbf{Res} is the residual vector and $\tilde{\mathbf{K}}$ is a preconditioning matrix. For $\tilde{\mathbf{K}} = \mathbf{K}$ the direct solution is recovered.

With iterative solvers, the aim is to find an effective preconditioning matrix $\tilde{\mathbf{K}}$ to approximate \mathbf{K} . The properties of an effective preconditioning matrix is that it should be

- Inexpensive to invert or decompose; and
- A representative approximation of \mathbf{K} , containing the relevant eigenvalues and eigenvectors information.

Löhner (2001) notes that these requirements are contradictory and that they tend to result in the loss of the low-eigenvalue information as \mathbf{K} is approximated with a preconditioner. He notes that most iterative solvers implement so-called globalisation procedures to prevent this loss of low-eigenvalue information. In this study, a LU-SGS preconditioner is used along with GMRES to accelerate the solution convergence.

LU-SGS

With LU-SGS preconditioning, we start by considering the left-hand side matrix \mathbf{K} and note that it can be stored in strict lower, upper, and diagonal matrices

$$\mathbf{K} = \mathbf{L} + \mathbf{U} + \mathbf{D} \quad (\text{A.14})$$

The LU-SGS factorised system reads

$$(\mathbf{D} + \mathbf{L})\mathbf{D}^{-1}(\mathbf{D} + \mathbf{U})\Delta \mathbf{W} = \mathbf{Res} + (\mathbf{L}\mathbf{D}^{-1}\mathbf{U})\Delta \mathbf{W} \quad (\text{A.15})$$

which can be approximated by neglecting the last term (Luo *et al.*, 2003, 1998).

The resulting equation is then solved in two steps of simple block matrix inversion. First, a lower or forward sweep is done

$$(\mathbf{D} + \mathbf{L})\Delta \mathbf{W}^* = \mathbf{Res} \quad (\text{A.16})$$

where after an upper or backward sweep is performed

$$(\mathbf{D} + \mathbf{U})\Delta \mathbf{W} = \mathbf{D}\Delta \mathbf{W}^* \quad (\text{A.17})$$

Although the LU-SGS method is more efficient than explicit schemes, it still requires a significant number of iterations before it reaches steady-state convergence. Its performance can further be improved by means of an iterative method. As noted previously, the GMRES method is employed for this purpose in this study.

APPENDIX A. TEMPORAL DISCRETISATION

GMRES

Similar to the conjugate gradient (CG) method, the GMRES method of Saad and Schultz (1986) is very efficient in solving large, sparse systems. The CG method, however, fails to produce acceptable results for non-symmetric matrices, such as those commonly found when discretising the flow equations. In order to counter this and properly account for complex eigenvalues, the space in which $\Delta\mathbf{W}$ is sought is widened through the so-called Krylov vector subspace. The Krylov space vectors are denoted \mathbf{v}^k , $k = 1, m$, where m is the dimension of the Krylov subspace or the number of search directions.

We start by constructing a set of search vectors, \mathbf{v}^k , $k = 1, m$, where a procedure similar to the one described by Löhner (2001) is followed:

- Construct the starting vector

$$\mathbf{v}^1 = \frac{\mathbf{Res}^n}{|\mathbf{Res}^n|}, \quad \mathbf{Res}^n = \mathbf{f} - \mathbf{K} \cdot \mathbf{W}^n \quad (\text{A.18})$$

- For $j = 1, 2, \dots, m - 1$ calculate

$$\mathbf{w}^{j+1} = \mathbf{K} \cdot \mathbf{v}^j - \sum_{i=1}^j h^{ij} \mathbf{v}^i, \quad h^{ij} = \mathbf{v}^i \cdot \mathbf{K} \cdot \mathbf{v}^j \quad (\text{A.19})$$

$$\mathbf{v}^{j+1} = \frac{\mathbf{w}^{j+1}}{|\mathbf{w}^{j+1}|} \quad (\text{A.20})$$

At each iteration, the increment in each solution is calculated from the expression

$$\Delta\mathbf{W} = \mathbf{v}^k a_k \quad (\text{A.21})$$

where a_k is calculated such that it minimises the residual (Löhner, 2001)

$$|\mathbf{K} \cdot (\mathbf{v}^k a_k) - \mathbf{Res}^n|^2 \rightarrow \min \quad (\text{A.22})$$

Löhner (2001) gives the following solution of the minimisation problem

$$(\mathbf{K} \cdot \mathbf{v}^k) \cdot (\mathbf{K} \cdot \mathbf{v}^l) a_l = (\mathbf{K} \cdot \mathbf{v}^k) \cdot \mathbf{Res}^n \quad (\text{A.23})$$

He then notes that for each GMRES iteration with m search directions the computational cost is of order m^2 scalar products and order m matrix vector multiplications. As with other conjugate gradient methods, the information transfer between unknowns only takes place on the RHS, making it necessary to use it in conjunction with the LU-SGS preconditioning to transfer information beyond the nearest neighbour.

Appendix B

Spatial interpolation of the discretised advective face flux

Most of the systems considered are advection dominated and the stabilising elliptic diffusive term tends to become negligible in most parts of the domain. The interpolation of the discretised face flux of the advection term becomes vital in establishing an accurate, stable solution. In this section different schemes for the interpolation of the advective term are considered, evaluating the accuracy of the schemes and the tendency of the scheme to cause spurious oscillations which may render the solution unstable. Versteeg and Malalasekera (1995) consider the following properties when evaluating various schemes:

- *Conservation*

With the finite volume approach, the partial derivatives of the governing equations are integrated and cast into weak form. Using the divergence theorem, the spatial derivatives can be written as a function of the fluxes crossing the control volume faces. These fluxes must be interpolated in a consistent manner to ensure the flux leaving the one control volume is equal to the flux entering the neighbouring volume. If a scheme is inconsistent in calculating the flux crossing a shared face, it may lead to a difference in the value used for the respective volumes and result in the scheme being non-conservative.

- *Boundedness*

In the absence of source terms, internal values must be bounded by prescribed boundary values. If a scheme does not comply with the boundedness requirements, the solution may become unstable or if the solution does converge it may possibly contain non-physical oscillations.

- *Transportiveness*

Transportiveness refers to the degree in which the interpolation takes the directionality of the flow into account when calculating the face value. The two

APPENDIX B. SPATIAL INTERPOLATION OF THE DISCRETISED ADVECTIVE FACE FLUX

extremes are central differencing which merely takes the average value as the face flux and does not consider the direction of flow, where on the other hand upwinding is completely direction biased and approximate the face value to be the same as the upwind value.

- *Accuracy*

The accuracy of a scheme can be established by determining the truncation error when compared to the expanded Taylor series.

If a one-dimensional system around the node ξ (see Figure B.1) is considered, then the general advection-diffusion equation can be written as

$$\frac{\partial \phi}{\partial t} + \frac{\partial u\phi}{\partial x} = \frac{\partial}{\partial x} \left(k \frac{\partial \phi}{\partial x} \right) \quad (\text{B.1})$$

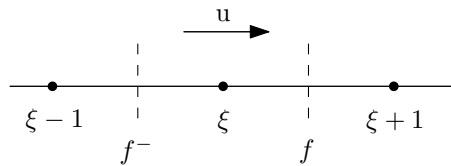


Figure B.1: Schematic representation of node points and edge faces on a one-dimensional grid

By following a similar approach as described in the finite volume edge-based discretisation discussed previously, cast Eq. (B.2) into weak form by integrating over the control volume, \mathcal{V}_ξ , and use Gauss' divergence theorem to write the advective term as the sum of the fluxes over the faces of the control volume

$$\frac{\Delta \phi_\xi}{\Delta t} \mathcal{V}_\xi + \int_{\mathcal{A}_\xi} u\phi \cdot n dA = \int_{\mathcal{V}_\xi} \frac{\partial}{\partial x} \left(k \frac{\partial \phi}{\partial x} \right) dV \quad (\text{B.2})$$

where

$$\int_{\mathcal{A}_\xi} u\phi \cdot n dA = \sum u_f \phi_f C_f \quad (\text{B.3})$$

B.1 Linear interpolation schemes

Central differencing

The most commonly used linear interpolation of the face flux is central differencing (CD). With CD the face value is taken as the average of the two neighbouring nodes

$$\phi_f = \frac{1}{2}(\phi_\xi + \phi_{\xi+1}) \quad (\text{B.4})$$

APPENDIX B. SPATIAL INTERPOLATION OF THE DISCRETISED ADVECTIVE FACE FLUX

As the face fluxes are calculated in a consistent manner for the different control volumes, CD ensures conservation. It is shown by Versteeg and Malalasekera (1995) that CD may lead to spurious oscillations and the solution becoming unbounded, where this is found to be particularly the case if sharp changes in the gradient are present. Blazek (2001) notes that CD can not suppress odd-even decoupling or spurious oscillations, and that artificial dissipation must be added for stability. Furthermore, as noted previously, the scheme does not take into consideration the direction of flow and can therefore not distinguish between upwind and downwind influences. However, for meshes with reasonable expansion ratios, it can be shown that CD is second order accurate.

Upwind differencing

The other commonly used scheme is upwind differencing (UD). With upwind differencing, the face value is taken to be equal to the value of the upwind node

$$\phi_f = \begin{cases} \phi_\xi & u > 0 \\ \phi_{\xi+1} & u < 0 \end{cases} \quad (\text{B.5})$$

Similar to CD, the face values are calculated in a consistent manner and the scheme is, therefore, conservative. When UD is used, the solution will remain bounded and is inherently stable as it will not cause non-physical oscillations. UD is, however, subjected to numerical diffusion, deteriorating the solution as the grid is coarsened or when flow is not aligned with the grid lines. Although UD takes the direction of flow into account when calculating the face values, it can be shown to be only first order accurate.

Higher order κ scheme

Various other linear interpolation schemes exist, and instead of considering each of them, the generalised higher order κ scheme is presented. This scheme also forms the base of the higher order non-linear schemes to be evaluated later on. The upwind biased κ scheme enhances the numerical accuracy by increasing the stencil size to three nodal values (Wesseling, 2001). The κ scheme can be expressed as follows (Waterson and Deconinck, 2007; Blazek, 2001)

$$\phi_f = \frac{1}{2}(\phi_\xi + \phi_{\xi+1}) + \frac{1-\kappa}{4}(-\phi_{\xi+1} + 2\phi_\xi - \phi_{\xi-1}^*) \quad u > 0 \quad (\text{B.6})$$

where Waterson and Deconinck (2007) note that the scheme can be viewed as CD with the addition of a stabilising, second order, upwind bias artificial dissipation term. From Eq. (B.6) it is noted that the upwind value, $\phi_{\xi-1}^*$, is included to improve the accuracy of the scheme. In the case of an unstructured mesh, a projected upwind approximation can be used (see Section B.3).

For different κ values Eq. (B.6) reduces to various well known higher order schemes. The second order upwind (SOU) scheme is found if $\kappa = -1$. When $\kappa = 0$

APPENDIX B. SPATIAL INTERPOLATION OF THE DISCRETISED ADVECTIVE FACE FLUX

Fromm's zero average phase error scheme is obtained (Fromm, 1968). The third order or cubic upwind biased scheme of Anderson *et al.* (1986) is obtained if $\kappa = \frac{1}{3}$. For $\kappa = \frac{1}{2}$ the QUICK (quadratic upstream interpolation for convective kinematics) proposed by Leonard (1979) is found. Finally, Eq. (B.6) reduces to the central differencing scheme if $\kappa = 1$. For all values of κ the scheme is second order accurate, except if $\kappa = \frac{1}{3}$, then the scheme becomes third order accurate. Waterson and Deconinck (2007) note that for $\kappa = 1$ the scheme eliminates the artificial diffusivity, but increases as κ reduces to -1 .

In a comparative analysis of linear schemes Waterson and Deconinck (2007) compared the accuracy and rate of convergence of the different κ schemes. They found that for smooth one-dimensional advection cases the accuracy of the third order upwind ($\kappa = 1/3$), Fromm's ($\kappa = 0$) and QUICK ($\kappa = 1/2$) scheme gave similar results, while the central difference ($\kappa = 1$) and second order upwinding ($\kappa = -1$) were notable less accurate. It is further stated that Fromm's scheme converged in 25 % less CPU time than both third order upwinding or QUICK, while central difference and second order upwinding schemes' rate of convergence were slower.

B.2 Non-linear interpolation schemes

As more complex physics need be modelled, the numerical approximation of ill-posed, non-linear systems are more commonly seen. Although the higher-order upwind biased schemes, discussed previously, prove to be more stable than pure central differencing, it is found that linear schemes are subjected to non-physical oscillations under circumstances where a sharp change in the gradient exist. According to Godunov's theorem, no higher order linear schemes can be monotonicity preserving (Roe, 1986).

It is, however, necessary to improve on the accuracy of the spatial interpolation of the convective face flux by using higher order schemes that are not subjected to the formation of spurious oscillations in the solution. This may be achieved by employing monotonic higher order non-linear schemes that provide the required accuracy while restricting the formation of spurious oscillations. There are two notable groups of non-linear schemes, the one group includes flux or slope limiting schemes and the second includes normalised variable schemes. The boundedness criteria typically employed are Total Variation Diminishing (TVD), positivity and Convection-Boundedness Criteria (CBC). The TVD approach is typically used in association with flux or slope schemes and CBC with normalised variable schemes.

Normalised variable schemes

A schematic representation of a one-dimensional system with normalised variable notation is shown in Figure B.2. The centre volume is referred to as the donor cell, the downwind cell as the acceptor and the other is the upwind cell. If it is assumed

APPENDIX B. SPATIAL INTERPOLATION OF THE DISCRETISED ADVECTIVE FACE FLUX

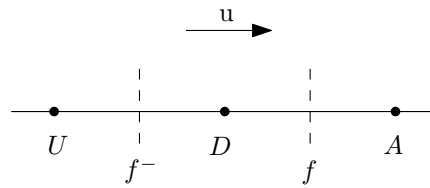


Figure B.2: Schematic representation of a one-dimensional grid for the donor-acceptor formulation

that the flow direction is positive, then the face under consideration, f , is located between the donor cell, D , and the acceptor cell, A .

In terms of the donor-acceptor model, the normalised variable as defined by Leonard (1991) is

$$\tilde{\phi} = \frac{\phi - \phi_U}{\phi_A - \phi_U} \quad (\text{B.7})$$

In general a non-linear scheme used to compute the face flux can be described as

$$\tilde{\phi}_f = \begin{cases} f(\tilde{\phi}_D) & u > 0 \\ f(\tilde{\phi}_A) & u < 0 \end{cases} \quad (\text{B.8})$$

where the function f must be defined in such a manner that it provides higher order accuracy while ensuring the monotonicity of the scheme is preserved. From Figure B.3 it is noted that to preserve the monotonicity of the scheme and preventing the generation of new local maximum and minimum values, $0 \leq \tilde{\phi}_D \leq 1$ must hold.

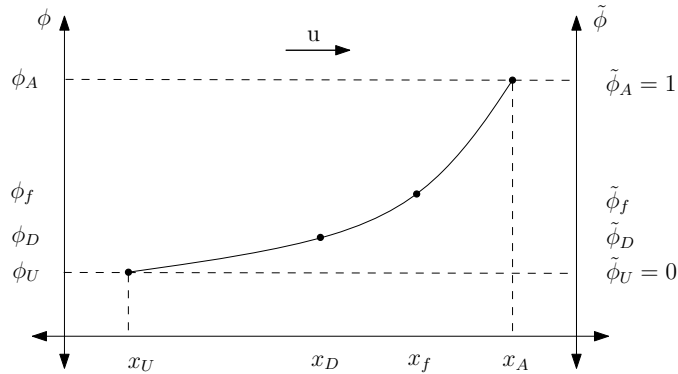


Figure B.3: Boundedness of the normalised variable to ensure monotonicity

To preserve local boundedness Gaskell *et al.* (1988) suggested the use of a convection boundedness criteria for one-dimensional implicit flow. Where the CBC are

APPENDIX B. SPATIAL INTERPOLATION OF THE DISCRETISED ADVECTIVE FACE FLUX

used to define bounds of the normalised face value to ensure local boundedness, for which the bounds on ϕ_f , for $u_f > 0$, are

$$\begin{aligned} \tilde{\phi}_f &= \tilde{\phi}_D & \text{for } \tilde{\phi}_D < 0 \text{ or } \tilde{\phi}_D > 1 \\ \tilde{\phi}_D &\leq \tilde{\phi}_f \leq 1 & \text{for } 0 \leq \tilde{\phi}_D \leq 1 \end{aligned} \quad (\text{B.9})$$

The κ scheme given above can be expressed in terms of the normalised variables (Wesseling, 2001)

$$\tilde{\phi}_f = \frac{2 - \kappa}{2} \tilde{\phi}_D + \frac{1 + \kappa}{4} \quad (\text{B.10})$$

where the use of the κ scheme in conjunction of the CBC provides a higher order scheme which preserves monotonicity. In Figure B.4 various schemes are shown on the normalised variable diagram (NVD), where the shaded area is as defined by Equation (B.9).

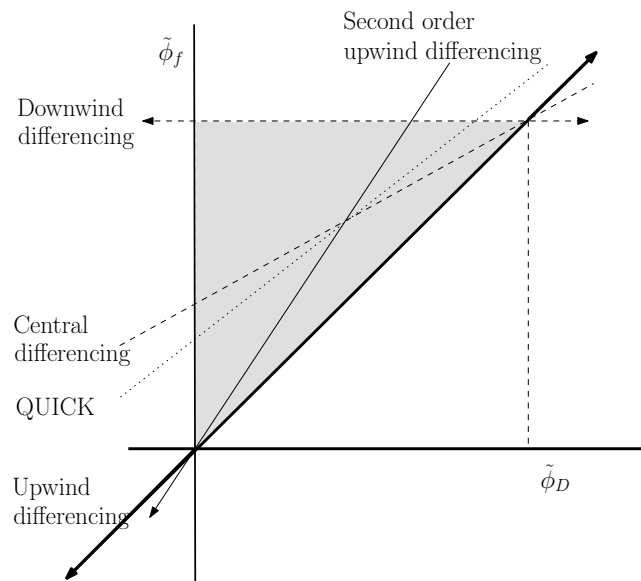


Figure B.4: Normalised variable diagram with the implicit convection boundedness criteria and various higher order schemes

The actual face value can then be recovered by employing the following relation

$$\phi_f = \tilde{\phi}_f \phi_A + (1 - \tilde{\phi}_f) \phi_U \quad (\text{B.11})$$

where

$$\phi_U = \frac{\phi_D - \tilde{\phi}_D \phi_A}{1 - \tilde{\phi}_D} \quad (\text{B.12})$$

APPENDIX B. SPATIAL INTERPOLATION OF THE DISCRETISED ADVECTIVE FACE FLUX

Substituting Eq. B.12 into Eq. B.11 to find the following expression for the face value

$$\phi_f = (1 - \beta_f)\phi_D + \beta_f\phi_A \quad (\text{B.13})$$

where weighting factor β_f is calculated as follows

$$\beta_f = \frac{\tilde{\phi}_f - \tilde{\phi}_D}{1 - \tilde{\phi}_D} \quad (\text{B.14})$$

Limiter functions

Limiter functions normally refer to flux limiting or slope limiting schemes. In their study Anderson *et al.* (1986) showed that better accuracy is achieved with slope limiting than with flux limiting and, therefore, only slope limiting schemes will be considered in this study. For detail description of flux limiting schemes refer to Wesseling (2001) and Blazek (2001).

The slope limiter functions regulate the slopes used to determine the face fluxes. At sharp discontinuities the slope is limited to prevent the creation of new extrema, this is done by recovering the first order upwind scheme in the immediate vicinity of high gradients. To reduce the amount of numerical dissipation, the limiter needs, however, to recover the original higher order interpolation in smooth regions.

Van Leer (1976) approximated ϕ with a piecewise linear distribution, but limited the slopes of the piecewise linear distribution to prevent the creation of non-physical oscillations in the solution. The left and right state of a face, which indicate if the discretisation is biased towards the node values on the left or right side of the face (Figure B.5) can be expressed as follows (Waterson and Deconinck, 2007; Blazek, 2001).

$$\begin{aligned} \phi_f^L &= \phi_\xi + \frac{1}{2}\psi(r_f^L)(\phi_\xi - \phi_{\xi-1}) \\ \phi_f^R &= \phi_{\xi+1} - \frac{1}{2}\psi(r_f^R)(\phi_{\xi+2} - \phi_{\xi+1}) \end{aligned} \quad (\text{B.15})$$

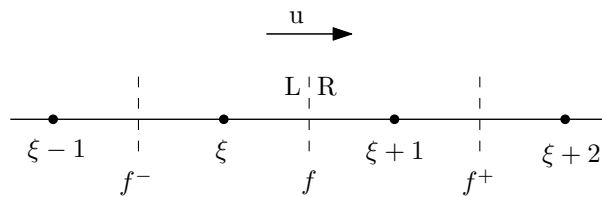


Figure B.5: One-dimensional stencil showing the left and right states of face, f

APPENDIX B. SPATIAL INTERPOLATION OF THE DISCRETISED ADVECTIVE FACE FLUX

The slope limiter, ψ , is a function of the gradients, r^L and r^R , which can be determined as follows

$$\begin{aligned} r_f^L &= \frac{\phi_{\xi+1} - \phi_{\xi}}{\phi_{\xi} - \phi_{\xi-1}^*} \\ r_f^R &= \frac{\phi_{\xi+1} - \phi_{\xi}}{\phi_{\xi+2}^* - \phi_{\xi+1}} \end{aligned}$$

The κ -scheme can then easily be recovered by setting the slope function in Eq. (B.15) equal to

$$\begin{aligned} \psi(r_f^L) &= \frac{(1+\kappa)}{2} r_f^L + \frac{(1-\kappa)}{2} \\ \psi(r_f^R) &= \frac{(1+\kappa)}{2} r_f^R + \frac{(1-\kappa)}{2} \end{aligned} \quad (\text{B.16})$$

which will give

$$\begin{aligned} \phi_f^L &= \phi_{\xi} + \frac{1}{4} [(1+\kappa)(\phi_{\xi+1} - \phi_{\xi}) + (1-\kappa)(\phi_{\xi} - \phi_{\xi-1}^*)] \\ \phi_f^R &= \phi_{\xi+1} - \frac{1}{4} [(1+\kappa)(\phi_{\xi+1} - \phi_{\xi}) + (1-\kappa)(\phi_{\xi+2}^* - \phi_{\xi+1})] \end{aligned} \quad (\text{B.17})$$

For monotonic solution, the slope function is limited using either the total variation diminishing or positivity boundedness criteria. Waterson and Deconinck (2007) notes that TVD is a stronger criterion than positivity and will therefore be used in this study. TVD is monotonic and is inherently stable, as no new local extrema is created that can cause the solution to diverge. The limiter diagram of Sweby (1984) is shown in figure B.6. The shaded area indicates the admissible region for TVD schemes with second order accuracy.

Various higher order TVD limiter have been proposed in literature. The general Sweby limiter is

$$\psi(r) = \max[0, \min(\beta r, 1), \min(r, \beta)] \quad (\text{B.18})$$

where $1 \leq \beta \leq 2$. If $\beta = 2$ the limiter reduces to the highly compressive Superbee limiter. For $\beta = 1$ the limiter reduce to Minmod, which is fairly simple as it switches between CD and SOU, but is found not to be very effective (Waterson and Deconinck, 2007).

Van Leer's MUSCL scheme is a slope-limited form of the Fromm's scheme. In smooth regions the scheme follows as much as possible the Fromm's scheme and only deviates from it in regions with large gradients where it reverts back the Sweby limiter.

$$\psi = \max \left[0, \min \left(2r, \frac{1+\kappa}{2} r + \frac{1-\kappa}{2}, 2 \right) \right] \quad (\text{B.19})$$

The MUSCL scheme provides a good combination of good accuracy in smooth regions, with reasonable resolution of sharp gradients while maintaining good convergence characteristics (Waterson and Deconinck, 2007).

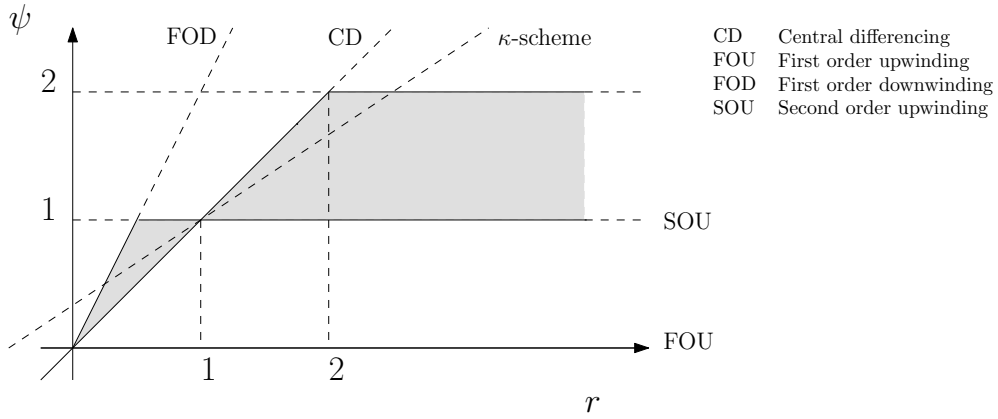
APPENDIX B. SPATIAL INTERPOLATION OF THE DISCRETISED ADVECTIVE FACE FLUX


Figure B.6: Admissible region for TVD second order schemes

Other limiters include the van Albada limiter

$$\psi(r) = \frac{r(r+1)}{r^2+1} \quad (\text{B.20})$$

and the Harmonic limiter

$$\psi(r) = \frac{r+|r|}{r+1} \quad (\text{B.21})$$

The reader is referred to Waterson and Deconinck (2007), Wesseling (2001) and Blazek (2001) for a detailed discussion on the different limiters and a comparison of them.

B.3 Extension to unstructured meshes

Consider the unstructured meshes shown in Figure B.7. It is noted that the upwind and downwind values, ϕ_{i-1}^* and ϕ_{i+2}^* , are unknown. Zhao *et al.* (2002) suggested the following approximation to accommodate the larger stencil of the flux or slope limiting scheme.

$$\begin{aligned} \Delta_i^+ &= \phi_{i+1} - \phi_i \\ \Delta_i^- &= \phi_i - \phi_{i-1}^* = 2\nabla\phi_i - (\phi_{i+1} - \phi_i) \\ &= 2\nabla\phi_i - \Delta_i^+ \\ \Delta_{i+1}^+ &= \phi_{i+2}^* - \phi_{i+1} = 2\nabla\phi_{i+1} - (\phi_{i+1} - \phi_i) \\ &= 2\nabla\phi_{i+1} - \Delta_i^+ \end{aligned} \quad (\text{B.22})$$

APPENDIX B. SPATIAL INTERPOLATION OF THE DISCRETISED ADVECTIVE FACE FLUX

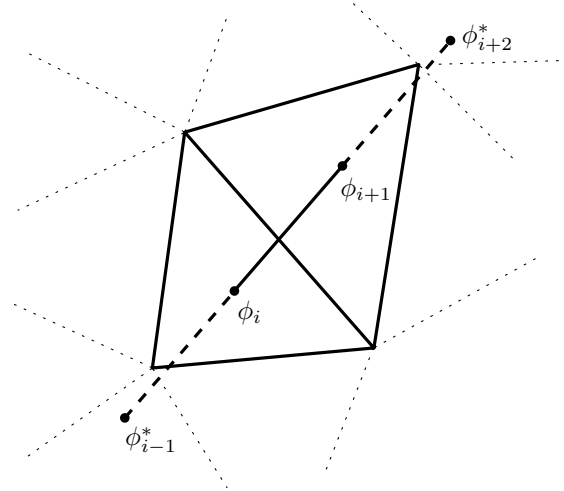


Figure B.7: Unstructured mesh

Substituting this approximation into Eq. (B.15) to find an unstructured formulation for the flux limiting scheme

$$\begin{aligned}\phi_{i+1/2}^L &= \phi_i + \frac{1}{2}\psi(r_{i+1/2}^L)(2\nabla\phi_i - \Delta_i^+) \\ \phi_{i+1/2}^R &= \phi_{i+1} - \frac{1}{2}\psi(r_{i+1/2}^R)(2\nabla\phi_{i+1} - \Delta_i^+)\end{aligned}\quad (\text{B.23})$$

In a similar manner the limiter slopes can be determined as follows for unstructured meshes

$$\begin{aligned}r_{i+1/2}^L &= \frac{\Delta_i^-}{\Delta_i^+} = \frac{2\nabla\phi_i - \Delta_i^+}{\Delta_i^+} \\ r_{i+1/2}^R &= \frac{\Delta_{i+1}^+}{\Delta_i^+} = \frac{2\nabla\phi_{i+1} - \Delta_i^+}{\Delta_i^+}\end{aligned}\quad (\text{B.24})$$

Ubbink and Issa (1999) adapted the normalised variable approach for arbitrary meshes where the upwind value is unknown. The predicted upwind value is then calculated using the following relation

$$\alpha_u^* = \min\{\max\{\alpha_A - 2(\nabla\alpha)_D \cdot \mathbf{d}, 0\}, 1\} \quad (\text{B.25})$$

Appendix C

Surface tension

As part of this study the continuum surface force (CSF) method of Brackbill *et al.* (1992), which is commonly used to model surface tension with the volume-of-fluid approach, is implemented. With this method a force, proportional to the curvature of the interface, is introduced to every control volume located within the interface. Brackbill *et al.* (1992) argue that the CSF method negates the need for costly interface reconstruction and is not restricted by topologically complex interfaces. Furthermore, this method is easily extended to unstructured three-dimensional meshes.

Williams *et al.* (1998) note that inaccuracies associated with the CSF method stems from the numerical approximation of the curvature. This follows for the inaccurate approximation of the spatial derivative of the volume fraction, as its gradient varies sharply over the interface. Ubbink (1997) shows that this inaccuracy results in the formation of low amplitude velocity field surrounding the interface, also referred to as parasitic currents by Lafaurie *et al.* (1994). By using a smoothed volume fraction, it is found that a more accurate approximation is obtained and the amplitude of the parasitic currents are reduced. Although various methods have been presented in literature (Cummins *et al.*, 2005; Williams *et al.*, 1998; Ubbink, 1997), the diffusive-type smoothing of the volume fraction using 2 explicit pseudo time loops (as presented in Chapter 4) is preferred.

The continuum surface tension source term which is added as a volume force to the average momentum equation reads

$$f_{\sigma}^j = \sigma \kappa \frac{\partial \alpha}{\partial x_j} \quad (\text{C.1})$$

where σ is the surface tension constant, which is positive for immiscible fluids.

To recover the correct force when the curvature radius approaches zero, a normalised curvature value is used. The curvature of the interface is described as the divergence of the unit vector normal to the interface

$$\kappa = -\frac{\partial n_i^*}{\partial x_i} \quad (\text{C.2})$$

APPENDIX C. SURFACE TENSION

where the unit normal vector is defined in Equation 4.26 and uses the smoothed volume fraction as calculated per Equation 4.29.

The surface tension body force is discretised by integrating over the control volume ξ so that

$$\begin{aligned} \int_{\xi} f_{\sigma}^j d\mathcal{V} &= \int_{\xi} \sigma \kappa \frac{\partial \alpha}{\partial x_j} d\mathcal{V} \\ &\approx \sigma \kappa_{\xi} \sum_{\Gamma \cap \mathcal{V}_{\xi}^j} \alpha_f C_f^j \end{aligned} \quad (\text{C.3})$$

where the curvature can be numerical approximated as

$$\begin{aligned} \kappa_{\xi} &= -\frac{1}{\mathcal{V}_{\xi}} \int_{\mathcal{V}_{\xi}} \frac{\partial n_i}{\partial x_i} d\mathcal{V} \\ &\approx -\frac{1}{\mathcal{V}_{\xi}} \sum_{\Gamma \cap \mathcal{V}_{\xi}} n_f^* C_f^i \end{aligned} \quad (\text{C.4})$$

To evaluate the numerical implementation of the CSF method, the pressure distribution over a static two-dimensional drop subjected to surface tension is considered. The drop is placed in a zero pressure field and the effect of gravity is neglected. White (2003) gives the following relation to calculate the average internal pressure for a infinite cylinder.

$$p_{avg} = \sigma \kappa = \sigma / R \quad (\text{C.5})$$

where R is the radius.

For this analysis a two-dimensional drop with a 1 mm radius is modelled and a 50×50 structured mesh is used to describe the $4 \text{ mm} \times 4 \text{ mm}$ computational domain. By averaging the pressure in the droplet and comparing it with the analytical solution it is found that the error is less than 2 %. A contour plot of the pressure is shown in Figure C.1a and the pressure distribution along the diagonal is shown in Figure C.1b.

APPENDIX C. SURFACE TENSION

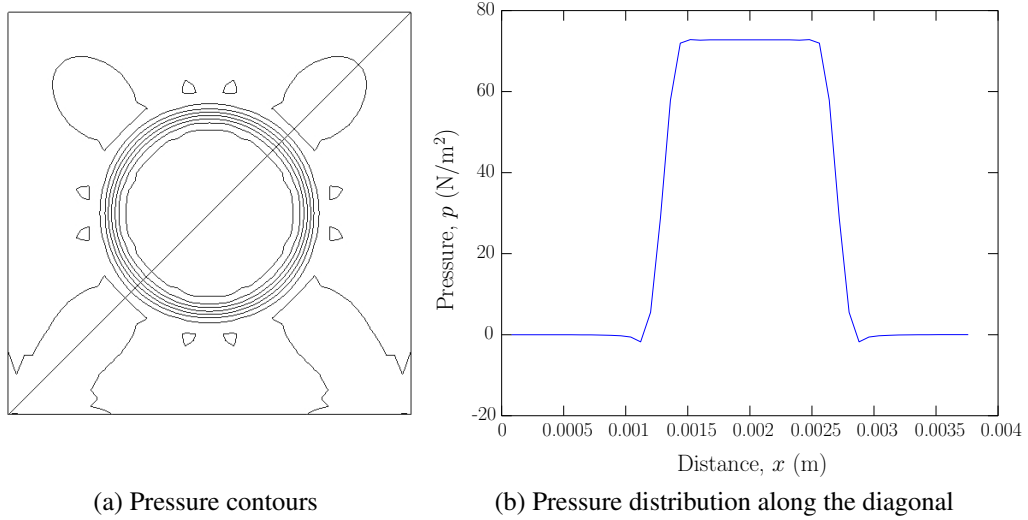
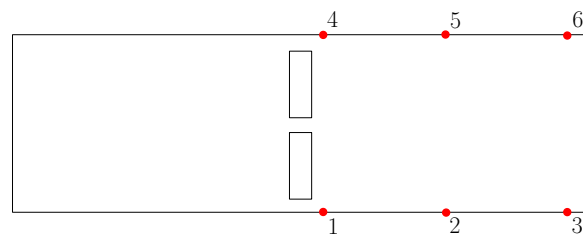


Figure C.1: Static two-dimensional drop subjected to surface tension

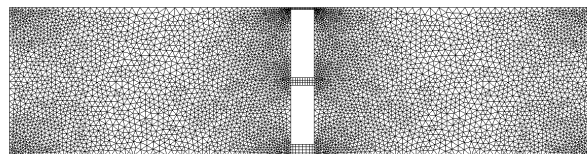
Appendix D

Validation of the weakly compressible liquid-gas flow solver

To validate the weakly compressible solver a partially filled tank with baffle configuration under lateral excitation is considered. It is numerically modelled using both a weakly compressible solver, accounting for variations in density, as well as an incompressible solver. The tank shown in Figure D.1a is 75 % filled with liquid and is subjected to sinusoidal lateral excitation where the maximum amplitude of displacement is 0.113 and the frequency is 1.5 Hz. This results in violent sloshing of the liquid within the tank with significant mixing of the liquid and gas. For this analysis an unstructured mesh with 6000 nodes, shown in Figure D.1b, is used and no-slip boundary conditions are assumed. As only relative pressures can be computed with the incompressible solver, the pressures relative to point 5 are given in the comparison of the weakly compressible and the incompressible solvers.



(a) Schematic representation



(b) Hybrid unstructured mesh

Figure D.1: Partially filled tank with baffle subjected to lateral excitation

APPENDIX D. VALIDATION OF THE WEAKLY COMPRESSIBLE LIQUID-GAS FLOW SOLVER

To evaluate the difference between the weakly compressible and incompressible solvers, the pressures at points 1 and 4 are compared with experimental results (BEELAB, 2008). In Figures D.2a and D.2b the pressures are shown just after a wave hits the top baffle opening at $t = 0.7$ s, when the effect of the compressibility is most pronounced as the pocket of gas is entrapped in the tank chamber. In the figures it is shown that the weakly compressible solver provides a noticeable improvement in capturing the oscillations seen in the experimental pressures due to the compression and expansion of the gas pocket.

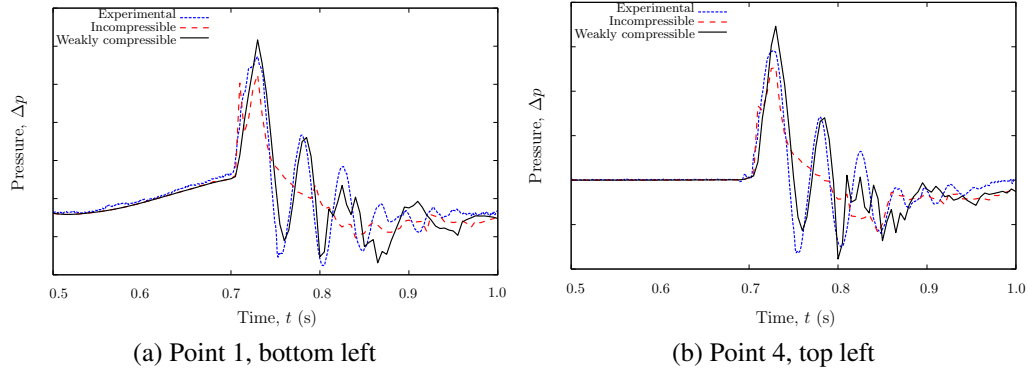


Figure D.2: Numerical and experimental predicted relative pressures

As the weakly compressible solver accounts for temporal variations in the gas density, it allows for the evaluation of the absolute pressures in the tank. In Figures D.3a and D.3b the predicted absolute pressures are compared with the experimental results. When considering the results, it is noted that the numerical results under predict the pressures to some degree. It was found that the weakly compressible solver is highly sensitive to the smearing of the interface, resulting in the discrepancy. Even though the volume-of-fluid approach is always subjected some amount of smearing, it is shown that the load frequency and amplitude are approximated with reasonable accuracy.

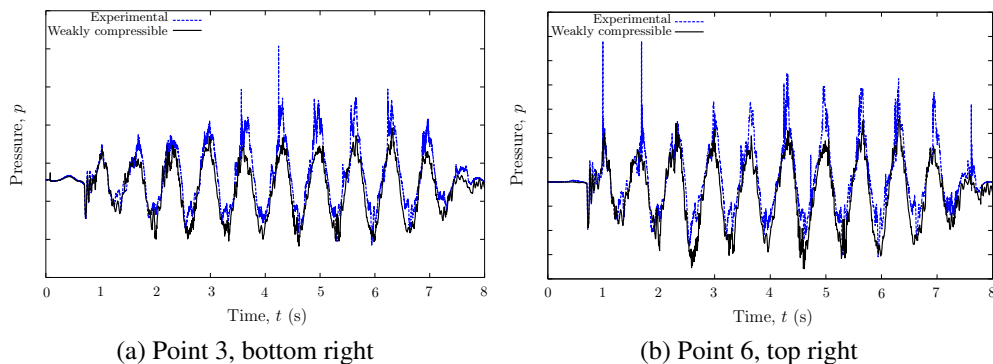


Figure D.3: Numerical and experimental predicted absolute pressures

APPENDIX D. VALIDATION OF THE WEAKLY COMPRESSIBLE LIQUID-GAS FLOW SOLVER

As noted in Chapter 6, it is found that the additional computational overhead for the weakly compressible formulation is negligible. Furthermore, the new weakly compressible formulation provides an improvement in the rate of convergence and for the problem considered here the computational time is reduced by approximately 30 %. Through the more accurate representation of the physics and accounting for variations in gas density, it is found that the numerical system is softened which results in the improved convergence rates.

References

- Abrahamsen, B. and Faltinsen, O. (2009). Decay of air cavity slamming pressure oscillations during sloshing at high fillings. In: *Proceedings of 24th International Workshop on Water Waves and Floating Bodies, April*, pp. 19–22.
- Anderson, W., Thomas, J. and Van Leer, B. (1986). Comparison of finite volume flux vector splittings for the Euler equations. *AIAA journal*, vol. 24, no. 9, pp. 1453–1460.
- Armenio, V. and Rocca, M.L. (1996). On the analysis of sloshing of water in rectangular containers: Numerical study and experimental validation. *Ocean Engineering*, vol. 23, no. 8, pp. 705 – 739.
- Babaei, R., Abdollahi, J., Homayonifar, P., Varahram, N. and Davami, P. (2006). Improved advection algorithm of computational modeling of free surface flow using structured grids. *Computer Methods in Applied Mechanics and Engineering*, vol. 195, no. 7-8, pp. 775 – 795.
- Bhajantri, M., Eldho, T. and Deolalikar, P. (2007). Numerical modelling of turbulent flow through spillway with gated operation. *International Journal for Numerical Methods in Engineering*, vol. 72, no. 2, pp. 221–243.
- Blazek, J. (2001). *Computational Fluid Dynamics: Principles and Applications*. 1st edn. Elsevier Science, Oxford.
- Bonometti, T. and Magnaudet, J. (2007). An interface-capturing method for incompressible two-phase flows. validation and application to bubble dynamics. *International Journal of Multiphase Flow*, vol. 33, no. 2, pp. 109 – 133.
- Brackbill, J., Kothe, D. and Zemach, C. (1992). A continuum method for modeling surface tension. *Journal of Computational Physics*, vol. 100, no. 2, pp. 335–354.
- Bullock, G., Obhrai, C., Peregrine, D. and Bredmose, H. (2007). Violent breaking wave impacts. Part 1: Results from large-scale regular wave tests on vertical and sloping walls. *Coastal Engineering*, vol. 54, no. 8, pp. 602–617.
- Cassidy, D.A., Edwards, J.R. and Tian, M. (2009). An investigation of interface-sharpening schemes for multi-phase mixture flows. *Journal of Computational Physics*, vol. 228, no. 16, pp. 5628 – 5649.

REFERENCES

- Chang, W., Lee, L., Lien, H. and Lai, J. (2008). Simulations of dam-break flows using free surface capturing method. *Journal of Mechanics*, vol. 24, no. 4, pp. 391–403.
- Chen, Y., Price, W. and Temarel, P. (2009). Numerical simulation of liquid sloshing in LNG tanks using a compressible two-fluid flow model. In: *Proceedings of the Nineteenth International Offshore and Polar Engineering Conference, Osaka, Japan*.
- Choi, Y.H. and Merkle, C.L. (1993). The application of preconditioning in viscous flows. *Journal of Computational Physics*, vol. 105, pp. 207–223.
- Chorin, A. (1968). Numerical solution of the Navier-Stokes equations. *Mathematics of Computation*, vol. 22, no. 104, pp. 745–762.
- Chorin, A.J. (1967). A numerical method for solving incompressible viscous flow problems. *Journal of Computational Physics*, vol. 2, pp. 12–26.
- Clarke, A. and Issa, R.I. (1997). A numerical model of slug flow in vertical tubes. *Computers and Fluids*, vol. 26, no. 4, pp. 395 – 415.
- Crumpton, P.I., Moinier, P. and Giles, M.B. (1997). An unstructured algorithm for high Reynolds number flows on highly stretched meshes. *Numerical Methods in Laminar and Turbulent Flow* (ed. C. Taylor and J. T. Cross), pp. 561–572.
- Cummins, S.J., Francois, M.M. and Kothe, D.B. (2005). Estimating curvature from volume fractions. *Computers and Structures*, vol. 83, no. 6-7, pp. 425 – 434.
- Darwish, M. and Moukalled, F. (2006). Convective schemes for capturing interfaces of free-surface flows on unstructured grids. *Numerical Heat Transfer, Part B: Fundamentals*, vol. 49, no. 1, pp. 19–42.
- De Foy, B. and Dawes, W. (2000). Unstructured pressure-correction solver based on a consistent discretization of the Poisson equation. *International Journal for Numerical Methods in Fluids*, vol. 34, pp. 463–478.
- De Sousa, F.S., Mangiavacchi, N., Nonato, L.G., Castelo, A., Tomé, M.F., Ferreira, V.G., Cuminato, J.A. and McKee, S. (2004). A front-tracking/front-capturing method for the simulation of 3D multi-fluid flows with free surfaces. *Journal of Computational Physics*, vol. 198, no. 2, pp. 469 – 499.
- Delorme, L., Iglesias, A. and Perez, S. (2005). Sloshing loads simulation in LNG tankers with SPH. In: *Proceedings of the International Conference on Computational Methods in Marine Engineering, Barcelona*.
- Dias, F., Dutykh, D. and Ghidaglia, J. (2010). A two-fluid model for violent aerated flows. *Computers & fluids*, vol. 39, no. 2, pp. 283–293.

REFERENCES

- Faltinsen, O., Rognebakke, O. and Timokha, A. (2005). Classification of three-dimensional nonlinear sloshing in a square-base tank with finite depth. *Journal of Fluids and Structures*, vol. 20, pp. 81–103.
- Farmer, J., Martinelli, L. and Jameson, A. (1994). Fast multigrid method for solving incompressible hydrodynamic problems with free surfaces. *AIAA journal*, vol. 32, no. 6, pp. 1175–1182.
- Ferziger, J.H. and Perić, M. (1999). *Computational Methods for Fluid Dynamics*. Springer-Verlag, New York.
- Fromm, J. (1968). A method for reducing dispersion in convective difference schemes. *Journal of Computational Physics*, vol. 3, no. 2, pp. 176–189.
- Gaskell, P., Lau, A. and Wright, N. (1988). Comparison of two solution strategies for use with higher-order discretization schemes in fluid flow simulation. *International Journal for Numerical Methods in Fluids*, vol. 8, no. 10, pp. 1203–1215.
- Godderidge, B., Turnock, S., Earl, C. and Tan, M. (2009a). The effect of fluid compressibility on the simulation of sloshing impacts. *Ocean Engineering*, vol. 36, no. 8, pp. 578–587.
- Godderidge, B., Turnock, S., Tan, M. and Earl, C. (2009b). An investigation of multiphase CFD modelling of a lateral sloshing tank. *Computers & Fluids*, vol. 38, no. 2, pp. 183–193.
- Gopala, V.R. and van Wachem, B.G. (2008). Volume of fluid methods for immiscible-fluid and free-surface flows. *Chemical Engineering Journal*, vol. 141, no. 1-3, pp. 204–221.
- Hirt, C. and Nichols, B. (1981). Volume of fluid (VOF) method for the dynamics of free boundaries. *Journal of Computational Physics*, vol. 39, no. 1, pp. 201–225.
- Hoekstra, M., Vaz, G., Abiel, B. and Bunnik, T. (2007). Free-surface flow modelling with interface capturing techniques. In: *Proceedings of the International Conference on Computational Methods in Marine Engineering, Barcelona, Spain*.
- Hogg, P., Gu, X. and Emerson, D. (2006). An implicit algorithm for capturing sharp fluid interfaces in the volume of fluid advection method. In: *Proceedings of European Conference on Computational Fluid Dynamics-ECCOMAS CFD, Egmond aan Zee, Netherlands*.
- Hwang, W. and Stoehr, R. (1988). Molten metal flow pattern prediction for complete solidification analysis of near net shape castings. *Materials Science and Technology*, vol. 4, no. 3, pp. 240–250.

REFERENCES

- Jasak, H. and Weller, H. (1995). Interface tracking capabilities of the inter-gamma differencing scheme. Tech. Rep., Technical report, CFD research group, Imperial College, London, 1995.
- Lafaurie, B., Nardone, C., Scardovelli, R., Zaleski, S. and Zanetti, G. (1994). Modelling merging and fragmentation in multiphase flows with SURFER. *Journal of Computational Physics*, vol. 113, no. 1, pp. 134–147.
- Lee, D., Kim, M., Kwon, S., Kim, J. and Lee, Y. (2007). A parametric sensitivity study on LNG tank sloshing loads by numerical simulations. *Ocean Engineering*, vol. 34, no. 1, pp. 3–9.
- Leonard, B. (1979). A stable and accurate convective modelling procedure based on quadratic upstream interpolation. *Computer Methods in Applied Mechanics and Engineering*, vol. 19, no. 1, pp. 59–98.
- Leonard, B.P. (1991). The ultimate conservative difference scheme applied to unsteady one-dimensional advection. *Computer Methods in Applied Mechanics and Engineering*, vol. 88, no. 1, pp. 17 – 74.
- Liou, M., Nguyen, L., Chang, C. and Theofanous, T. (2007). How to solve compressible multifluid equations: a simple, robust and accurate method. *AIAA paper*, vol. 4456, p. 2007.
- Liu, D. and Lin, P. (2009). Three-dimensional liquid sloshing in a tank with baffles. *Ocean Engineering*, vol. 36, pp. 202–212.
- Löhner, R. (2001). *Applied CFD Techniques*. John-Wiley and Sons Ltd., Chichester.
- Löhner, R., Yang, C. and Oñate, E. (2006). On the simulation of flows with violent free surface motion. *Computer Methods in Applied Mechanics Engineering*, vol. 195, pp. 5597–5620.
- López, J. and Hernández, J. (2010). On reducing interface curvature computation errors in the height function technique. *Journal of Computational Physics*, vol. 229, no. 13, pp. 4855 – 4868.
- Lugni, C., Brocchini, M. and Faltinsen, O. (2006). Wave impact loads: The role of the flip-through. *Physics of Fluids*, vol. 18.
- Luo, H., Baum, J.D. and Löhner, R. (1994). Edge-based finite-element scheme for the Euler equations. *AIAA*, vol. 32, no. 6, pp. 1183–1190.
- Luo, H., Baum, J.D. and Löhner, R. (1998). A fast, matrix-free implicit method for compressible flows on unstructured grids. *Journal of Computational Physics*, , no. 146, pp. 664–690.

REFERENCES

- Luo, H., Sharov, D., Baum, J. and Löhner, R. (2003). Parallel unstructured grid GMRES+LU-SGS method for turbulent flows. *AIAA Paper 2003*, vol. 273.
- Malan, A. and Lewis, R. (2011). An artificial compressibility CBS method for modelling heat transfer and fluid flow in heterogeneous porous materials. *International Journal for Numerical Methods in Engineering*, vol. 87, pp. 412–423.
- Malan, A. and Oxtoby, O. (2010). A parallel free-surface-modelling technology for application to aircraft fuel-sloshing. In: *Proceedings of ECCOMAS CFD-Fifth European Conference on Computational Fluid Dynamics, Lisbon, Portugal*, vol. 14.
- Malan, A.G. (2002). *Investigation into the Continuum Thermodynamic Modeling of Investment Casting Shell-Mould Drying*. Ph.D. thesis, University of Wales Swansea.
- Malan, A.G., Lewis, R.W. and Nithiarasu, P. (2002a). An improved unsteady, unstructured, artificial compressibility, finite volume scheme for viscous incompressible flows: Part I. Theory and implementation. *International Journal for Numerical Methods in Engineering*, vol. 54, no. 5, pp. 695–714.
- Malan, A.G., Lewis, R.W. and Nithiarasu, P. (2002b). An improved unsteady, unstructured, artificial compressibility, finite volume scheme for viscous incompressible flows: Part II. Application. *International Journal for Numerical Methods in Engineering*, vol. 54, no. 5, pp. 715–729.
- Malan, A.G., Meyer, J.P. and Lewis, R.W. (2007). Modelling non-linear heat conduction via a fast matrix-free implicit unstructured-hybrid algorithm. *Computer Methods in Applied Mechanics and Engineering*, vol. 196, no. 45-48, pp. 4495–4504.
- Murrone, A. and Guillard, H. (2005). A five equation reduced model for compressible two phase flow problems. *Journal of Computational Physics*, vol. 202, no. 2, pp. 664–698.
- Muzaferija, S., Peric, M., Sames, P. and Schellin, T. (1998). A two-fluid Navier-Stokes solver to simulate water entry. In: *Proc 22nd Symposium on Naval Hydrodynamics*, pp. 277–289.
- Nithiarasu, P. (2003). An efficient artificial compressibility (AC) scheme based on the characteristic based split (CBS) method for incompressible flow. *International Journal for Numerical Methods in Engineering*, vol. 56, no. 13, pp. 1815–1845.
- Oxtoby, O.F. and Malan, A.G. (2011). A matrix-free, implicit, incompressible fractional-step algorithm for fluid-structure interaction applications. *Submitted for publication*.

REFERENCES

- Panahi, R., Jahanbakhsh, E. and Seif, M. (2006). Development of a VoF-fractional step solver for floating body motion simulation. *Applied Ocean Research*, vol. 28, no. 3, pp. 171–181.
- Popinet, S. and Zaleski, S. (1999). A front-tracking algorithm for accurate representation of surface tension. *International Journal for Numerical Methods in Fluids*, vol. 30, no. 6, pp. 775–793.
- Raessi, M., Mostaghimi, J. and Bussmann, M. (2010). A volume-of-fluid interfacial flow solver with advected normals. *Computers & Fluids*, vol. 39, no. 8, pp. 1401 – 1410.
- Reddy, D.N. and Radosavljevic, D. (2006). Verification of numerical methods applied to sloshing studies in membrane tanks of LNG ships. In: *Proceedings of International Conference - ICSOT 2006: Design, Construction and Operation Of Natural Gas Carriers and Offshore Systems*, pp. 163–178.
- Roe, P. (1986). Characteristic-based schemes for the Euler equations. *Annual Review of Fluid Mechanics*, vol. 18, no. 1, pp. 337–365.
- Romenski, E. and Toro, E. (2004). Compressible two-phase flows: two-pressure models and numerical methods. *Comput. Fluid Dyn. J*, vol. 13, pp. 403–416.
- Rusche, H. (2002). *Computational fluid dynamics of dispersed two-phase flows at high phase fractions*. Ph.D. thesis, Imperial College, University of London.
- Saad, Y. and Schultz, M. (1986). GMRES: A generalized minimal residual algorithm for solving nonsymmetric linear systems. *SIAM Journal on Scientific and Statistical Computing*, vol. 7, no. 3, pp. 856–869.
- Scardovelli, R. and Zaleski, S. (1999). Direct numerical simulation of free-surface and interfacial flow. *Annual Review of Fluid Mechanics*, vol. 31, no. 1, pp. 567–603.
- Sethian, J. (2003). Level set methods and fast marching methods. *Journal of Computing and Information Technology*, vol. 11, no. 1, pp. 1–2.
- Shuen, J.S., Chen, K.H. and Choi, Y.H. (1993). A coupled implicit method for chemical non-equilibrium flows at all speeds. *Journal of Computational Physics*, vol. 106, pp. 306–318.
- Song, C. and Yuan, M. (1988). A weakly compressible flow model and rapid convergence methods. *Journal of Fluids Engineering*, vol. 110, no. 4, pp. 441–455.
- Song, C. and Zhou, F. (1999). Simulation of free surface flow over spillway. *Journal of Hydraulic Engineering*, vol. 125, no. 9, pp. 959–967.

REFERENCES

- Sussman, M., Almgren, A., Bell, J., Colella, P., Howell, L. and Welcome, M. (1999). An Adaptive Level Set Approach for Incompressible Two-Phase Flows. *Journal of Computational Physics*, vol. 148, no. 1, pp. 81–124.
- Sweby, P. (1984). High resolution schemes using flux limiters for hyperbolic conservation laws. *SIAM Journal on Numerical Analysis*, pp. 995–1011.
- Takatani, K. (2007). Mathematical modeling of incompressible mhd flows with free surface. *ISIJ international*, vol. 47, no. 4, pp. 545–551.
- Terashima, H. and Tryggvason, G. (2010). A front-tracking method with projected interface conditions for compressible multi-fluid flows. *Computers & Fluids*, vol. 39, no. 10, pp. 1804 – 1814.
- BEELAB (2008). Test reference BAE808: Laboratory simulation of sloshing in part-filled tanks.
- Tsui, Y.-Y., Lin, S.-W., Cheng, T.-T. and Wu, T.-C. (2009). Flux-blending schemes for interface capture in two-fluid flows. *International Journal of Heat and Mass Transfer*, vol. 52, no. 23-24, pp. 5547 – 5556.
- Turkel, E. (1987). Preconditioning methods for solving incompressible and low speed compressible equations. *Journal of Computational Physics*, vol. 72, pp. 227–298.
- Ubbink, O. (1997). *Numerical prediction of two fluid systems with sharp interfaces*. Ph.D. thesis, Department of Mechanical Engineering, Imperial College, London.
- Ubbink, O. and Issa, R.I. (1999). A method for capturing sharp fluid interfaces on arbitrary meshes. *Journal of Computational Physics*, vol. 153, pp. 26–50.
- Unverdi, S.O. and Tryggvason, G. (1992). A front-tracking method for viscous, incompressible, multi-fluid flows. *Journal of Computational Physics*, vol. 99, no. 1, pp. 180 – 180.
- Vahdati, M., Morgan, K., Peraire, J. and Hassan, O. (1989). A cell-vertex upwind unstructured grid solution procedure for high-speed compressible viscous flow. In: *Proceedings at the International Conference on Hypersonic Aerodynamics*, pp. 12.1–12.22. Royal Aeronautical Society, London.
- Van Leer, B. (1976). Muscl, a new approach to numerical gas dynamics. In: *Proceedings of Computing in Plasma Physics and Astrophysics*, vol. 1.
- Versteeg, H. and Malalasekera, W. (1995). *An introduction to computational fluid dynamics: the finite volume method*. Longman Scientific & Technical.

REFERENCES

- Wacławczyk, T. and Koronowicz, T. (2006). Modeling of the wave breaking with CICSAM and HRIC high-resolution schemes. In: Wesseling, S., Oñate, E. and Périaux, J. (eds.), *Proceedings of the European Conference on Computational Fluid Dynamics ECCOMAS CFD*.
- Wacławczyk, T. and Koronowicz, T. (2008). Comparison of CICSAM and HRIC high-resolution schemes for interface capturing. *Journal of Theoretical and Applied Mechanics*, vol. 46, no. 2, pp. 325–345.
- Waterson, N. and Deconinck, H. (2007). Design principles for bounded higher-order convection schemes—a unified approach. *Journal of Computational Physics*, vol. 224, no. 1, pp. 182–207.
- Wesseling, P. (2001). *Principles of computational fluid dynamics*, vol. 29. Springer Verlag.
- White, F.M. (2003). *Fluid Mechanics*. 5th edn. McGraw-Hill, Boston.
- White, F.M. (2006). *Viscous Fluid Flow*. 3rd edn. McGraw-Hill International Editions, Singapore.
- Williams, M., Kothe, D. and Puckett, E. (1998). Convergence and accuracy of kernel-based continuum surface tension models. Tech. Rep., Los Alamos National Lab., NM (US).
- Zalesak, S. (1979). Fully multidimensional flux-corrected transport algorithms for fluids. *Journal of Computational Physics*, vol. 31, no. 3, pp. 335–362.
- Zhao, Y., Tan, H.H. and Zhang, B. (2002). A high-resolution characteristics-based implicit dual time-stepping VOF method for free surface flow simulation on unstructured grids. *Journal of Computational Physics*, vol. 183, no. 1, pp. 233 – 273.
- Zhao, Y. and Zhang, B. (2000). A high-order characteristics upwind FV method for incompressible flow and heat transfer simulation on unstructured grids. *Computer methods in applied mechanics and engineering*, vol. 190, no. 5-7, pp. 733–756.
- Zienkiewicz, O.C. and Taylor, R.L. (2000). *The Finite Element Method: Volume 3 - Fluid Dynamics*. 5th edn. Butterworth-Heinemann, Oxford.